

Model Studies on Rare Earth Oxide Thin Films: Surface Chemistry and Catalytic Properties

Dissertation

zur Erlangung des Doktorgrades der Naturwissenschaften

- Dr. rer. nat. -

Vorgelegt dem Promotionsausschuss
des Fachbereichs 2 (Chemie/Biologie)

der Universität Bremen

VON

Jin-Hao Jhang

Bremen, 2015

Erstgutachter: Prof. Dr. Marcus Bäumer (Universität Bremen)

Zweitgutachter: Prof. Dr. Jens Falta (Universität Bremen)

Erklärung

Hiermit erkläre ich, dass ich die Doktorarbeit mit dem Titel:

Model Studies on Rare Earth Oxide Thin Films: Surface Chemistry and Catalytic Properties

Selbstständig verfasst und geschrieben habe und außer den angegebenen Quellen keine weiteren Hilfsmittel verwendet habe. Diese Arbeit wurde nicht vorher an anderer Stelle eingereicht.

Bremen, den

(Jin-Hao Jhang)

ACKNOWLEDGEMENT

In 2011 I left my country Taiwan and started a new life in Germany for this PhD project. After four years at this moment I am writing this dissertation to make an ending of my PhD work. Many people who I met from the work and life during the four years indeed helped me a lot and I do appreciate all your kindness and friendliness.

First of all, I would like to thank **Prof. Dr. Marcus Bäumer** for organizing and supporting this PhD project. It is my honor to work in your group and your extensive knowledge in different fields always inspired me to learn more beyond UHV and surface science.

I would like to thank **Priv. –Doz. Dr. Volkmar Zielasek** for all the discussions and suggestions regarding data analysis and scientific writing. Your solid knowledge in physics and surface science especially made important contributions to this project. I also enjoyed your good sense of humor during lunch time, although sometimes I could not follow these jokes due to my limited German ability.

I am very grateful to **Dr. Andreas Schaefer** who is my direct supervisor. Your solid knowledge in REOs studies and surface science also made significant contributions to my PhD work. I enjoyed the time when we worked together in our labs and in Max-lab, Lund. Thank you for guiding and helping me during the PhD time, and I also missed the days when we drank beers after work. It was a pleasure to work with you.

I would like to thank **Prof. Dr. Jason F. Weaver** in the University of Florida. It was really great to have this collaboration with you, and I did enjoy my time in Florida, USA in 2012 and 2014. Also thank you for scientific discussions especially on STM and TPD techniques.

There are many thanks to my colleagues. Scientific discussions in seminars and chats at coffee breaks with you were always enjoyable. Especially I would like to thank **Theodor Weiss**. There were many good conversations with you, and your ideas always impressed me. I would also like to thank **Simona Keil**. Although we only worked together for a couple of months, it was great to finish the TPD works and write the manuscript regarding the CO/water studies with you. Particularly thank you for helping me to correct my German language in the abstract of this dissertation. Thank **Dr. Lyudmila Moskaleva** for many nice discussions about computational chemistry which were very

illuminating. Thank **Martin Nowak** for many technical supports in the UHV labs. Thank **Ingo Bardenhagen, Junjie Shi, Anastasia Lackmann, Imke Schrader, and Miriam Schubert** for the comfortable workplace environment. It was my pleasure working with you. Thank **Dr. Arne Wittstock** and **Dr. Sebastian Kunz** for providing me suggestions regarding scientific careers. I would like to thank **Ute Melville, Cornelia Rybarsch-Steinke, Vera Suling, and Brigitte Neimeier** for many helps during my PhD studies.

There are many thanks to my friends and family for supporting and encouraging me. I would like to share one of my favorite quotes from Albert Einstein with you.

“Beim Menschen ist es wie beim Velo. Nur wenn er fährt, kann er bequem die Balance halten.”

– Albert Einstein

ZUSAMMENFASSUNG/ABSTRACT

Seltenerdoxide (REOs) haben ein erhebliches Potential für die Durchführung bestimmter katalytischer Reaktionen gezeigt. Doch nur Ceroxid (CeO_x) wurde systematisch hinsichtlich seiner Oberflächenchemie und seiner Faktoren für das katalytische Verhalten untersucht. Das grundlegende Verständnis in Bezug auf die Verbindungen zwischen der Oberflächenchemie und den katalytischen Eigenschaften von anderen REOs ist immer noch sehr begrenzt. Der Hauptteil dieser Dissertation berichtet von oberflächenwissenschaftlichen Studien an Samariumoxid (SmO_x), die im Ultrahochvakuum durchgeführt werden. Darüber hinaus stellt die Dissertation kurz aktuelle Untersuchungen zu Praseodym (PrO_x), PrO_x - CeO_x Mischoxiden und Terbiumoxid (TbO_x), die von meiner Arbeitsgruppe (AG Bäumer) und unseren Mitarbeitern durchgeführt wurden, vor.

Dünne Sm_2O_3 Schichten aufgewachsen auf einem Pt(111) Substrat wurden als SmO_x Modellsysteme eingesetzt. Die strukturellen und Film morphologischen Studien wurden durch Beugung niederenergetischer Elektronen (LEED) und Rastertunnelmikroskopie (STM) durchgeführt. Solche dünnen Filme wachsen als defekt-Fluorit-Struktur, d.h. Sm-Atome ordnen sich in einem hexagonalen Untergitter, während sich Oberflächenfehlstellen zufällig in dem dünnen Film verteilen. Es wurde ein Film Benetzungs-/ Entnetzungs-Verhalten als Antwort auf die SmO_x Reduktions-/Oxidationsbedingungen beobachtet. Um etwas über die chemischen/katalytischen Eigenschaften des SmO_x Modellsystem zu lernen, wurden Kohlenmonoxid (CO), Wasser (D_2O) und Methanol (MeOH) auf das System für Adsorptions-Reaktionsexperimente mittels Temperaturprogrammierter Desorptionsspektroskopie (TPD) dosiert. Ferner wurde die MeOH-TPD Studie mit Infrarotabsorptionreflexionsspektroskopie (IRRAS) kombiniert, um den gesamten MeOH Reaktionsmechanismus des Modellsystems zu verstehen.

Der Einfluss der SmO_x Reduktions-/Oxidationsbedingungen auf die chemischen Reaktionen von diesen Adsorbaten wurden ebenfalls untersucht. Die Existenz der Perimeterstellen zwischen den SmO_x Inseln und den unbedeckten Pt Bereichen fördert offensichtlich die Reaktivität und ändert die chemischen Eigenschaften des SmO_x Modellsystems. Ein Überlaufen der adsorbierten Spezies von der SmO_x Oberfläche zu den sichtbaren Pt Bereichen wurde beobachtet. Dies ist besonders wichtig bei der Erhöhung der SmO_x Reaktivität in die Richtung der MeOH Zersetzung.

Rare earth oxides (REOs) have shown considerable capacities for performing certain catalytic reactions. However, only ceria (CeO_x) has been systematically studied regarding the surface chemistry and the factors for catalytic behavior. The fundamental understanding with respect to the connections between the surface chemistry and catalytic properties of other REOs is still in a very limited scope. Major part of this PhD dissertation reports on surface science studies of samaria (SmO_x) conducted in ultra-high vacuum. In addition, the dissertation briefly introduces recent studies on praseodymia (PrO_x), PrO_x - CeO_x mixed oxides, and terbium (TbO_x) which were carried out by my working group (AG Bäumer) and our collaborators.

Sm_2O_3 thin films grown on a Pt(111) substrate were employed as SmO_x model systems. Structural and film morphologic studies were conducted by low-energy electron diffraction (LEED) and scanning tunneling microscopy (STM). Such thin films grow as a defective-fluorite structure, *i.e.*, Sm atoms arrange into a hexagonal sublattice whereas surface vacancies randomly distribute on the thin films. A film wetting/dewetting behavior responding to the SmO_x reduction/oxidation conditions was observed. To learn about the chemical/catalytic properties of the SmO_x model system, carbon monoxide (CO), water (D_2O), and methanol (MeOH) were dosed onto the system for adsorption-reaction experiments conducted by temperature programmed desorption spectroscopy (TPD). The MeOH-TPD study was further combined with infrared absorption-reflection spectroscopy (IRRAS) to gain the whole picture of the MeOH reaction mechanism on the model system.

The influence of the SmO_x reduction/oxidation conditions on the chemical responses of these adsorbates were also investigated. The existence of the perimeter sites between SmO_x islands and uncovered Pt areas obviously promotes the reactivity and alters chemical properties of the SmO_x model system. A spillover of adsorbed species from the SmO_x surface to exposed Pt areas was observed. It is particularly important in increasing the SmO_x reactivity towards the MeOH decomposition.

LIST OF PUBLICATIONS

The major theme of this dissertation is based on the following Paper I, II, and III.

The summaries of Paper IV and V will be briefly introduced in Chapter 1.

Paper I.

Growth and Partial Reduction of Sm₂O₃(111) Thin Films on Pt(111): Evidence for the Formation of SmO(100), **J.-H. Jhang**, A. Schaefer, W. Cartas, S. Epuri, M. Bäumer, J.F. Weaver, *The Journal of Physical Chemistry C* **2013**, *117*, 21396 – 21406.

Contribution: I was responsible for performing the all experiments, the data analysis, and writing the manuscript.

Paper II.

CO and D₂O Chemistry on Continuous and Discontinuous Samaria Thin Films on Pt(111), **J.-H. Jhang**, S. Keil, A. Schaefer, V. Zielasek, M. Bäumer, *Surface Science*, Submitted for Initial Review.

Contribution: I was responsible for performing the all experiments, the data analysis, and writing the manuscript.

Paper III.

Methanol Adsorption and Reaction on Samaria Thin Films on Pt(111), **J.-H. Jhang**, A. Schaefer, V. Zielasek, J.F. Weaver, M. Bäumer, *Materials* **2015**, *8*, 6228 – 6256.

Contribution: I was responsible for performing the all experiments, the data analysis, and writing the manuscript.

Paper IV.

Temperature-Dependent Reduction of Epitaxial Ce_{1-x}Pr_xO_{2-δ} (x = 0 – 1) Thin Films on Si(111): A Combined Temperature-Programmed Desorption, X-ray Diffraction, X-ray Photoelectron Spectroscopy, and Raman Study, M.H. Zoellner, G. Niu, **J.-H. Jhang**, A. Schaefer, P. Zaumseil, M. Bäumer, T. Schroeder, *The Journal of Physical Chemistry C* **2013**, *117*, 24851 – 24857.

Contribution: I was responsible for performing the temperature programmed desorption experiments.

Paper V.

Controlling the Physics and Chemistry of Binary and Ternary Praseodymium and Cerium Oxide Systems, G. Niu, M.H. Zoellner, T. Schroeder, A. Schaefer, **J.-H. Jhang**, V. Zielasek, M. Baumer, H. Wilkens, J. Wollschlager, R. Olbrich, C. Lammers, M. Reichling, *Physical Chemistry Chemical Physics* **2015**, *17*, 24513 – 24540.

Contribution: I was responsible for performing the temperature programmed desorption and synchrotron radiation XPS experiments.

Conference Contributions

- Ultrathin samaria films on Pt(111) studied by PES and LEED (Poster)
76th DPG annual conference, April 2012, Berlin
- Growth of ultrathin samaria films on Pt(111) studied by LEED and STM (Presentation)
77th DPG annual conference, March 2013, Regensburg
- Growth and partial reduction of Sm₂O₃(111) thin films on Pt(111): evidence for the formation of SmO(100) (Poster)
CECAM workshop, October 2013, Bremen
- Methanol adsorption and reaction on SmO_x/Pt(111) systems studied by temperature programmed desorption and infrared reflection-absorption spectroscopy (Poster)
COST Action CM1104, September 2014, Delmenhorst
- Model studies beyond ceria: higher rare earth oxides in heterogeneous catalysis (Presentation)
Doktorandenkolloquium (Universität Bremen), December 2014, Bremen
- Methanol adsorption and reaction on SmO_x/Pt(111) systems studied by TPD and IRRAS (Poster)
79th DPG annual conference, March 2015, Berlin

TABLE OF CONTENTS

ACKNOWLEDGEMENT	I
ZUSAMMENFASSUNG/ABSTRACT	III
LIST OF PUBLICATIONS	V
CHAPTER 1 STUDIES OF RARE EARTH OXIDES IN CHEMISTRY	3
1.1 Introduction of rare earth oxides.....	3
1.2 Catalytic properties of REOs	4
1.3 Approach by surface science: studies of REO model systems	5
1.3.1 Studies of ceria, praseodymia, and terbia	5
1.3.2 Studies of samaria	10
CHAPTER 2 STRUCTURAL STUDIES OF SAMARIA THIN FILMS	12
2.1 As-prepared Sm ₂ O ₃ thin films	13
2.2 Thermal reduction of Sm ₂ O ₃ thin films	15
2.3 Reoxidation of reduced SmO _x thin films	18
2.4 Adjustable lattice structures: from quasi – to perfect – 3 x 3	19
2.5 Summary of the structural studies	21

CHAPTER 3 SURFACE CHEMISTRY OF SAMARIA THIN FILMS	22
3.1 CO chemistry – CO adsorption and reaction	23
3.2 Water chemistry.....	24
3.2.1 Water (D ₂ O) adsorption and dissociation	24
3.2.2 CO assistance for D ₂ production	27
3.3 Methanol chemistry	29
3.3.1 Methanol (MeOH) adsorption and reaction	29
3.3.2 SmO _x structural changes induced by MeOH	37
3.4 Summary of the surface chemistry studies.....	39
CHAPTER 4 CONCLUSION AND OUTLOOK.....	41
REFERENCE	43
<i>Abbreviations.....</i>	49
<i>Curriculum Vitae.....</i>	50
<i>Papers.....</i>	52

CHAPTER 1

STUDIES OF RARE EARTH OXIDES IN CHEMISTRY

1.1 Introduction of rare earth oxides

Elements in the lanthanum series are named rare earth elements (REEs). Scandium (Sc) and yttrium (Y) are not in this series but they exhibit fairly similar chemical/physical properties with regard to REEs, therefore normally both Sc and Y are included into the family of REE. As a matter of fact, REEs are not really “rare” considering their abundance on earth compared to other truly rare elements. The abundance of each rare earth element is actually similar to the crustal concentration of industrial metals such as nickel, molybdenum, tin, and gallium [1]. Nevertheless, due to the similar chemical and physical attributes of REEs in nature, the respective existence of REEs is “rarely” observed. **Table 1** shows the relevant characteristics of REEs, *i.e.* electronic configuration, standard atomization enthalpies, ionization potentials and ionic radii. Note that the ionic radii continuously decrease while the atomic numbers of REEs increase. This behavior is called “lanthanide contraction” which is due to the insufficient shielding effect by $4f$ electrons towards the outer shell electrons ($5d$ and $6s$). In ordinary environment, REEs tend to form oxides, named rare earth oxides (REOs), due to relatively low ionization potentials and standard atomization enthalpies of REEs (**Table 1**) [2].

Because the trivalent ($3+$) state exists generally in entire REEs, sesquioxides (RE_2O_3) are the most common REOs to be found for all REOs. Three REEs namely cerium (Ce), praseodymium (Pr), and terbium (Tb), possess the tetravalent ($4+$) state because their fourth ionization potentials are relatively lower than that of other REEs, therefore they are able to form dioxides and mixed-valent ($3+/4+$) oxides, such as CeO_2 , Pr_6O_{11} , and Tb_4O_7 . These oxides are also named as higher oxides. Apart from sesquioxides and higher oxides, lower oxides are also known and exist corresponding to the divalent ($2+$) state of REEs. For instance, samarium (Sm) and europium (Eu) have shown the capability of forming SmO and EuO under extreme temperature and pressure conditions [3, 4]. Thanks to the existence of several oxidation states in REE, one can expect REOs as fairly reducible materials. Indeed,

some of REOs, especially higher oxides have shown this capability. Moreover, high oxygen mobility is also generally observed in higher REOs, *i.e.* ceria, praseodymia, and terbia. In contrast, the rest of REOs exhibit relatively low oxygen mobility [5].

Element	Electron Conf.	$\Delta H_{\text{atom}}^{\circ}$ (KJ.mol ⁻¹)	Σ IP (1-3) (KJ.mol ⁻¹)	4th. IP (KJ.mol ⁻¹)	$r_{\text{ion}}(\text{M}^{3+})$ (pm)*
La	5d ¹ 6s ²	431.0	3455	4819	117
Ce	4f ¹ 5d ¹ 6s ²	420.1	3523	3547	115
Pr	4f ³ 6s ²	356.9	3627	3761	113
Nd	4f ⁴ 6s ²	326.9	3697	3899	112
Pm	4f ⁶ 6s ²	----	3740	3966	111
Sm	4f ⁶ 6s ²	206.9	3869	3994	110
Eu	4f ⁷ 6s ²	177.4	4036	4110	109
Gd	4f ⁷ 5d ¹ 6s ²	397.5	3749	4245	108
Tb	4f ⁹ 6s ²	388.7	3791	3839	106
Dy	4f ¹⁰ 6s ²	290.4	3911	4001	105
Ho	4f ¹¹ 6s ²	300.6	3924	4101	104
Er	4f ¹² 6s ²	316.4	3934	4115	103
Tm	4f ¹³ 6s ²	232.4	4045	4119	102
Yb	4f ¹⁴ 6s ²	155.6	4194	4220	101
Lu	4f ¹⁴ 5d ¹ 6s ²	427.6	3887	4360	100

Table 1. Electron configuration, standard atomization enthalpies, ionization potentials and ionic radii of rare earth elements [2].

In fact, REOs have been employed widely in many applications, *e.g.* as doping in glasses [6-9], materials for surface polishing [10], luminescent materials [9, 11], ion-conductors [9, 12-14], and catalysts [9, 15-18]. Apart from these applications, REOs also show their potentials for other uses. For instance, perovskite type mixed REOs are developed as high temperature superconductors [19, 20], moreover, REOs are also considered as high- κ dielectric materials [21-23]. Because catalytic properties of REOs are the main interest in this PhD project, they will be main focal points in the following parts of this dissertation.

1.2 Catalytic properties of REOs

Lanthana (La₂O₃) and ceria (CeO₂) as commercial catalysts are used in chemical industry. In the global REO-catalyst market (in 2008), 66 percent of REO catalysts was contributed by La₂O₃, 32 percent was contributed by CeO₂, only 2 percent was contributed by two other REOs, namely Pr₆O₁₁

and Nd_2O_3 [24]. The La_2O_3 catalyst is mainly used for “fluid cracking” reactions [25] and CeO_2 is a well-known material used as an oxygen-storage reservoir in three-way catalytic (TWC) converters [26]. Furthermore, CeO_2 as a reducible oxide has shown its potential to be employed in the water-gas-shift reaction [27-29] and pollution reduction, *i.e.* CO and NO_x oxidation [30-32]. Apart from La_2O_3 and CeO_2 , other REOs are still not commercially used as catalysts, nevertheless, they also exhibit impressive catalytic properties for particular reactions. For instance, samaria (Sm_2O_3) and europia (Eu_2O_3) are considered as worthy catalysts with high selectivity for higher hydrocarbon production in the oxidative coupling of methane (OCM) reaction [33-36]. Moreover, Sm_2O_3 also shows catalytic activity for a dehydration reaction of propan-2-ol to propene with impressive selectivity [37].

Currently, the basic concept to explain the catalytic behavior of REOs is related to lattice-oxygen mobility in oxides [2]. Higher oxygen mobility is observed in higher oxides, thus they usually lead to complete oxidation reactions. In contrast, sesquioxides have relatively low oxygen mobility which may induce incomplete oxidation reactions, and therefore lead to an increase of selectivity in certain partial oxidation reactions. However, apart from oxygen mobility or the so-called redox property, other fundamental properties such as acidity, basicity, surface structure, defects or vacancies can also influence the catalytic behavior and efficiency of REOs. To learn how the chemical properties of REOs respond to these factors in a heterogeneous reaction in which the catalyst surface is mainly in charge of reacting with adsorbates, and to gain fundamental understanding of the interaction between reactants and the catalyst surface, it is important to perform a systematic study under a well-controlled experimental condition. Such a study can be implemented in an ultra-high vacuum system by preparing a well-characterized low-index crystalline surface of the catalyst as a model surface for studying the interaction with reactants. This way is the so-called “surface science approach” which is extensively used to build up knowledge relevant to explaining chemical properties of certain catalytic surfaces [38, 39].

1.3 Approach by surface science: studies of REO model systems

1.3.1 Studies of ceria, praseodymia, and terbia

Ceria as the most popular material in the series of rare earth oxides has been intensively studied not only under ambient conditions but also in UHV. Recently, D.R. Mullins published a review article regarding the studies of ceria in surface chemistry [40]. The author summarized that so far three low-index faces of CeO₂, *i.e.* (111), (110), and (100) have been used as model systems. Especially the CeO₂(111) surface has been intensively studied by using diagnostic tools of UHV surface analysis as well as computational methods. To learn about chemical reactivity and behavior of these ceria surfaces, simple inorganic and organic molecules, *e.g.* CO, H₂O, NO, alcohols, and formic acid, etc. have been chosen for adsorption-reaction experiments on these surfaces. He concluded that the chemical properties and reactivity of ceria are clearly related to three main concepts: (1) coordination conditions of the surface atoms, *i.e.* Ce and O, (2) redox properties of ceria, and (3) oxidation conditions of the ceria surface. Furthermore, the author also summarized recent studies on “inverse ceria model catalysts” which exhibit unique and impressive properties toward certain chemical reactions. An inverse ceria model catalyst is fabricated by depositing discontinuous ceria thin films (oxide islands) onto a bulk metallic substrate, such as Pt(111), Au(111), Cu(111), and Rh(111). Such an inverse model catalyst differs from the “conventional” model catalyst in which metal nanoparticles are deposited onto a well-defined oxide surface. Unfortunately, the design of such a conventional surface is not conducive to catalytic activities of the oxide. The oxide surface defects and vacancies usually function as active sites for catalysis, however in the conventional model catalyst they are usually blocked by metal nanoparticles. In contrast, these active sites on the oxide surface are exposed in the inverse case, therefore reactants may react with the metal sites, the perimeter sites between oxide islands and the metal surface, and additionally these active sites on the oxide surface [41]. Particularly the studies of these inverse ceria model catalysts have been focused on the water-gas-shift reaction which involves two reactions, *i.e.* CO oxidation and water dissociation. These two reactions were also intensively studied on the ceria-metal systems. In the WGS reaction, ceria as a reducible oxide has the capability of promoting water dissociation and CO oxidation. Unfortunately, highly stable intermediates formed in the mixture of CO and water usually block the active sites and stop the reaction, thus ceria alone is not an active WGS catalyst. The inverse ceria catalysts may solve the problem in so far as the metal surface provides a platform for CO adsorption and the perimeter sites between ceria and metal surfaces can destabilize the intermediates.

Apart from ceria, other rare earth oxides have been paid less attention to surface science studies, although they also exhibit valuable properties for catalyzing certain chemical reactions as mentioned above. Particularly praseodymia (PrO_x), terbia (TbO_x), and samaria (SmO_x) have attracted interests. PrO_x and TbO_x are also able to form higher oxides, thus one may expect that their lattice oxygen mobility, oxygen storage capacity, and the redox property are the primary key for driving catalytic reactions. SmO_x is, in contrast to PrO_x and TbO_x not forming higher oxides and has been considered as an important catalyst for the OMC reaction which may be related to its surface structure, acid-base property and the limited oxygen mobility. In order to gain greater understanding about these REOs, my working group (AG Bäumer) and our collaborators have built PrO_x , $\text{PrO}_x\text{-CeO}_x$ mixed oxide, TbO_x , and SmO_x model systems for surface science studies. Recent work on PrO_x , $\text{PrO}_x\text{-CeO}_x$, and TbO_x model systems will be briefly introduced in this section. The SmO_x model system is the major theme of this dissertation and will be presented in details in the following chapters.

The model studies of PrO_x and $\text{PrO}_x\text{-CeO}_x$ mixed oxides were conducted by my working group (AG Bäumer) and our collaborators from IHP¹, BTU Cottbus-Senftenberg², and Universität Osnabrück. The PrO_x and $\text{PrO}_x\text{-CeO}_x$ mixed oxide films of a thickness range from tens to hundreds of nanometers were grown on boron-doped p-typed Si(111) substrates by molecular beam epitaxy (MBE). In addition, “pure” ceria films were also prepared on the Si substrates for film structural studies and comparison with PrO_x and $\text{PrO}_x\text{-CeO}_x$ mixed oxides. Studies of the film structural reveal that hex- $\text{Pr}_2\text{O}_3(0001)$ growth on a Si(111) substrate is preferred in UHV, because the lateral lattice mismatch between the oxide structure and the Si substrate is only 0.5% compared to 2.7% of the mismatch for cub- $\text{Pr}_2\text{O}_3(111)$. However, the hex- $\text{Pr}_2\text{O}_3(0001)$ film can be transformed into a type-B oriented cub- $\text{Pr}_2\text{O}_3(111)$ by a thermal treatment in N_2 or low pressure O_2 environment [42, 43]. Since Pr can exhibit the 4+ oxidation state, similar to Ce, a mixed-valent (3+/4+) praseodymia, *i.e.* Pr_6O_{11} , is well known and stable under ambient conditions [4]. In UHV conditions, the cub- $\text{Pr}_2\text{O}_3(111)$ film can also be oxidized and form the stable Pr_6O_{11} phase and a co-existence of $\text{PrO}_{2-\delta}$ ($1.83 < \delta < 2$) oxide at an annealing temperature below 500 °C in O_2 background. If the film is further annealed in the same O_2 background at higher temperatures, the praseodymia will exhibit the $\text{PrO}_{2-\delta}$ as well as PrO_2 phases. This oxidation process can be even promoted efficiently by using a cold radio frequency

¹ IHP: Innovations for High Performance GmbH

² BTU Cottbus-Senftenberg: Brandenburgische Technische Universität Cottbus-Senftenberg

oxygen-plasma treatment [44]. The fully oxidized PrO_2 film has been conducted with several studies regarding the reduction behavior, phase transitions, and oxygen mobility [44-46]. The results reveal that a higher oxygen storage capacity of praseodymia was found compared to ceria.

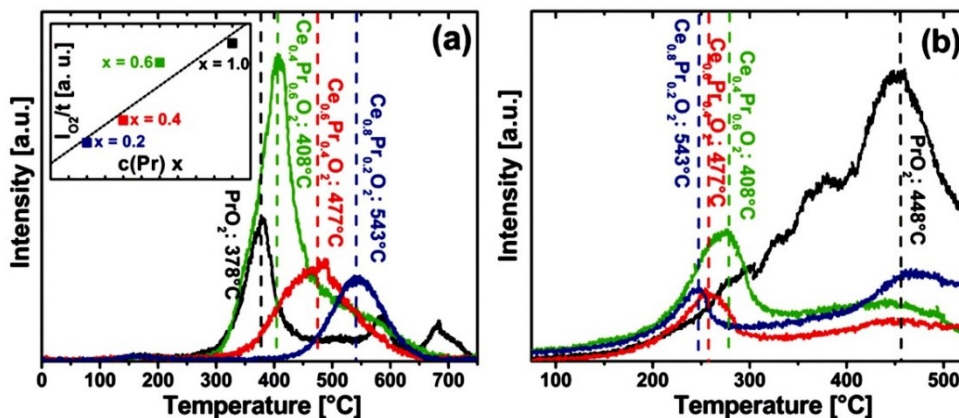


Figure 1. (a) O_2 -TPD spectra collected from the PrO_x - CeO_x mixed oxides with the in situ O_2 -plasma treatment. The inset reveals the I_{O_2} /film thickness versus Pr concentration ratios (X) plot. The I_{O_2} is the integrated intensities of O_2 -TPD peaks and the I_{O_2} /film thickness is used to eliminate the influence of the film thicknesses to the peak intensities. (b) CO_2 -TPD spectra collected from the same samples with the ex situ molecular O_2 treatment [47, 48].

In the system of PrO_x - CeO_x mixed oxides, the oxygen storage capacity is also strongly affected by the Pr concentration which was investigated by conducting a series of TPD experiments, shown in **Figure 1 (a)**. As a result of an increase of Pr concentration, the samples produce molecular oxygen at lower temperatures, moreover, the yield of O_2 production increases. In contrast, ceria exhibits a better hydrocarbon oxidation capability than praseodymia, thus, with the increase of Ce concentration in the mixed oxides, the CO_2 desorption temperature obviously decreases (**Figure 1 (b)**). It has also been found that the Ce^{4+} oxidation state can be stabilized by the $\text{Pr}^{4+}/\text{Pr}^{3+}$ redox system, *i.e.* at elevated temperatures, an oxygen transfer takes place from Pr to Ce, leading to a reduction of Pr^{4+} to Pr^{3+} and the stabilization of Ce^{4+} [47]. Thus, praseodymia exhibits the capability of being an oxygen reservoir in the PrO_x - CeO_x mixed oxide. Based on the result, the PrO_x - CeO_x mixed oxide suggests an important concept, *i.e.* by selecting the concentration of Pr (or Ce) in a mixed oxide, it is able to tune the chemical properties of a sample with dominant oxygen storage capacity or superior hydrocarbon oxidation ability [47, 48].

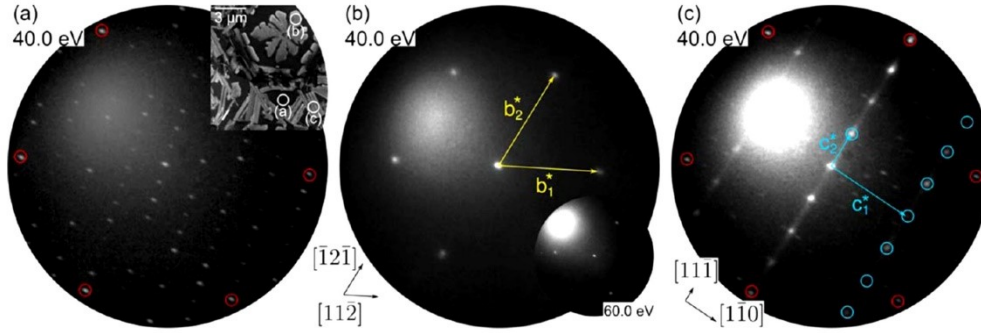


Figure 2. A TbO_x thin film grown on a $\text{Cu}(111)$ substrate studied by LEEM and μLEED . Three areas in the LEEM image (the insert in (a)) show different LEED patterns which are identified as (a) Cu_2O , (b) $\text{TbO}_x(111)$, and (c) $\text{TbO}_x(112)$ [49].

Model studies of terbia (TbO_x) were performed by my working group (AG Bäumer), and our collaborators from the University of Florida. So far, the studies have been mainly focused on the TbO_x oxidation reaction and characterization of film structures. An initial Tb_2O_3 thin film can be grown on $\text{Pt}(111)$ by reactive physical vapor deposition (RPVD). By a plasma-generated oxygen atom beam the Tb_2O_3 thin film could be fully oxidized to TbO_2 at room temperature as shown by temperature programmed desorption (TPD) and X-ray photoelectron spectroscopy (XPS) results. The oxidized TbO_2 thin film can be thermally reduced to the Tb_2O_3 stoichiometry by heating to 1000 K. It has been found that TbO_2 surface lattice oxygen desorbs at lower temperature (ca. 385 K) compared to bulk lattice oxygen desorption (600 K). Additionally, the plasma-generated oxygen atom beam can produce a weakly bound oxygen on the TbO_2 surface and such oxygen desorbs at lower temperatures between 100 K and 270 K [50]. The structural study of a TbO_x thin film grown on a $\text{Cu}(111)$ substrate was conducted by using low-energy electron microscopy (LEEM) and micro-illumination low-energy electron diffraction (μLEED). This work was completed in collaboration with the surface physics group of Prof. Dr. Jens Falta (Institute of Solid State Physics, Universität Bremen). A TbO_x thin film can be grown on the $\text{Cu}(111)$ substrate uniformly in an O_2 background at room temperature, however, the film does not exhibit a long-range order. At elevated temperatures in the O_2 background, a well-crystalline TbO_x thin film consisting of three-dimensional islands with dendrite-like and rectangular structures is found as shown in **Figure 2**. The dendrite-like structure is identified as the $\text{TbO}_x(111)$ phase, whereas the rectangular structure corresponds to the $\text{TbO}_x(112)$ phase. The formation of the $\text{TbO}_x(112)$ phase may be related to an appropriate lattice match between this oxide

phase and the Cu(111) lattice structure, and possibly the existence of ordered Cu₂O structures. Since the TbO_x(112) phase is less stable than the TbO_x(111) phase, the (112) phase is eventually incorporated into the (111) phase when the sample temperature is raised above 530 °C [49].

1.3.2 Studies of samaria

Samaria (SmO_x) has shown its significance by being a high-selectivity catalyst for OCM to produce higher hydrocarbons, and the effort of crystal structures to the chemical reactivity and selectivity has been found on SmO_x for catalyzing the OCM reaction. A plausible speculation for the chemical behavior has been made by considering a primary role of SmO_x surface defects [51]. However, it still remains unclear, and so far no solid evidence has been found to confirm this speculation. A study from “surface science approach” on a SmO_x model system therefore becomes a major option for exploring the nature of SmO_x surfaces. Studies of SmO_x model systems in surface science are somehow very limited. Only few reports were published with respect to some chemical reactions on SmO_x model systems. Back to 1998, T. Kuriyama *et al.* first reported a CO adsorption-desorption study on a SmO_x thin film in UHV [52]. In the same year, the authors published another paper regarding the CO interaction with the interface between SmO_x and a Ru(0001) surface [53]. In 2004, Z. Jiang *et al.* reported a study to demonstrate CO adsorbing on the perimeter sites between SmO_x islands and the Rh(100) surface [54]. Their results reveal that CO only weakly adsorbs on SmO_x surfaces, and more importantly, hint that the existence of perimeter sites in SmO_x-based catalysts is significant for CO reactions due to the presence of the metal surfaces for stabilizing CO up to higher temperatures. Afterwards, the systematic studies for the SmO_x model systems were missing. Not only SmO_x but also other rare-earth sesquioxide model systems are lacking entirely in the context of model studies in catalysis, although sesquioxide is the most common form in the series of REOs. Consequently, the relationship between the surface properties and the chemical reactivity of the oxides remains mostly unknown. Therefore, the main purpose of my PhD project was to setup a SmO_x model system for both surface structural and chemical studies in order to respond to these urgent demands.

High-quality Sm₂O₃ thin films consisting of large, flat, and well-ordered oxide domains on a Pt(111) substrate were successfully prepared by using reactive physical vapor deposition (RPVD). X-ray photoelectron spectroscopy (XPS) and Auger electron spectroscopy (AES) were used mainly for

the film-thickness characterization. For surface structural characterization, scanning tunneling microscopy (STM) and low energy electron diffraction (LEED) were used to investigate the films' structural properties, such as surface morphology and lattice structures. The STM and LEED work will be introduced in the following Chapter 2. To learn about chemical properties and reactivity of the SmO_x model system, carbon monoxide (CO), water (D_2O), and methanol (MeOH) were chosen for adsorption-reaction experiments conducted by temperature-programmed desorption (TPD) and infrared absorption-reflection spectroscopy (IRRAS). CO and water adsorption-reaction studies on ceria and other metal oxide catalysts have been ubiquitous on the basis of two reasons: (1) CO oxidation is essential for eliminating toxic exhaust gas emission and (2) water dissociation is the key for hydrogen production. The MeOH adsorption-reaction study is particularly important for identifying surface active sites of oxide catalysts, because the products from the MeOH reaction are directly determined by the nature of these active sites. Thus, MeOH was also named as a "smart" molecular probe and has been used for characterizing the nature of active sites on different ceria surfaces [55-59]. The CO, D_2O , and MeOH adsorption-reaction studies will be presented in the following Chapter 3.

CHAPTER 2

STRUCTURAL STUDIES OF SAMARIA THIN FILMS (RELEVANT PAPER I)

The most stable form of bulk samaria is sesquioxide (Sm_2O_3) and there are three crystalline types of Sm_2O_3 existing below approximately 2000 °C under ordinary pressures. The three types are named as A (hexagonal), B (monoclinic), and C (cubic). As shown in **Figure 3**, in the temperature range between room temperature and ca. 800 °C the type-C Sm_2O_3 is the most stable crystalline structure which is also known as the cubic bixbyite structure (space group $Ia\bar{3}$). Following the increase of temperature up to ca. 1800 °C, Sm_2O_3 is stable as a monoclinic structure. Between ca. 1800 °C and 2000 °C Sm_2O_3 forms a hexagonal structure. At temperatures above 2000 °C two other crystalline types, *i.e.* H and X may also exist [4].

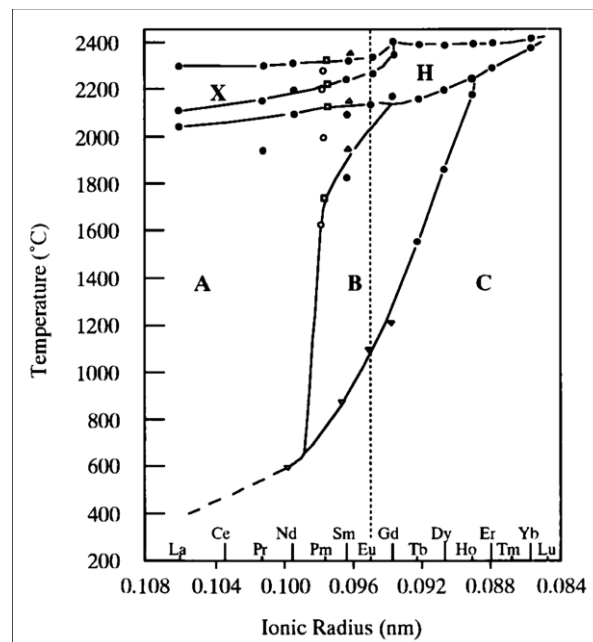


Figure 3. Polymorphic transformation for the rare earth sesquioxides [4].

The bixbyite structure can be obtained by removing two lattice oxygen atoms from each unit cell of a fluorite structure. Representative diagrams of both, a bixbyite and a fluorite structure, are shown in **Figure 4**. From the fluorite structure to the bixbyite structure, ordered oxygen vacancies form and metal cations relax from their original positions in the face-centered cubic (fcc) sublattice. The coordination numbers of metal cations are therefore reduced from eight to six. As a result, the cubic symmetry consisting of metal cations in the fluorite structure vanishes, and the volume of a unit cell of the bixbyite structure is about eight times larger than that of the fluorite structure.

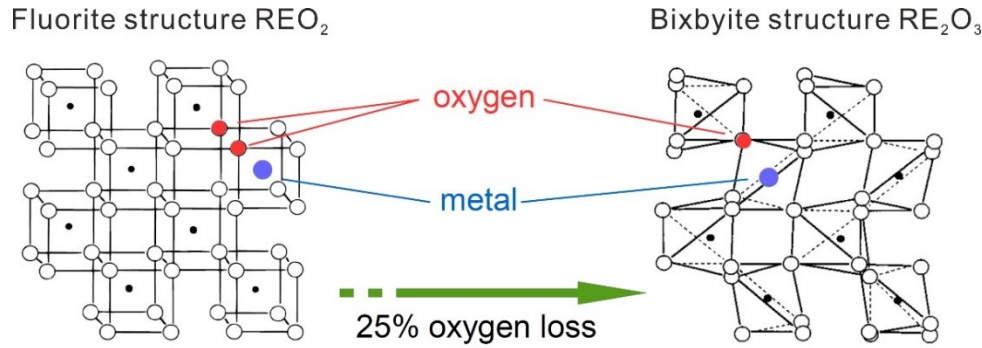


Figure 4. Representations of REO_2 fluorite and RE_2O_3 bixbyite structures. (Reproduced from ref. [4])

Because the bixbyite structure is short of a simple hexagonal symmetry, it is difficult to anticipate how SmO_x preferring a bixbyite structure in bulk will grow as thin films on a hexagonally closed-packed metallic substrate, *e.g.* the Pt(111) surface. Thus, the priority of building a SmO_x model system is to generate high-quality SmO_x thin films and further study their structural properties. In Chapter 2 the structural studies of SmO_x thin films grown on Pt(111) are presented based on experimental results from LEED and STM.

2.1 As-prepared Sm_2O_3 thin films

A high-quality Sm_2O_3 thin film exhibiting typical hexagonally shaped islands can be grown on a Pt(111) substrate via well-controlled RPVD, as shown in **Figure 5 (a)**. A line scan over a Sm_2O_3 island in **Figure 5 (a)** reveals that the step height of the island's first layer is 3.1 Å (shown in **Figure 5 (b)**) which is very close to the average distance of a O-Sm-O trilayer along the $\langle 111 \rangle$ direction of the

type-C Sm_2O_3 bixbyite structure [60]. The estimated thickness of the second layer (1.1 Å) is smaller than that of the first layer which is most likely due to a different tunneling condition through this layer and the first layer. The atomically resolved STM image shown in **Figure 5 (c)** reveals that Sm cations array into a hexagonal arrangement in the sublattice in registry with Pt(111), whereas oxygen vacancies randomly distribute within the Sm_2O_3 structure. This observation demonstrates that the as-prepared Sm_2O_3 thin film exhibits a defective fluorite structure rather than a bixbyite structure as expected for its bulk. The result also implies that the way how a sesquioxide thin-film grows may be determined by the oxide-metallic substrate interaction. The average distance between two adjacent Sm cations is 3.83 ± 0.05 Å estimated from the atomically resolved STM image (**Figure 5 (c)**), which shows good agreement with the observation in LEED. **Figure 6 (a) – (e)** shows the LEED patterns collected from as-prepared Sm_2O_3 thin films with different coverages, and a hexagonal (1.37 x 1.37) superstructure in registry with the Pt(111) (1 x 1) spots adopts to the lattice arrangement of Sm cations, thus, the estimated lattice constant from LEED spots is 3.81 Å.

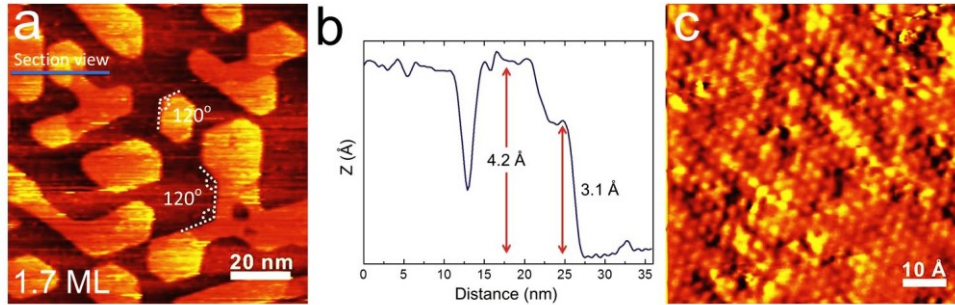


Figure 5. (a) Topographic STM image of a 1.7 ML Sm_2O_3 (111) thin film on Pt(111). (b) Height profile of a Sm_2O_3 island as estimated from the measurement of section view in (a). (c) Atomically resolved image showing a hexagonal arrangement of Sm atoms and randomly structural defects as well.

At film coverages between ~ 1 and 3 ML, apart from the Pt(111) and Sm_2O_3 (111) main spots, additional spots are observed in LEED patterns. These additional spots are arrayed into a hexagonal arrangement and form a quasi – 3 x 3 superstructure in registry with the Sm_2O_3 lattice. A real-space model consisting of the superposed Sm and Pt lattices was generated to analyze this pattern, afterwards a fast Fourier transform (FFT) [61] of the real-space model was applied to simulate its diffraction pattern. The FFT result shows good agreement with the quasi – 3 x 3 pattern and provides evidence for double diffraction at the coincidence lattice between the Pt(111) surface and the Sm sublattice

leading to the formation of the quasi – 3×3 superstructure in LEED. A schematic representation of the quasi – 3×3 superstructure is shown in **Figure 6(f)**. Along the line connecting the $(0, 0)$ and $\text{Pt}(0, 1)$ spots, the additional spots generated by the diffraction from the coincidence lattice are located at the $(0, 3/11)$ and $(0, 5/11)$ positions, and the main-order Sm spot is located at the $(0, 8/11)$ position.

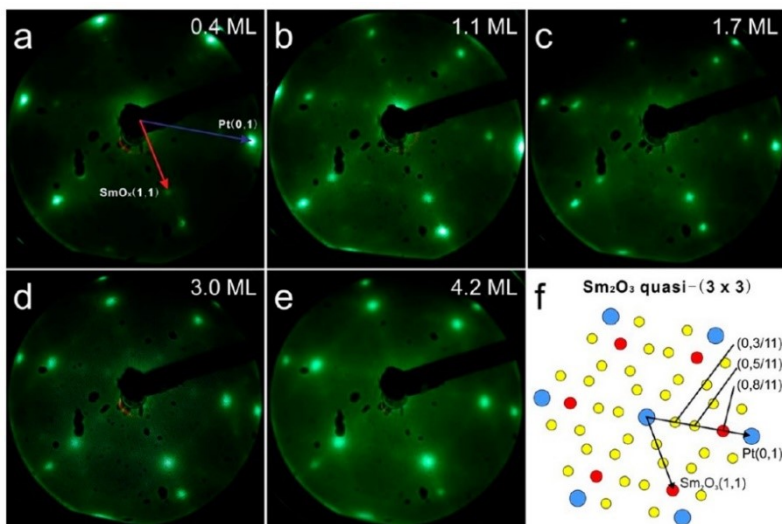


Figure 6. LEED patterns collected from different Sm_2O_3 thin-film coverages on $\text{Pt}(111)$: (a) 0.4 ML, $E = 58$ eV, (b) 1.1 ML, $E = 48$ eV, (c) 1.7 ML, $E = 56$ eV, (d) 3.0 ML, $E = 52$ eV, and (e) 4.2 ML, $E = 56$ eV. (f) A schematic representation of the quasi – 3×3 superstructure.

2.2 Thermal reduction of Sm_2O_3 thin films

The bulk Sm_2O_3 sesquioxide is, in general, not discussed as a reducible oxide, because a reduction from the Sm_2O_3 sesquioxide to a SmO monoxide only occurs under extreme experimental conditions, *i.e.* in a pressure range of 15 – 80 kbar and in a temperature range of 500 – 1200 °C [3]. Surprisingly, in this work it has been demonstrated that a Sm_2O_3 thin film grown on $\text{Pt}(111)$ shows the capability of being partially reduced to SmO according to STM and LEED studies. The partially reduced SmO_x thin film can be produced by thermally annealing an as-prepared Sm_2O_3 thin film at 1000 K for 30 min in UHV. *Experimental details are described in the attached paper I.* The STM images reveal that a partially reduced SmO_x surface consists of extensively flat $\text{Sm}_2\text{O}_3(111)$ terraces and crack-like phases, shown in **Figure 7 (a)** and **(d)**. In atomically resolved STM images shown in **Figure 7 (c)** and **(e)**, the crack-like phase gives rise to a square periodicity with a lattice parameter of 3.56 \AA , which corresponds well

to a rocksalt SmO(100) phase. The hexagonal arrangement of Sm atoms in the Sm₂O₃(111) phase with the lattice parameter of 3.83 Å is still visible on the partially reduced surface, shown in **Figure 7 (b)**. The SmO(100) phase is nonpolar and it is the most stable facet of bulk rocksalt SmO, however, bulk SmO is only obtained under extreme conditions. The formation of SmO(100) phases found in this work implies that the interaction between SmO_x and Pt(111) may play an important role for promoting the partial reduction of Sm₂O₃ to SmO.

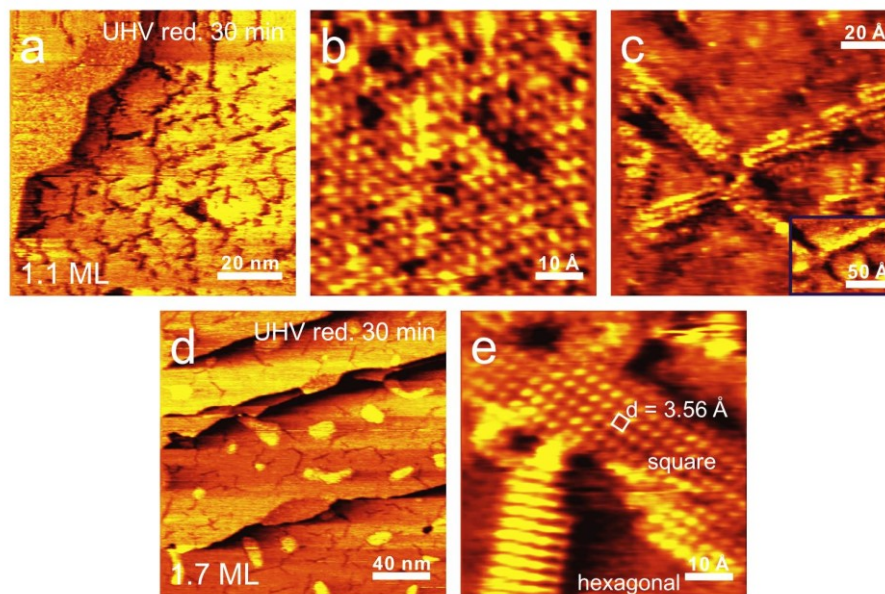


Figure 7. (a) Topographic and (b) – (c) atomically resolved STM images collected from the 1.1 ML partially reduced SmO_x thin film on Pt(111). (d) Topographic and (e) atomically resolved STM images from the 1.7 ML reduced thin film.

According to the STM results, SmO(100) phases are mainly generated in the first oxide layer which is closest to the Pt(111) surface. Meanwhile, the occurrence of SmO is also accompanied by a SmO_x thin-film wetting behavior, resulting in a nearly continuous film covering the Pt(111) substrate, also shown in **Figure 7 (a)** and **(d)**. The quasi – 3 x 3 superstructure vanishing in LEED (**Figure 8**) after partial reduction provides additional evidence for the SmO(100) formation in the first layer. Apart from the disappearance of the quasi – 3 x 3 structure, additional satellite spots forming a hexagonal arrangement centered by the Sm₂O₃(111) (1 x 1) main spots are observed in LEED (**Figure 8 (a)** and **(b)**). The satellite structure is only observed on a partially reduced SmO_x thin film at coverages between ~1 and 2 ML, which may correspond to a coincidence lattice of SmO(100) and

$\text{Sm}_2\text{O}_3(111)$ domains as indicated by the consistency of simulated and measured LEED patterns. *The simulated LEED pattern is shown in the attached paper I.* While the SmO_x coverage is above 3 ML, no obvious changes are seen in LEED (**Figure 8 (c)**) after the thermal reduction process.

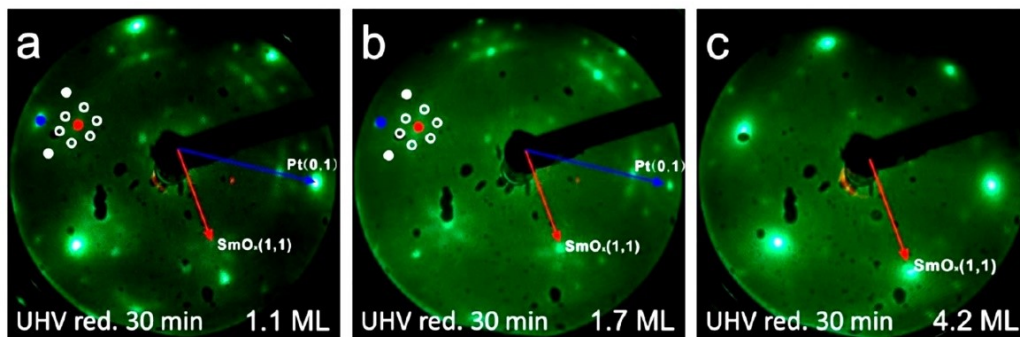


Figure 8. LEED patterns collected from the partially reduced SmO_x thin films on Pt(111) with initial Sm_2O_3 coverages of (a) 1.1 ML, $E = 64$ eV, (b) 1.7 ML, $E = 58$ eV, and (c) 4.2 ML, $E = 43$ eV.

X-ray photoelectron spectroscopy (XPS)³ provides spectroscopic evidence revealing an electronic change of a SmO_x thin film after partial reduction. Sm 3d and O 1s spectra collected from an as-prepared Sm_2O_3 thin film reveal a typical Sm_2O_3 XPS spectroscopic feature [62], shown in **Figure 9**. After the thermal reduction process, both Sm 3d and O 1s photoemission peaks shift ca. 0.5 – 1.0 eV to higher binding energies. This shift is not simply a chemical shift but signifies a band-bending effect [63, 64], which can arise when an electronic-structure change occurs on a crystalline film surface and/or the interface between the film and a metallic substrate. Thus, the band-bending effect is likely induced by surface structural changes on the SmO_x thin film and/or SmO formation at the interface between Sm_2O_3 layers and the Pt(111) substrate. Overall, the treatment of thermal reduction of Sm_2O_3 thin films leads to significant geometric as well as electronic changes.

³ The XPS work was published in the relevant paper III.

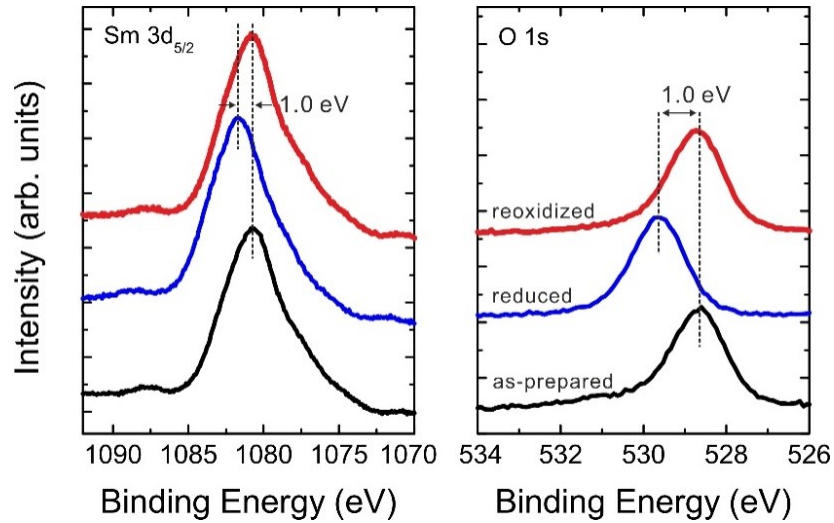


Figure 9. Sm $3d_{5/2}$ and O $1s$ core level XPS spectra collected from a 2.8 ML as-prepared Sm_2O_3 thin film grown on Pt(111), and the film after reduction and reoxidation processes.

2.3 Reoxidation of reduced SmO_x thin films

As already mentioned, bulk Sm_2O_3 is not considered as a reducible material, nevertheless the evidence has shown that a Sm_2O_3 thin film grown on Pt(111) can be partially reduced by a thermal treatment (1000 K in UHV for 30 min). A further study suggests that the partial reduction is reversible by re-annealing a reduced SmO_x thin film in O_2 background at 1000 K for 10 min. STM and LEED results reveal that an initial Sm_2O_3 crystalline structure can be regained by the reoxidation process, thereby $\text{SmO}(100)$ phases are easily oxidized back to $\text{Sm}_2\text{O}_3(111)$ phases. After the reoxidation process, the satellite pattern vanishes whereas the quasi – 3×3 superstructure is restored in LEED as shown in **Figure 10 (a)** implying the success of the reoxidation process. The STM image in **Figure 10 (b)** reveals that the treatment results in a film dewetting behavior which significantly improves film flatness as well as connectivity among Sm_2O_3 domains, compared with its as-prepared condition.

A spectroscopic evidence also implies the success of reoxidation via monitoring Sm $3d$ and O $1s$ XPS spectra of a reoxidized film also shown in **Figure 9**. The treatment of reoxidation induces an inverse band bending effect that both Sm and O spectra downshift by ca. 0.5 – 1.0 eV back to its as-prepared (oxidized) condition. Thus, the spectroscopic evidence suggests that not only the atomic structure but also the electronic property of a Sm_2O_3 thin film can be well restored through this

treatment. Overall, it is demonstrated that even though a low lattice oxygen mobility in SmO_x is expected, the model study of SmO_x thin films grown on Pt(111) shows that the thin film is capable to achieve oxidation/reduction cycles under well-controlled conditions.

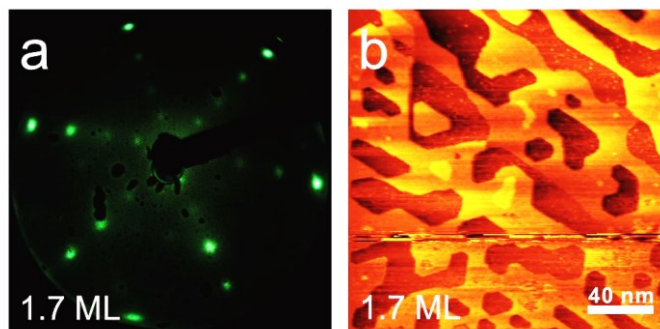


Figure 10. (a) LEED pattern, $E = 58.5$ eV and (b) STM topographic image collected from the 1.7 ML reoxidized Sm_2O_3 thin film. Highly interconnected Sm_2O_3 domains can be obtained after the reoxidation process.

2.4 Adjustable lattice structures: from quasi – to perfect – 3×3

While SmO_x thin films grow on a Pt(111) substrate, a small extent of SmO_x lattice compression is tolerated according to LEED and STM studies. It has been known that the rocksalt $\text{SmO}(100)$ phases can be generated by partially reducing an as-prepared Sm_2O_3 thin film, thus a designated method was proposed for preparing $\text{SmO}(100)$ phases in a partially reduced SmO_x thin film: a certain amount of Sm_2O_3 was prepared as a thin film on Pt(111) at 600 K and subsequently the half equivalent amount of Sm atoms was deposited on the thin film, afterwards the sample was annealed in UHV at 800 K for 10 min instead of annealing at 1000 K for 30 min. The annealing temperature of 800 K is not sufficient for reducing a Sm_2O_3 thin film, however, additional Sm atoms can react with the Sm_2O_3 thin film to produce $\text{SmO}(100)$ phases at the temperature. A similarly designated method has been used for preparing Ce_2O_3 thin films via an interfacial reaction between Ce atoms and CeO_2 [65]. In **Figure 11** the STM image shows that certainly large $\text{SmO}(100)$ domains can be produced via this method.

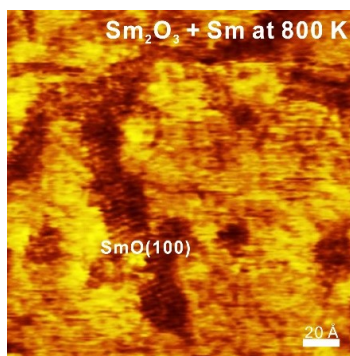


Figure 11. Atomically resolved STM image recorded from the reduced SmO_x thin film prepared from additional Sm atoms reacting with a Sm_2O_3 thin film at 800 K for 10 min.

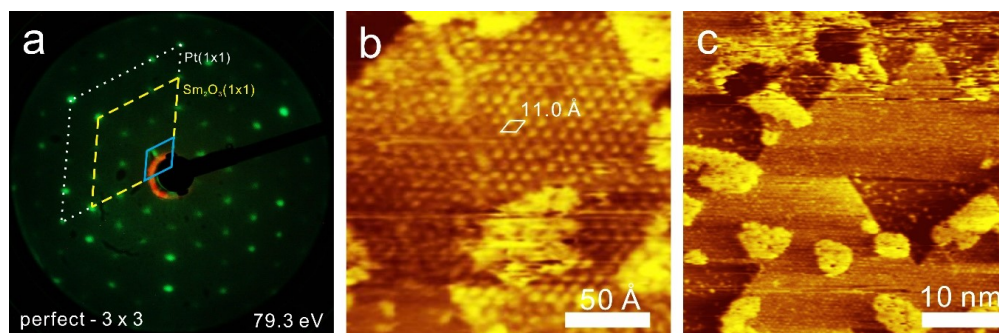


Figure 12. (a) LEED pattern obtained after reoxidizing the reduced SmO_x thin film. (b) Atomically resolved STM image and (c) topographic STM image of the reoxidized Sm_2O_3 thin film.

A treatment of reoxidation was also carried out on this sample via annealing in O_2 background at 1000 K for 10 min. Afterwards, intriguingly a perfect 3×3 pattern instead of the quasi- 3×3 pattern arises in LEED as shown in **Figure 12 (a)**, indicating that the film's lattice constant decreases and a hexagonal (1.33×1.33) superstructure forms. Following the interpretation for the formation of the quasi- 3×3 pattern, the same trend of thought for explaining the perfect- 3×3 pattern is followed. Thus, it is due to a double diffraction from a coincidence lattice between the Pt(111) substrate and $\text{Sm}_2\text{O}_3(111)$ domains, wherein a reduction of the distance of adjacent Sm cations in the sublattice to 3.70 \AA is expected. The perfect- 3×3 superstructure is also verified by an atomically resolved STM image shown in **Figure 12 (b)**. A perfectly hexagonal arrangement of protrusions is monitored exhibiting a measured distance of 11.0 \AA between two adjacent protrusions. The distance fits well to four times the Pt-Pt lattice constant and three times the Sm-Sm lattice constant. The perfectly hexagonal arrangement is therefore confirmed as the coincidence lattice between the Pt substrate and

Sm₂O₃ domains. The formation of the perfect – 3 x 3 superstructure also requires large Sm₂O₃ domains at the first oxide layer on the Pt(111) substrate. In the STM topographic image (**Figure 12 (c)**) indeed there is a nearly continuous Sm₂O₃ layer lying on the Pt substrate, and additional triangular holes which is speculated to represent exposed Pt areas exist in the Sm₂O₃ layer. The reason of why the lattice constant of Sm-Sm in the sublattice changes (leading to the perfect – 3 x 3 pattern) is still unclear, nevertheless, one can expect that the interaction between the first Sm₂O₃ layer and the Pt substrate must play a predominant role.

2.5 Summary of the structural studies

The structural studies of SmO_x thin films based on LEED and STM results have shown that high-quality Sm₂O₃ thin films consisting of well-ordered, large, and flat oxide domains can be grown on Pt(111) by RPVD and post-annealing in an O₂ background at 1000 K. The Sm₂O₃ thin films exhibit a fluorite defective structure instead of a bixbyite structure which is found in bulk Sm₂O₃, suggesting that an oxide-metallic substrate interaction plays an important role in determining a sesquioxide thin-film structure. At a film coverage between about 1 and 3 ML, a quasi – 3 x 3 LEED pattern is observed which is generated by double diffraction from a coincidence lattice between Pt(111) and Sm₂O₃. Rocksalt SmO(100) phases are obtained after partially reducing the Sm₂O₃ thin films, meanwhile, the reduction process leads to a film wetting behavior. Reoxidation of the reduced SmO_x thin films restores the Sm₂O₃(111) lattice structure, and improves the connectivity among Sm₂O₃ domains and the film flatness. The film wetting/dewetting cycle achieved by the reduction/reoxidation processes is found in the STM and LEED studies. The status of wetting or dewetting can be taken as an indication for the rate of SmO_x oxidation conditions. In contrast, the film-structural status of thicker SmO_x thin films (thickness > 3 ML) does not respond strongly to the reduction/reoxidation processes, *i.e.* the SmO_x thin films fully cover on Pt(111), thus no wetting/dewetting behavior can be observed. Additionally, no obvious changes in LEED patterns are monitored from the thicker thin films during the reduction/reoxidation processes. An alternative way for preparing a partially reduced SmO_x thin film was developed by depositing Sm atoms onto a Sm₂O₃ thin film and post-annealing the sample at 800 K. Such partially reduced thin film after the reoxidation process shows a perfect – 3 x 3 instead of the quasi – 3 x 3 pattern, indicating a small degree of flexibility in the lattice.

CHAPTER 3

SURFACE CHEMISTRY OF SAMARIA THIN FILMS (RELEVANT PAPER II AND III)

The structural studies of SmO_x thin films have been introduced in Chapter 2, showing that high-quality Sm_2O_3 thin films can be grown on the Pt(111) substrate by RPVD. The well-controlled preparation of a specific film coverage leads to the possibility of studying chemical behavior of a continuous SmO_x thin film fully covering the Pt(111) substrate as well as of SmO_x islands partially covering Pt(111) by conducting different gas molecules onto these surfaces for adsorption-reaction experiments. A sample constituted by oxide islands grown on a metal substrate is a so-called inverse catalyst exhibiting certain catalytic capabilities, which usually are not found in its conventional system (metal nanoparticles grown on an oxide substrate) [27, 66-68]. In this respect, scientists are focusing on developing inverse catalysts and understanding the fundamental properties of these catalysts. For instance, inverse catalysts consisting of CeO_x or TiO_x nanoparticles and metallic substrates have shown promising activity towards the water-gas-shift (WGS) reaction [27]. Recent studies reveal that in the inverse WGS catalysts the oxide surface plays an important role for water dissociation and CO oxidation, meanwhile the metallic substrate is responsible for CO adsorption and destabilizing intermediates produced from the CO-OH reaction [67].

The studies of chemical reactivity and behavior were conducted on both the continuous SmO_x thin film as well as the discontinuous thin film which consists of SmO_x islands and exposed Pt areas by reacting with CO, D_2O , and MeOH. For simplicity, the continuous thin films and discontinuous thin films are named as “thin films” and “islands”, respectively. Main adsorption-reaction studies carried out by TPD and IRRAS will be presented in the following sections, and the results show that especially the SmO_x islands exhibit unique chemical behavior and impressive reactivity.

3.1 CO chemistry – CO adsorption and reaction

CO adsorption-reaction studies on a Sm_2O_3 thin film (4.3 ML) and Sm_2O_3 islands (1.3 ML) were carried out by using TPD. By dosing 5 Langmuir⁴ of CO on the Sm_2O_3 thin film at 96 K, CO desorbed from the film quickly at 113 K. The CO-TPD result is shown in **Figure 13**. It indicates that CO only weakly adsorbs on the Sm_2O_3 surface. The result is consistent with previous studies of CO adsorption-desorption on SmO_x surfaces which were introduced in the section 1.3 [52-54]. By considering a first-order desorption of CO from the surface, the activation energy of CO desorption can be estimated as 28.7 kJ mol^{-1} by using Redhead's equation and assuming a frequency factor of 10^{13} s^{-1} [69]. It should be noted that the CO desorption signal from the Pt substrate at 350 K – 500 K is not observed from this sample, suggesting that the Sm_2O_3 thin film entirely covers the Pt(111) surface.

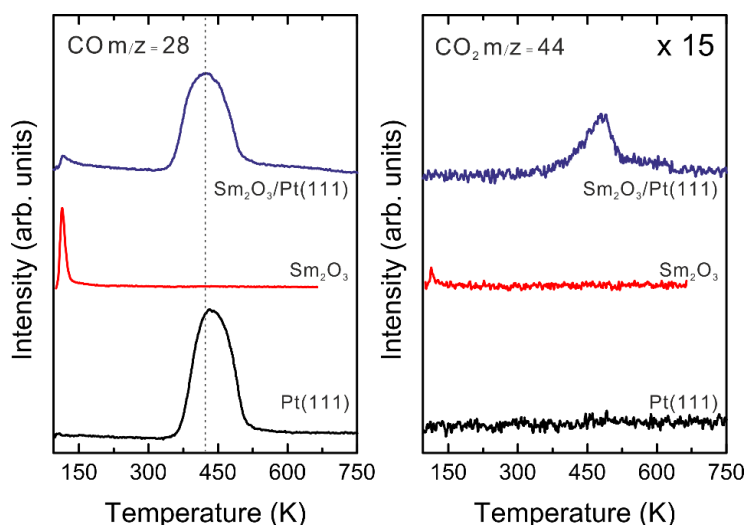


Figure 13. CO- and CO_2 -TPD spectra collected from a Pt(111) surface, an as-prepared continuous Sm_2O_3 thin film, and an as-prepared Sm_2O_3 islands, respectively, after dosing 5 L CO at 96 K.

In contrast, both CO desorption signals contributed by the Sm_2O_3 surface and the Pt(111) substrate are obtained from the Sm_2O_3 islands (**Figure 13**). Importantly, two interesting findings should be mentioned here. First, the CO desorption signal from Pt(111) downshifts by 15 K compared to the “bare” Pt(111) surface. Second, a CO_2 -TPD signal arising at 400 K – 500 K from the sample

⁴ One Langmuir (L) is defined by the exposure of a surface to a gas ($P = 1.0 \times 10^{-6}$ Torr) for one second.

indicates successful CO oxidation. The downshift of the CO desorption peak suggests a decrease of activation energy of CO desorption by 4.1 kJ mol^{-1} from the Pt surface, implying an increase of the CO-CO long-range repulsive interaction due to the decrease of the mean distance between two adjacent CO molecules. The result suggests a CO spillover taking place from Sm_2O_3 islands to exposed Pt areas at elevated temperatures. The CO_2 desorption peak locates at that temperature at which CO desorption occurs from Pt(111), suggesting CO oxidation at the perimeter sites where Sm_2O_3 provides available oxygen to oxidize CO. Two possible oxygen sources, *i.e.* lattice oxygen and surface hydroxyls are considered to contribute to CO_2 formation. If the reaction of hydroxyls and CO was dominant, the H_2 product in TPD spectra should be observed. Due to no observation of H_2 formation during this TPD experiment, lattice oxygen on the perimeter sites as cause for CO oxidation is concluded. Furthermore, CO_2 production can be eliminated by operating repeated CO-TPD experiments on the Sm_2O_3 islands, or treating the islands with thermal reduction. These results again reveal the contribution of lattice oxygen for CO oxidation.

3.2 Water chemistry

3.2.1 Water (D_2O) adsorption and dissociation

Water (D_2O) TPD experiments were also carried out on the Sm_2O_3 thin film and Sm_2O_3 islands by dosing 10 Langmuir of D_2O onto each sample at 96 K. A main D_2O desorption peak at 190 K accompanied by a tail up to ca. 250 K – 300 K is observed on both D_2O -TPD spectra collected from the Sm_2O_3 thin film and islands, shown in **Figure 14**. The main D_2O peak is assigned as a non-dissociative molecular D_2O desorption, whereas the tail up to higher temperatures is assigned as a recombinative D_2O desorption which is not observed in the D_2O -TPD spectrum from the Pt(111) substrate. Based on the nature of the Sm_2O_3 surface introduced in Chapter 2 according to STM studies, OD and D species from D_2O dissociation staying on different sites on the Sm_2O_3 surface is expected. OD species (nucleophilic) stay on Sm-cation sites or surface vacancies while D species (electrophilic) stay on O-anion sites. Following the elevated temperatures above 300 K, the D_2O chemistry behaves differently on the Sm_2O_3 thin film and islands. Another D_2O recombination peak appears at 520 K on the Sm_2O_3 thin film, whereas no D_2O recombination peak but a D_2 peak arises at 600 K on the Sm_2O_3 islands. Both D_2O recombination and D_2 formation suggest that OD (and D) species are stable

on Sm_2O_3 surfaces up to ca. 450 K – 500 K. Different products desorbing from the thin film and islands may suggest a different reactive nature of the two surfaces. Because the D_2 desorption temperature (600 K) from the islands is higher than the desorption temperature (520 K) of the recombinative D_2O peak from the thin film, a stronger binding of OD species on the islands than on the thin film is speculated which may block the pathway of D_2O recombination and therefore induce D_2 formation.

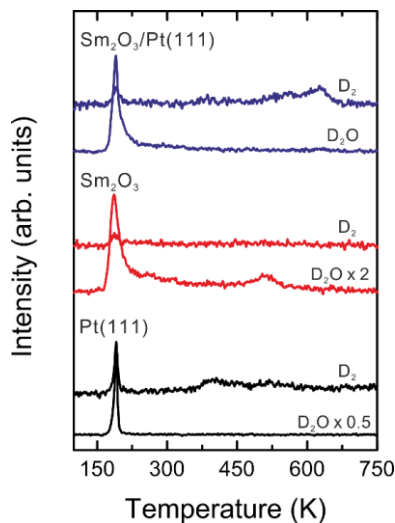


Figure 14. D_2O - and D_2 -TPD spectra collected from the Pt(111), the as-prepared continuous Sm_2O_3 thin film, and the as-prepared Sm_2O_3 islands.

In Chapter 2 it has been described that the SmO_x film's status can be significantly altered by thermal reduction, *i.e.* Sm_2O_3 can be partially reduced to SmO and a film-wetting behavior occurs. To understand how D_2O chemically responds to different SmO_x oxidation conditions, *e.g.* oxidized and reduced surfaces, D_2O adsorption-reaction experiments were also performed on both reduced SmO_x thin film and islands. The D_2O - and D_2 -TPD results are shown in **Figure 15**. The features of D_2O -TPD desorption signals stay similar when reduced SmO_x thin films are compared to as-prepared Sm_2O_3 thin films. The main D_2O peak remains due to non-dissociative D_2O desorption, however, both recombinative D_2O desorption signals shift to higher temperatures. The tail ends at 450 K and the peak emerges at 650 K. Both shifts indicate that OD species from D_2O dissociation exhibit highly thermal stability on the reduced surface. Particularly, the integrated area of the tail increases by 1.8 times suggesting that thermal reduction is capable of promoting D_2O dissociation.

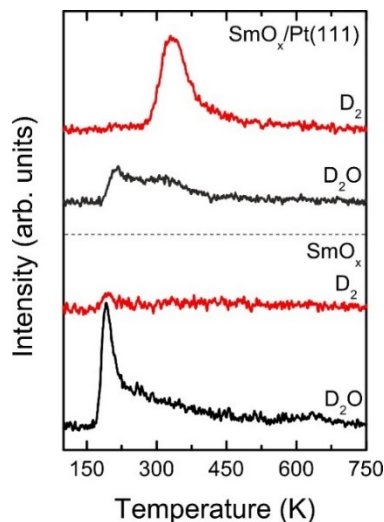


Figure 15. D₂O- and D₂-TPD spectra collected from the reduced continuous SmO_x thin film and the reduced SmO_x islands.

The TPD result collected from the reduced SmO_x islands shows obvious changes in the features of both D₂O and D₂ desorption signals (**Figure 15**). It is known that the reduced SmO_x islands cover ca. 90 % of the Pt(111) surface based on the Pt area estimation obtained from CO-TPD experiments (*shown in the attached paper II*), therefore both non-dissociative and recombinative D₂O molecules mainly desorb from the SmO_x surface but not from the free Pt areas. A clear D₂ desorption peak emerges at 325 K in the D₂-TPD spectrum. The D₂ formation reveals that a part of OD or O species from D₂O dissociation remains on the SmO_x surface. Apparently thermal reduction influences the chemical behavior of the reduced islands stronger than of the reduced thin film, which may be explained by taking the influence of the film thickness into consideration. As shown in Chapter 2, the STM study revealed that the response of SmO_x thin films to thermal reduction is strongly dependent on the film thickness. Thermal reduction particularly causes obviously SmO_x electronic and morphologic changes while the film thickness is below 3.0 ML, because the influence of SmO formation at the interface between Sm₂O₃ layers and the Pt substrate becomes leading on thinner films. Certainly, D₂O dissociation is even promoted on the reduced SmO_x islands by estimating the integrated area of the D₂O recombination signal. The result shows that 4.5 times more recombinative D₂O molecules are produced from the reduced islands than from the oxidized one. The desorption temperature of the D₂-TPD peak is near the temperature of molecular hydrogen (H₂) desorption from a Pt(111) surface

indicating a D spillover effect, *i.e.* D species from D₂O dissociation on the SmO_x surface diffuse onto the exposed Pt areas and subsequently recombine and desorb as D₂ from the Pt surface.

3.2.2 CO assistance for D₂ production

To extend surface chemistry studies on SmO_x to more complicated reactions, a sample consisting of SmO_x islands and exposed Pt areas seems to be a suitable model system. For example, in the WGS reaction two possible mechanisms are proposed as (1) the redox mechanism and (2) the associative mechanism, and both mechanisms can be achieved by CO oxidation and water dissociation [70-74]. The CO-TPD studies (section 3.1) reveal two important results, *i.e.* above room temperature CO only remains on the exposed Pt surface, and the perimeter sites between Sm₂O₃ islands and Pt are able to provide available lattice oxygen for CO oxidation. The D₂O-TPD studies show that D₂O dissociation mainly takes place on SmO_x surfaces, which can be even promoted especially on the reduced SmO_x islands. The fact that above room temperature CO and OD species stably remain on Pt and SmO_x respectively leads to a question, *i.e.* how do CO and OD species interact with each other especially on the perimeter sites? Thus CO/D₂O coadsorption-reaction experiments were conducted on SmO_x islands, and such experiments can be also considered as tests for a model WGS reaction.

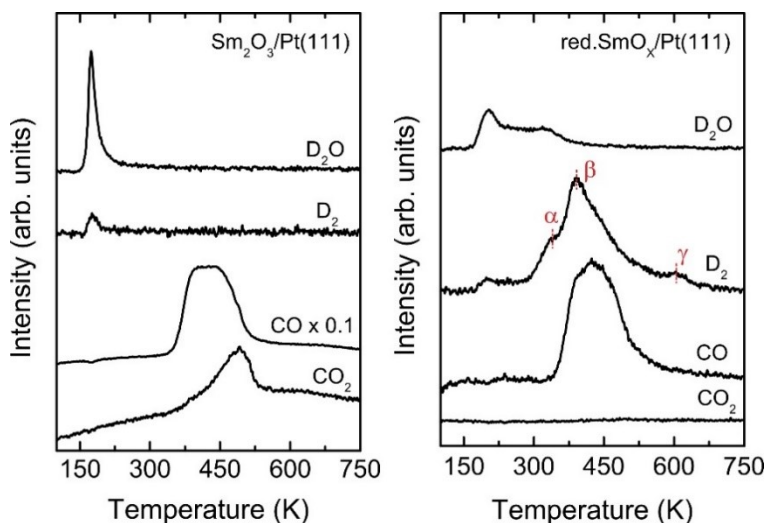


Figure 16. TPD spectra collected from the as-prepared and the reduced SmO_x islands with 5 L pre-dosed CO and 10 L D₂O.

To perform the CO + D₂O coadsorption-reaction experiments, the exposed Pt areas were pre-covered by CO and afterwards D₂O was dosed onto both Pt and SmO_x surfaces for TPD experiments. *The experimental details are described in the attached paper II.* **Figure 16** shows the TPD results from the CO + D₂O experiments on the as-prepared Sm₂O₃ islands (**left**) and the reduced SmO_x islands (**right**). Note that the intensity of the CO-TPD spectrum recorded from the as-prepared Sm₂O₃ islands is divided by 10. Obviously there is no significant difference in CO and CO₂-TPD spectra collected from the as-prepared Sm₂O₃ islands compared to the results obtained from the CO-TPD experiments without D₂O involvement, suggesting that CO/D₂O co-existence does not lead to a strong impact on CO desorption and reaction on the sample. In contrast, the D₂O desorption peak slightly downshifts by 15 K in this case with CO/D₂O co-existence on Pt compared to that without CO participation. The downshift reveals a decrease of activation energy of D₂O desorption due to a repulsive D₂O-CO interaction which destabilizes the D₂O-D₂O interaction [75]. Because CO only adsorbs on exposed Pt surfaces, the downshift therefore implies that the non-dissociative D₂O-TPD signal is mainly contributed by D₂O desorption from the CO-covered Pt areas or the perimeter sites between Sm₂O₃ islands and Pt. Apart from this result, there was no evidence for interaction between CO and OD species observed on the as-prepared Sm₂O₃ islands.

The same CO+D₂O TPD experiment was also carried out on the reduced SmO_x islands (**Figure 16, right**). Note that the intensity of the CO-TPD signal becomes much smaller as expected while the as-prepared Sm₂O₃ islands are thermally reduced. Because SmO_x islands spread onto the Pt surface and form a wetting film during thermal reduction, as a result, less free Pt area, responsible for CO adsorption, is exposed after thermal reduction. No CO₂ formation implies that available lattice oxygen on the perimeter sites is eliminated by thermal reduction, which therefore limits CO oxidation on the reduced SmO_x islands. The D₂O-TPD signals show a similar feature as that from the D₂O-TPD experiment without CO participation (section 3.2.1), supporting the idea that the SmO_x surface takes the major responsibility for D₂O desorption.

Intriguingly, in the D₂-TPD spectrum (**Figure 16, right**) a pronounced D₂ desorption signal arises in a broad temperature range between 300 K and 650 K. This broad D₂-TPD signal consists of three contributions named as α , β , γ . The peak α has been identified in the D₂O-TPD experiment without CO involvement as the D₂ desorption peak contributed by exposed Pt areas due to the D spillover

effect (section 3.2.1). The new contributions β and γ emerging in the temperature range of CO desorption from the Pt surface expose the fact that the interaction between CO and OD species indeed occurs presumably on the perimeter sites. Nevertheless, the interaction is not seen on the as-prepared Sm_2O_3 islands indicating that the chemical property of a SmO_x surface is strongly dependent on its surface status, *e.g.* oxidation states, surface defects/vacancies, etc. Because OD (and D) species are stabilized on a reduced SmO_x surface based on the D_2O -TPD results (section 3.2.1), it suggests an increased interaction between the oxygen of hydroxyl and the reduced surface due to surface vacancy formation. A theoretical work on CeO_x surfaces [76] may explain the increased interaction between O and the reduced surface due to a local accumulation of positive charges generated around vacancies on the reduced surface. As a result, the O-D bond is weakened and the interaction between CO and OD therefore becomes dominant leading to D_2 formation. Two possible reactions are proposed regarding the CO-OD interaction: (1) a hydrogen bond forms between CO and OD, which further weakens the O-D bond and eventually leads to D_2 formation, or (2) CO and OD react and produce formate as intermediate species which further decomposes to CO, D_2 , and O. Decomposition of formate species to CO has been found and discussed in the reverse WGS reaction [77, 78] and methanol decomposition [79]. The reaction of CO and OD on the perimeter sites undergoing either way must remain O on the sample which may desorb as O_2 , or oxidize CO to CO_2 , or reoxidize the perimeter sites. Based on the TPD results showing no O_2 and CO_2 formation, O staying and partially reoxidizing the perimeter sites is therefore deduced.

3.3 Methanol chemistry

3.3.1 Methanol (MeOH) adsorption and reaction

Studies of MeOH adsorption and reaction on metal oxide surfaces have been increasingly paid attention to, because MeOH is considered as a “smart” molecular probe for characterizing chemical properties of oxide surfaces [80, 81]. How a MeOH molecule dissociates and reacts on an oxide surface is strongly influenced by the nature of the oxide surface, thus the products of the MeOH reaction are able to reflect the nature of active sites on the oxide surface. For instance, MeOH is dehydrated and forms dimethyl ether on Lewis and Brønsted acid sites, is oxidatively-dehydrogenated and forms formaldehyde on redox sites, and is dehydrogenated and forms CO and CO_2 on basic sites. Based on

this concept, MeOH adsorption-reaction studies were performed by using TPD and IRRAS in order to learn about fundamental properties of active sites on SmO_x thin films. The MeOH adsorption-reaction experiments were also conducted on both continuous and discontinuous SmO_x thin films. Also for simplicity the continuous and discontinuous thin films are named as “thin film” and “islands” respectively in this section. In the following, the study of MeOH adsorption and reaction is presented first on the SmO_x thin films and second on the SmO_x islands.

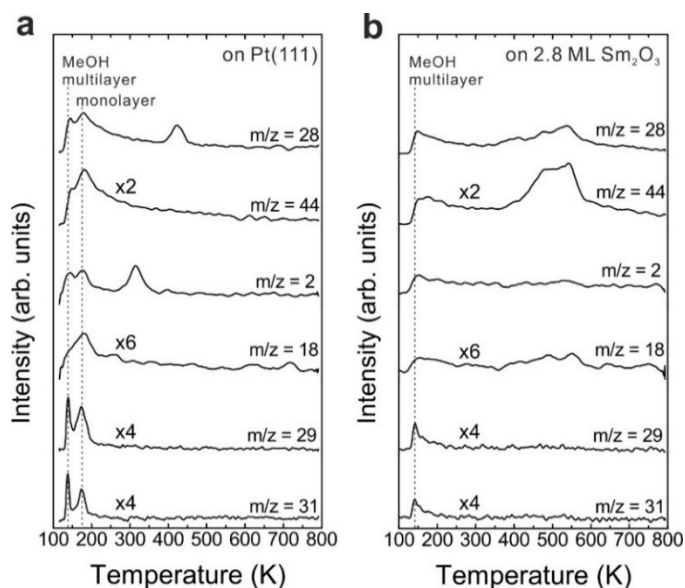


Figure 17. TPD spectra recorded from (a) a Pt(111) surface and (b) a 2.8 ML as-prepared continuous Sm_2O_3 thin film.

The MeOH TPD result obtained from an as-prepared continuous Sm_2O_3 thin film (2.8 ML) in **Figure 17 (b)** reveals that the MeOH reaction on the Sm_2O_3 thin film mainly forms CO and CO_2 as products. The result suggests that MeOH dehydrogenation is dominant on the SmO_x surface, and reveals that basic sites on the surface are in charge of the MeOH reaction. The features of MeOH TPD signals (CO and H_2) produced from Pt(111) shown in **Figure 17 (a)** vanish in the TPD spectra recorded from the as-prepared thin film, which indicates that the Sm_2O_3 thin film fully covers on Pt(111). By quantifying the MeOH TPD result for the Sm_2O_3 thin film, a considerable amount of hydrogen is absent in the balance, *i.e.* remaining on or in the sample, implying that hydrogen may form hydroxyl by reacting with SmO_x surface lattice oxygen or diffuse into the thin film. To learn how the Sm_2O_3 thin film responds to the MeOH reaction, repeated MeOH TPD experiments were conducted

on the sample shown in **Figure 18**. Obviously the result from the 2nd TPD shows clear changes compared to the 1st TPD. The intensity of CO₂ decreases whereas the intensity of CO increases, and a H₂-TPD signal arises at 540 K. The decrease of the CO₂ production yield indicates that available oxygen (OH species and surface lattice oxygen) is continuously eliminated via CO oxidation, which can be confirmed by monitoring the increasing trend of the CO production yield over repeated TPD runs. The appearance of the H₂ product in the 2nd TPD run suggests a saturated condition of the thin film towards hydrogen storage through OH formation and/or H diffusion. Overall, on the basis of the result of the repeated TPD experiments the MeOH reaction shows the capability of altering the chemical behavior and reactivity of the thin film.

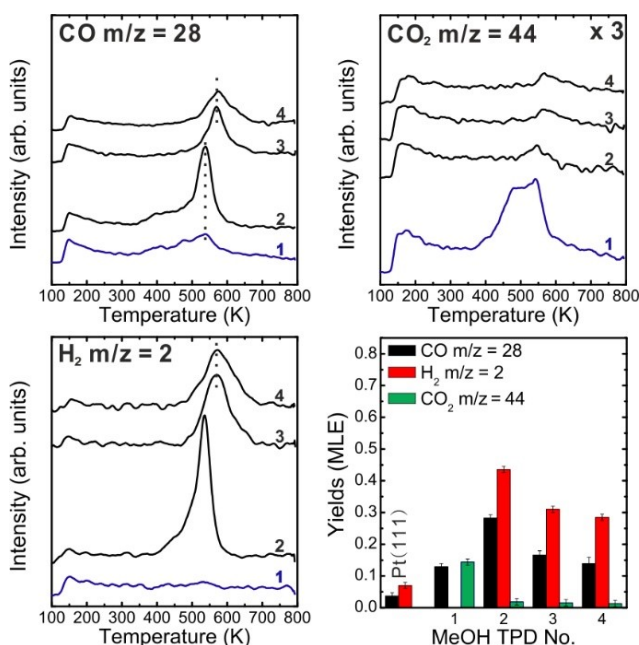


Figure 18. Repeated TPD series obtained from the 2.8 ML as-prepared Sm₂O₃ thin film and the estimated yields of CO, CO₂, and H₂ products.

In Chapter 2 It has been introduced that reduction and reoxidation treatments can alter SmO_x thin-film surface structure, also it has been found that the chemical property of SmO_x thin films can be modified by thermal reduction in CO- and D₂O-TPD studies. To further obtain insight into connections of oxidation conditions and structural/chemical properties of SmO_x thin films, the MeOH study was also performed on films treated by reduction/reoxidation. The MeOH TPD results (**Figure 19**) indeed reveal changes in chemical properties and reactivity of the SmO_x thin film due to

the treatments of reduction and reoxidation. CO_2 production is obviously suppressed on the reduced thin film due to lack of available oxygen on the surface, shown in **Figure 19 (a)**. Meanwhile the desorption signals of all products (CO , CO_2 , and H_2) shift to higher temperatures than those observed on the as-prepared thin film. Such observation is also seen on the SmO_x islands. In the following section TPD and IRRAS studies will be combined to give a whole picture of the MeOH reaction mechanism and the explanation for the shifting behavior will be given as well.

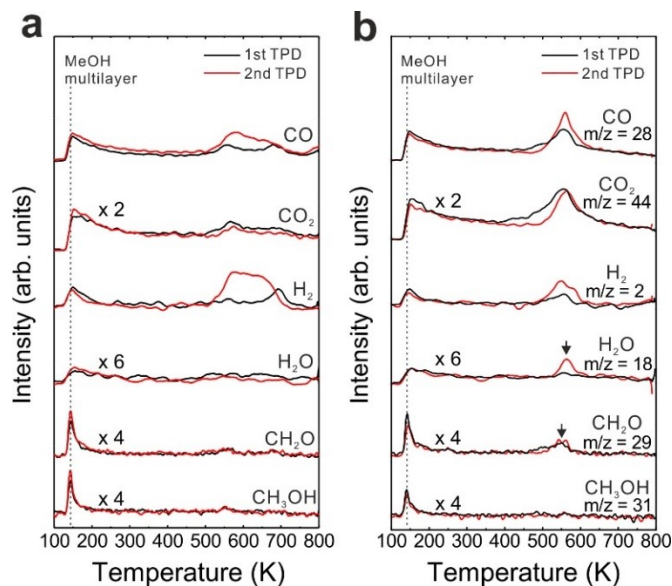


Figure 19. TPD spectra obtained from (a) the 2.8 ML reduced and (b) reoxidized SmO_x thin films.

The SmO_x thin film after the reoxidation treatment exhibits a distinct chemical behavior, *i.e.* formaldehyde (CH_2O) and water (H_2O) as new products are seen in the TPD spectra (**Figure 19 (b)**). Formation of CH_2O and H_2O indicates incomplete MeOH dehydrogenation on the reoxidized thin-film surface, suggesting that both weak acidic and basic sites exist on the reoxidized surface in order to restrict C-H bond breaking and avoid strong adsorption of CH_2O on the surface. Two possible explanations for this observation are: (1) special oxygen species such as superoxide (O_2^-) may be stored on the reoxidized surface. Such oxygen species existing on CeO_x surfaces have been reported [82-84]. The oxygen species acting as weaker basic sites than lattice oxygen may conduct incomplete MeOH dehydrogenation. (2) The reoxidation treatment improves the flatness of the thin film, and therefore reduces the numbers of surface vacancies/defects. Because surface vacancies/defects are essential for successful MeOH dehydrogenation, as a result, incomplete MeOH dehydrogenation may take place

on the reoxidized surface. According to the TPD result, the chemical property of the 2.8 ML reoxidized SmO_x thin film can be altered but not restored to its as-prepared condition by thermal reoxidation.

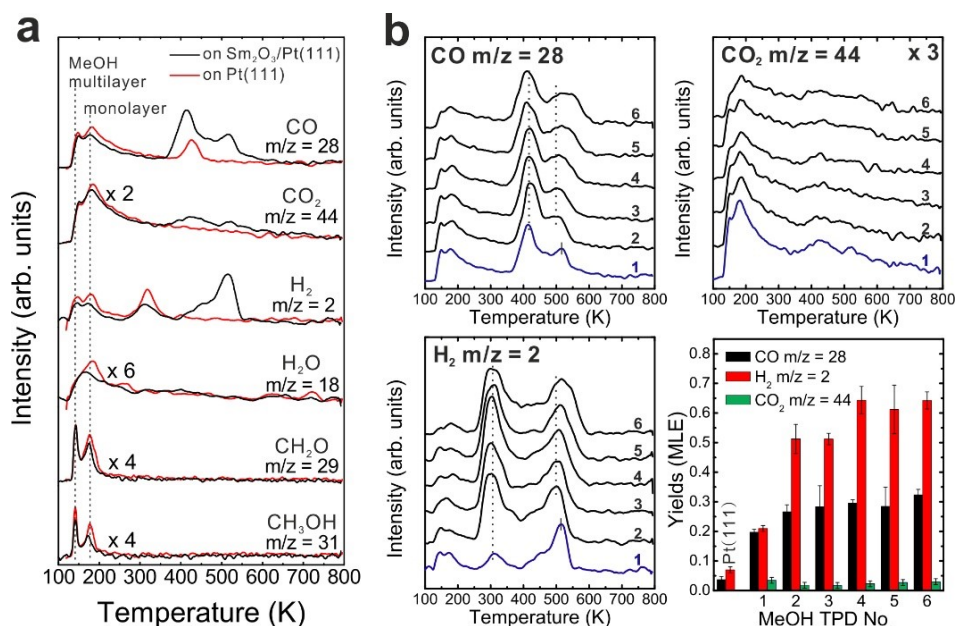


Figure 20. (a) The 1st TPD spectra obtained from Pt(111) and 0.9 ML as-prepared Sm_2O_3 islands. (b) Repeated TPD series obtained from the 0.9 ML Sm_2O_3 islands and the estimated yields of products.

Studies of MeOH adsorption and reaction were also conducted on as-prepared Sm_2O_3 islands (0.9 ML) and the TPD result is shown in **Figure 20**. As expected, the CO and H_2 desorption signals contributed by both the Pt(111) surface and the as-prepared Sm_2O_3 islands for MeOH decomposition arise in this case. Note that the MeOH monolayer desorption at 180 K mainly from exposed Pt areas is also observed here. Over repeated MeOH TPD experiments the Pt-related TPD signals remain at the original temperatures whereas the SmO_x -related signals shift to higher temperatures, indicating that only the SmO_x chemical behavior is altered by the MeOH reaction. The MeOH reaction also induces an increase of the sample reactivity according to the estimation of production yields.

IRRAS studies were performed to extend the understanding of MeOH adsorption and reaction on the SmO_x -Pt system. Here the existence of methoxy species (CH_3O^-) is clearly demonstrated by the detection of $\nu(\text{C-O})$, $\nu(\text{CH}_3)$, and $\rho(\text{CH}_3)$ features as shown in **Figure 21**. It should be noted that

methoxy species do not exist on both bare Pt(111) and O-terminated Pt(111) surfaces when the sample temperature above 150 K [85], therefore MeOH dehydrogenation to methoxy species on the SmO_x surface is confirmed. The $\nu(\text{C-O})$ peak emerges in the range of 1000 and 1100 cm^{-1} , and the $\nu_s(\text{CH}_3)$ and $\nu_{as}(\text{CH}_3)$ peaks appear at 2790 cm^{-1} and 2926 cm^{-1} respectively, also the $\rho(\text{CH}_3)$ peak is observed at 1140 cm^{-1} . The absence of a $\nu(\text{OH})$ signal at 3280 cm^{-1} indicates that the O-H bond of MeOH breaks during the dehydrogenation process. OH species may remain on the film surface as discussed above, however it should be noted that the IRRAS result does not provide information on surface OH species due to their small dynamic dipole moment and the varied adsorption geometry [86]. The broad signal of $\nu(\text{C-O})$ identified as two bands at 1080 cm^{-1} and 1042 cm^{-1} actually reveals that methoxy species stay at different adsorption sites on the Sm_2O_3 surface.

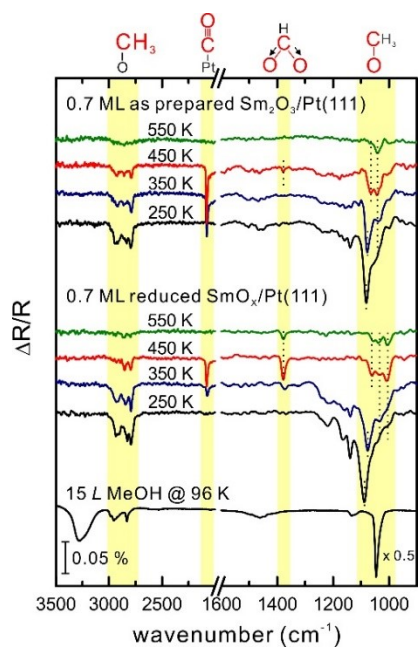


Figure 21. Temperature-dependent IRRAS spectra obtained from the 0.7 ML as-prepared and reduced SmO_x islands.

Further dehydrogenation of methoxy species to final products seen in TPD can be followed by monitoring the $\nu(\text{C-O})$ region. At elevated temperatures $\nu(\text{C}\equiv\text{O})$ and $\nu_s(\text{OCO})$ bands are also identified at 2080 cm^{-1} and 1378 cm^{-1} respectively in the IRRAS spectra. The $\nu(\text{C}\equiv\text{O})$ band originating from CO adsorbed on exposed Pt areas implies that a fraction of methoxy species dehydrogenates to H and CO, which subsequently spill over onto Pt and desorb as H_2 and CO at certain temperatures.

The spillover effect is obviously related to the significant increase of the production yields of Pt-related H₂ and CO products shown in the TPD results. The appearance of the $\nu_s(\text{OCO})$ band indicates that a part of methoxy species transforms into formate species on the Sm₂O₃ surface. The formate species may be an intermediate and eventually decompose as CO, CO₂, and H₂ products.

The IRRAS result from the reduced SmO_x islands is shown in **Figure 21** as well. There is an obvious difference in the $\nu(\text{C-O})$ region compared to the IRRAS spectra from the as-prepared Sm₂O₃ islands. A $\nu(\text{C-O})$ band appears at 1005 cm⁻¹ revealing that a new adsorption site is formed on the reduced SmO_x islands for methoxy species. Apart from the new $\nu(\text{C-O})$ band, other vibrational bands are still visible in the IRRAS spectra from the reduced surface. After heating the sample to 550 K, three $\nu(\text{C-O})$ bands and the $\nu_s(\text{OCO})$ band become small but still evident which is in contrast to absence of these bands on the as-prepared Sm₂O₃ surface. Based on this result, it can be speculated that there is a stronger bonding of methoxy and formate species on the reduced surface, perhaps because more surface defects/vacancies are formed and assist in stabilizing these species.

TPD results collected from the reduced SmO_x islands (**Figure 22**) certainly support this speculation, *i.e.* SmO_x-related peaks shifting to higher temperatures suggest that methoxy and also formate species bind to the reduced surface stronger, therefore decompose and desorb as products at higher desorption temperatures. It also explains the same trend which was mentioned above when the TPD studies from the 2.8 ML as-prepared and reduced continuous SmO_x thin films were compared. The TPD result (**Figure 22**) also reveals a wetting of the reduced SmO_x islands on Pt(111) based on disappearance of the Pt-related peaks in the 1st TPD experiment. Importantly, slight reoxidation of the SmO_x surface by MeOH is observed according to the average $[\text{H}_2]/\{[\text{CO}]+[\text{CO}_2]\}$ ratio which is significantly larger than two given by the estimation of production yields. This observation is also supported by monitoring the downshift of the SmO_x-related peaks towards lower temperatures and a film dewetting behavior on the basis of the regain of Pt-related peaks over the repeated TPD runs. The TPD result collected from the reoxidized Sm₂O₃ islands strongly suggests that the chemical behavior of the as-prepared surface is completely restored (**Figure 23**). The reoxidation procedure is therefore more efficient for the SmO_x islands than the continuous SmO_x thin film.

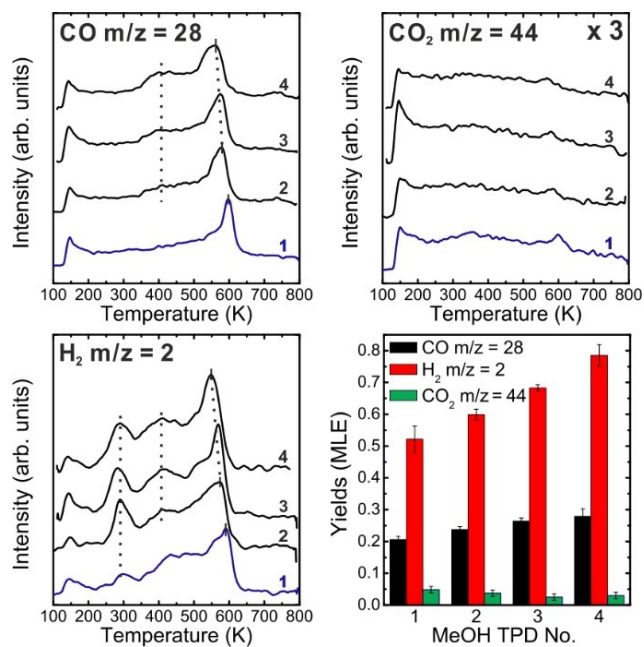


Figure 22. Repeated TPD series obtained from the 0.9 ML reduced SmO_x islands and the estimated yields of products.

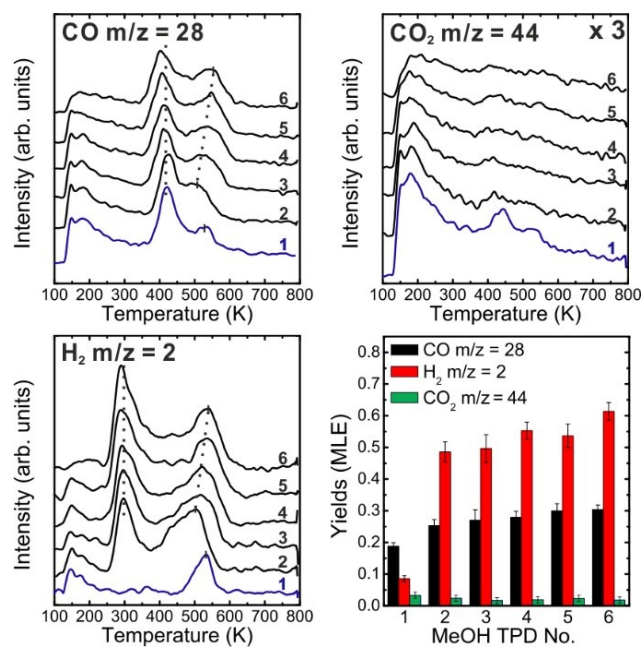


Figure 23. Repeated TPD series obtained from the 0.9 ML reoxidized Sm_2O_3 islands and the estimated yields of products.

Yield of MeOH reaction (MLE)	Pt(111)	0.9 ML samaria thin films			2.8 ML samaria thin films		
		as prep. Sm ₂ O ₃	red. SmO _x	reox. Sm ₂ O ₃	as prep. Sm ₂ O ₃	red. SmO _x	reox. Sm ₂ O ₃
1 st TPD	0.04	0.24	0.26	0.22	0.27	0.12	0.14
Ave. w/o 1 st TPD	--	0.31	0.35*	0.30	0.21	0.17	0.14
Ratio of [H₂]/{[CO]+[CO₂]}							
1 st TPD	1.80	0.89	2.00	0.40	--	0.57	0.22
Ave. w/o 1 st TPD	--	1.87	2.38	1.80	1.61	1.59	1.35

Table 2. Summary of overall reactivity for the MeOH reaction on the Pt(111), the 0.9 ML SmO_x islands, and the 2.8 ML SmO_x thin films. Yields of the MeOH reaction are defined by [CH₃OH] = [CO] + [CO₂] except from the 0.9 ML reduced islands (marked *). 0.35 MLE is calculated by [CH₃OH] = 2[H₂] because a fraction of C and O remains on/in the sample, which is based on the estimated ratio of [H₂]/{[CO]+[CO₂]}.

A comparison of overall reactivity towards the MeOH reaction on Pt(111), the continuous SmO_x thin film, and the discontinuous SmO_x thin film (islands) is provided in **Table 2** on the basis of estimating how many monolayer equivalent (MLE)⁵ MeOH molecules react on these surfaces. It denotes that the SmO_x islands show the highest reactivity, which suggests that a cooperative effect between SmO_x islands and exposed Pt surfaces must play an important role for promoting the MeOH reaction. The cooperative effect actually takes place on the perimeter sites where CO and H produced from MeOH dehydrogenation on the SmO_x surface spill over to free Pt areas at relatively low temperature (ca. 250 K), and a part of adsorption sites on the SmO_x surface can be vacated. Therefore, residual MeOH molecules still exist on the surface and they may refill these vacant adsorption sites. As a result, in total more MeOH molecules can react on the SmO_x islands than on the continuous thin film and the Pt(111) surface.

3.3.2 SmO_x structural changes induced by MeOH

The long-range structural changes of SmO_x induced by reduction/oxidation treatments have been described in Chapter 2. In the MeOH study, it is found that MeOH exhibits the capability of reducing or oxidizing SmO_x depending on the initial SmO_x oxidation conditions. Moreover, the MeOH-induced reduction/reoxidation procedures also lead to long-range structural changes of SmO_x thin

⁵ One monolayer equivalent (MLE) is defined as the Pt(111) surface atomic density, *i.e.* 1.52 x 10¹⁵ cm⁻².

films/islands. The structural changes were studied by LEED and the results are summarized in **Table 3**. Respective LEED images and details are shown in the attached paper III. In the LEED study, apart from the quasi-3 x 3 and satellite structures, several new structures, such as rotated, 2 x 2, and $(2\sqrt{3} \times 2\sqrt{3})R30^\circ$ structures in registry with $\text{SmO}_x(111)$ are observed as well.

LEED patterns of 0.9 ML SmO_x on Pt(111)				Schematic representation of LEED patterns
MeOH TPD treatment	as-prepared Sm_2O_3	reduced SmO_x	reoxidized Sm_2O_3	
w/o	quasi-3 x 3	satellites	quasi-3 x 3 + 2 add. spots	
with	slightly rotated	rotated	quasi-3 x 3 + 2 add. spots + $(2\sqrt{3} \times 2\sqrt{3})R30^\circ$	
LEED patterns of 2.8 ML SmO_x on Pt(111)				
MeOH TPD treatment	as-prepared Sm_2O_3	reduced SmO_x	reoxidized Sm_2O_3	
w/o	quasi-3 x 3	quasi-3 x 3 + $(2\sqrt{3} \times 2\sqrt{3})R30^\circ$	quasi-3 x 3 + 2 x 2	
with	$\text{SmO}_x(1 \times 1)$	quasi-3 x 3 + $(2\sqrt{3} \times 2\sqrt{3})R30^\circ$	quasi-3 x 3 + $(2\sqrt{3} \times 2\sqrt{3})R30^\circ$	

Table 3. Summary of LEED patterns obtained from the 0.9 ML SmO_x islands and the 2.8 ML SmO_x thin films before and after MeOH-TPD experiments.

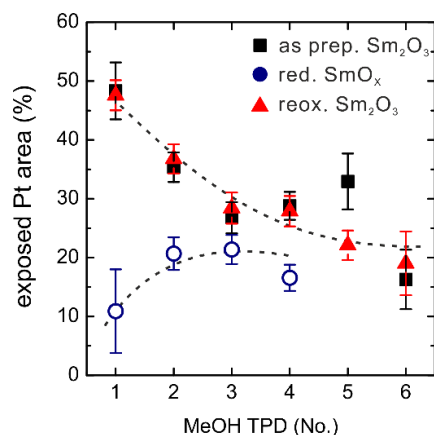


Figure 24. Variations of exposed Pt areas (%) on the 0.9 ML SmO_x islands over repeated MeOH-TPD experiments. (Dashed lines as a guide to the eye)

Particularly a significant material transport is involved in the structural changes of the discontinuous SmO_x thin films (islands) related to the film's wetting/dewetting behavior, which can be demonstrated by the TPD results. Because the MeOH monolayer-desorption signal (at 180 K) is primarily contributed by Pt(111), the desorption yield from this signal therefore provides revelation about the area of exposed Pt surface. The changes of exposed Pt areas are monitored over repeated

TPD runs, as shown in **Figure 24**. About half of the Pt(111) surface was covered by the as-prepared Sm_2O_3 islands before the MeOH TPD experiments. The exposed Pt areas continuously decrease from $\sim 50\%$ to $\sim 20\%$ during the repeated TPD experiments, revealing that the film's wetting behavior is due to the MeOH-induced reduction. The changes of exposed Pt areas estimated from the reoxidized islands follow the same trend as from the as-prepared one, which again suggests a successful restoration of the film condition by reoxidation. In contrast, the exposed Pt areas estimated from the reduced islands continuously increase from $\sim 10\%$ to $\sim 20\%$ during the repeated TPD runs, indicating that the film's dewetting is due to the MeOH-induced reoxidation. Note that the oxidized (as-prepared and reoxidized) Sm_2O_3 and the reduced SmO_x islands reach a similar status with $\sim 20\%$ of Pt surface exposed after repeated TPD experiments. This observation implies the existence of an equilibrium condition of the film structure, *i.e.* the condition which is independent on the initial film status can be achieved by the MeOH reaction.

3.4 Summary of the surface chemistry studies

The chemical reactivity and properties of both continuous SmO_x thin films and SmO_x islands have been investigated by conducting CO, D_2O , and MeOH adsorption-reaction experiments. CO only weakly adsorbs on Sm_2O_3 surfaces, whereas CO can stay on the Pt surface above room temperature. Importantly, the system constituted by both Sm_2O_3 islands and exposed Pt areas exhibits a new property for CO oxidation. The result therefore reveals the importance of the perimeter sites. Water (D_2O) can dissociate on SmO_x surfaces and form stable OD species on these surfaces above room temperature. D_2O dissociation is even promoted and OD species are stabilized on thermal reduced SmO_x surfaces presumably due to SmO_x surface vacancy formation. An intriguing result is observed on the reduced SmO_x islands, *i.e.* a pronounced amount of D_2 is produced with CO participation. Moreover, the perimeter sites show importance for improving the chemical reactivity of the SmO_x -Pt system. On the basis of the TPD results, the identified mechanisms of D_2O dissociation and D_2 formation are summarized in **Figure 25**.

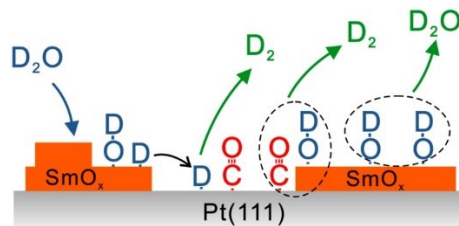


Figure 25. Summary of D_2O dissociation-reaction and the CO-OD interaction on SmO_x islands.

MeOH is dehydrogenated on SmO_x surfaces and forms CO and H_2 as main desorbing products. CO_2 in small quantities is also obtained via full oxidation of MeOH by available oxygen from the Sm_2O_3 surface. The TPD results indicate that a fraction of hydrogen is stored either as surface OH species on SmO_x or in the film. MeOH dehydrogenation is further confirmed in IRRAS spectra by detecting the methoxy and formate species. The SmO_x islands exhibit the highest reactivity compared to the SmO_x thin films and the Pt(111) surface. The fact can be explained by a spillover effect, *i.e.* products are able to spillover from SmO_x islands to Pt at relatively low temperature (ca. 250 K) which is not available on the continuous SmO_x thin films. The identified mechanisms of the MeOH reaction are summarized in **Figure 26**. The reactivity for the MeOH reaction is also affected by SmO_x structures and oxidation conditions, and *vice versa*, MeOH-induced reduction/oxidation can alter the SmO_x structures leading to a film's wetting/dewetting behavior.

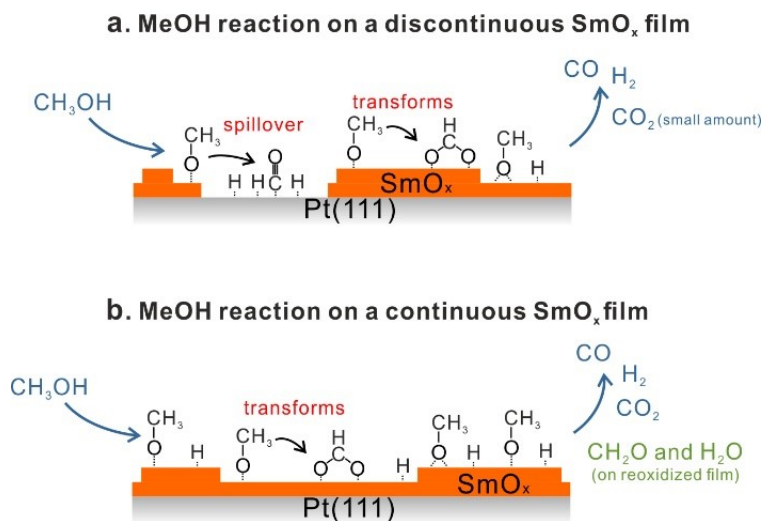


Figure 26. Summary of the MeOH dehydrogenation and reaction on (a) a discontinuous SmO_x thin film (islands) and (b) a continuous SmO_x thin film.

CHAPTER 4

CONCLUSION AND OUTLOOK

To respond to the urgent demands regarding the scarcity of systematic studies for a SmO_x model system, high-quality Sm_2O_3 thin films grown on Pt(111) were well characterized by STM and LEED. The thin films grow as a defective fluorite structure instead of a bixbyite structure usually seen in bulk sesquioxides. Sm atoms in the lattice of thin films exhibit a small degree of flexibility, *i.e.* they can arrange into either a well-ordered hexagonal (1.37 x 1.37) or a (1.33 x 1.33) sublattice in registry of Pt(111), resulting in a quasi- 3×3 or a perfect- 3×3 LEED pattern. Although bulk Sm_2O_3 is not generally considered as a reducible oxide, partial reduction of Sm_2O_3 thin films is obtained by annealing the thin films in UHV at 1000 K. Rocksalt SmO(100) is found at the interface between Sm_2O_3 and Pt(111) at low SmO_x coverages between ~ 1 and 2 ML after the thermal reduction process, meanwhile, SmO_x islands spreading onto Pt(111) leads to a significant film-wetting behavior. Alternatively, the SmO(100) phases can also be obtained via the $\text{Sm}_2\text{O}_3 + \text{Sm}$ reaction at 800 K. Such reduced SmO_x thin films can be reoxidized successfully, *i.e.* the $\text{Sm}_2\text{O}_3(111)$ lattice structure is restored and additionally the film flatness and connectivity of Sm_2O_3 domains are improved.

CO, D_2O , and MeOH adsorption-reaction studies were conducted on the SmO_x model system in order to gain the fundamental understanding of the relationships between the surface properties and chemical reactivity of the SmO_x thin films. To further study the influence of the oxide-metal interaction at the boundary/perimeter sites towards thin-film reactivity, both continuous SmO_x thin films and discontinuous thin films (SmO_x islands with exposed Pt areas) were prepared. CO oxidation only takes place at the perimeter sites in which Sm_2O_3 provides available lattice oxygen to oxidize CO adsorbing on Pt. D_2O dissociates and produces stable OD species on both the Sm_2O_3 thin film and Sm_2O_3 islands. Thermal reduction promotes not only D_2O dissociation but also the stabilization of OD species on these surfaces presumably because of SmO_x surface vacancy formation. A CO-OD interaction releasing a pronounced D_2 production is also observed on the perimeter sites in which CO adsorbing on the Pt areas is able to react with OD species locating on reduced SmO_x islands. SmO_x

as a basic oxide is verified by the MeOH adsorption-reaction studies based on the CO, CO₂ and H₂ production. Again, the existence of the perimeter sites plays an important role for improving the SmO_x reactivity towards the MeOH reaction, *i.e.* products of the MeOH reaction on SmO_x islands can spillover to exposed Pt surfaces resulting in vacating SmO_x adsorption sites for additional MeOH molecules. The SmO_x reactivity is also influenced by its structures and oxidation conditions, and *vice versa*, MeOH-induced reduction/oxidation fairly shows capability of directing SmO_x structural changes.

This research could bring the value of studying SmO_x model systems to light with respect to both structural and chemical interests. However, there are open questions remaining behind the studies which may encourage further fundamental and applied studies. For instance, only SmO_x thin films at coverages below 5 ML (ca. thickness 2 nm) have been studied, and such thin films grow as the defective fluorite structure. If the film thickness is increased to tens of nanometers, would the defective fluorite structure still exist or transform to a bixbyite structure? Discontinuous SmO_x thin films (islands) fairly named as “inverse SmO_x model catalysts” show potentials for hydrogen production and CO oxidation under UHV experimental conditions. However, real world catalysts normally operate at pressures in excess of atmospheric pressure instead of UHV conditions. Additionally such real catalysts are typically polycrystalline instead of single crystalline materials, thus doubt can emerge if a single-crystal model catalyst could be comparable to its real catalyst counterpart regarding chemical properties. These differences between surface science and real catalytic studies are the so-called “pressure gap” and “material gap” [87]. Therefore the question is if such model catalysts could overcome the “pressure gap” or the “material gap” and show the same abilities towards the real world catalysis. This comprehensive study for the MeOH reaction may recommend more chemical studies particularly of other chemical compounds containing similar functional groups such as alcohols and hydrocarbons. To study these compounds will be also important for exploring catalytic properties of SmO_x-based catalysts. In particular, studies of hydrocarbons on this SmO_x model system will contribute to a fundamental understanding of the interactions between hydrocarbons and SmO_x surfaces, which will be beneficial to developing high-selectivity catalysts for the OCM reaction. Overall, this work demonstrates the significance of studying SmO_x and to look into other rare-earth sesquioxides will be indispensable.

REFERENCE

- [1] G.B. Haxel, J.B. Hedrick, G.J. Orris, P.H. Stauffer, J.W. Hendley II, Rare earth elements: critical resources for high technology, in: Fact Sheet, 2002.
- [2] S. Bernal, G. Blanco, J.M. Gatica, J.A. Pérez-Omil, J.M. Pintado, H. Vidal, Chemical Reactivity of Binary Rare Earth Oxides, in: G. Adachi, N. Imanaka, Z.C. Kang (Eds.) Binary Rare Earth Oxides, Springer Netherlands, 2005, pp. 9-55.
- [3] J.M. Leger, N. Yacoubi, J. Loriers, Synthesis of rare earth monoxides, Journal of Solid State Chemistry, 36 (1981) 261-270.
- [4] G. Adachi, N. Imanaka, The binary rare earth oxides, Chemical Reviews, 98 (1998) 1479-1514.
- [5] G.V. Antoshin, K.M. Minachev, R.V. Dmitriev, Mobility of oxygen and catalytic properties of rare earth oxides with respect to oxidation of hydrogen, Russian Chemical Bulletin, 16 (1967) 1793-1795.
- [6] J.E. Shelby, J.T. Kohli, Rare-Earth Aluminosilicate Glasses, Journal of the American Ceramic Society, 73 (1990) 39-42.
- [7] F. Auzel, P. Goldner, Towards rare-earth clustering control in doped glasses, Optical Materials, 16 (2001) 93-103.
- [8] R. L. W, The Use of Rare Earths in Glass Compositions, in: Industrial Applications of Rare Earth Elements, America Chemical Society, 1981, pp. 81-94.
- [9] J.P. Cuif, E. Rohart, P. Macaudiere, C. Bauregard, E. Suda, B. Pacaud, N. Imanaka, T. Masui, S. Tamura, Applications, in: G. Adachi, N. Imanaka, Z.C. Kang (Eds.) Binary Rare Earth Oxides, Springer Netherlands, 2005, pp. 215-255.
- [10] H. Robert V, Rare Earth Polishing Compounds, in: Industrial Applications of Rare Earth Elements, America Chemical Society, 1981, pp. 95-100.
- [11] J.R. McColl, P. Frank C, Use of Rare Earths in Television and Cathode Ray Phosphors, in: Industrial Applications of Rare Earth Elements, America Chemical Society, 1981, pp. 177-193.
- [12] K. Huang, J.B. Goodenough, A solid oxide fuel cell based on Sr- and Mg-doped LaGaO_3 electrolyte: the role of a rare-earth oxide buffer, Journal of Alloys and Compounds, 303-304 (2000) 454-464.
- [13] G.B. Balazs, R.S. Glass, ac impedance studies of rare earth oxide doped ceria, Solid State Ionics, 76 (1995) 155-162.
- [14] H. Yahiro, Y. Eguchi, K. Eguchi, H. Arai, Oxygen ion conductivity of the ceria-samarium oxide system with fluorite structure, Journal of Applied Electrochemistry, 18 (1988) 527-531.
- [15] W. David N, The Use of Rare Earth Elements in Zeolite Cracking Catalysts, in: Industrial Applications of Rare Earth Elements, America Chemical Society, 1981, pp. 101-116.
- [16] P. Alan W, K.I.M. Gwan, Rare Earths in Noncracking Catalysts, in: Industrial Applications of Rare Earth Elements, America Chemical Society, 1981, pp. 117-131.

- [17] G.A.M. Hussein, Rare earth metal oxides: Formation, characterization and catalytic activity-thermoanalytical and applied pyrolysis review, *Journal of Analytical and Applied Pyrolysis*, 37 (1996) 111-149.
- [18] M.P. Rosynek, Catalytic Properties of Rare Earth Oxides, *Catalysis Reviews*, 16 (1977) 111-154.
- [19] K.N. Yang, Y. Dalichaouch, J.M. Ferreira, B.W. Lee, J.J. Neumeier, M.S. Torikachvili, H. Zhou, M.B. Maple, R.R. Hake, High temperature superconductivity in rare-earth (R)-barium copper oxides (RBa₂)Cu₃O_{9- δ} , *Solid State Communications*, 63 (1987) 515-519.
- [20] J.M. Tarascon, W.R. McKinnon, L.H. Greene, G.W. Hull, Vogel, M. E, Oxygen and rare-earth doping of the 90-K superconducting perovskite YBa₂Cu₃O₇, *Physical Review B*, 36 (1987) 226-234.
- [21] W.C. Chin, K.Y. Cheong, Z. Hassan, Sm₂O₃ gate dielectric on Si substrate, *Materials Science in Semiconductor Processing*, 13 (2010) 303-314.
- [22] M. Leskelä, M. Ritala, Rare-earth oxide thin films as gate oxides in MOSFET transistors, *Journal of Solid State Chemistry*, 171 (2003) 170-174.
- [23] S. Ohmi, S. Akama, A. Kikuchi, I. Kashiwagi, C. Ohshima, J. Taguchi, H. Yamamoto, K. Sato, M. Takeda, H. Ishiwara, Rare earth metal oxides for high-K gate insulator, in: *Semiconductor silicon 2002: proceedings of the Ninth International Symposium on Silicon Materials Science and Technology*, Electrochemical Society, 2002, pp. 376.
- [24] T.G. Goonan, Rare earth elements—End use and recyclability: U.S. Geological Survey Scientific Investigations, Report 2011–5094, available only at <http://pubs.usgs.gov/sir/2011/5094/>, 2011.
- [25] Y. Yoshimura, N. Kijima, T. Hayakawa, K. Murata, K. Suzuki, F. Mizukami, K. Matano, T. Konishi, T. Oikawa, M. Saito, T. Shiojima, K. Shiozawa, K. Wakui, G. Sawada, K. Sato, S. Matsuo, N. Yamaoka, Catalytic Cracking of Naphtha to Light Olefins, *Catalysis Surveys from Asia*, 4 (2001) 157-167.
- [26] J.A. Sullivan, O. Keane, P. Dulgheru, N. O'Callaghan, Environmental Applications of Multifunctional Nanocomposite Catalytic Materials: Issues with Catalyst Combinations, in: *Advanced Catalytic Materials*, John Wiley & Sons, Inc., 2015, pp. 1-36.
- [27] J.A. Rodriguez, S. Ma, P. Liu, J. Hrbek, J. Evans, M. Pérez, Activity of CeO_x and TiO_x Nanoparticles Grown on Au(111) in the Water-Gas Shift Reaction, *Science*, 318 (2007) 1757-1760.
- [28] R.J. Gorte, S. Zhao, Studies of the water-gas-shift reaction with ceria-supported precious metals, *Catalysis Today*, 104 (2005) 18-24.
- [29] C. Ratnasamy, J.P. Wagner, Water Gas Shift Catalysis, *Catalysis Reviews*, 51 (2009) 325-440.
- [30] M. Machida, Y. Murata, K. Kishikawa, D. Zhang, K. Ikeue, On the Reasons for High Activity of CeO₂ Catalyst for Soot Oxidation, *Chemistry of Materials*, 20 (2008) 4489-4494.
- [31] K. Krishna, A. Bueno-López, M. Makkee, J. Moulijn, Potential rare-earth modified CeO₂ catalysts for soot oxidation part II: Characterisation and catalytic activity with NO+O₂, *Applied Catalysis B: Environmental*, 75 (2007) 201-209.

- [32] E. Aneggi, M. Boaro, C.d. Leitenburg, G. Dolcetti, A. Trovarelli, Insights into the redox properties of ceria-based oxides and their implications in catalysis, *Journal of Alloys and Compounds*, 408–412 (2006) 1096-1102.
- [33] A.G. Dedov, A.S. Loktev, Moiseev, II, A. Aboukais, J.F. Lamonier, I.N. Filimonov, Oxidative coupling of methane catalyzed unexpected synergistic effect of the by rare earth oxides oxide mixtures, *Applied Catalysis A: General*, 245 (2003) 209-220.
- [34] T.W. Elkins, B. Neumann, M. Bäumer, H.E. Hagelin-Weaver, Effects of Li Doping on MgO-Supported Sm_2O_3 and TbO_x Catalysts in the Oxidative Coupling of Methane, *ACS Catalysis*, 4 (2014) 1972-1990.
- [35] K.D. Campbell, H. Zhang, J.H. Lunsford, Methane activation by the lanthanide oxides, *The Journal of Physical Chemistry*, 92 (1988) 750-753.
- [36] B. Neumann, T. Elkins, A. Gash, H. Hagelin-Weaver, M. Bäumer, Sol–Gel Preparation of Samaria Catalysts for the Oxidative Coupling of Methane, *Catalysis Letters*, 145 (2015) 1251-1261.
- [37] G.A.M. Hussein, Samarium oxide catalyst; formation, characterization and activity towards propan-2-ol decomposition. An IR spectroscopic study, *Journal of the Chemical Society, Faraday Transactions*, 90 (1994) 3693-3697.
- [38] C.R. Henry, Surface studies of supported model catalysts, *Surface Science Reports*, 31 (1998) 231-325.
- [39] P.L.J. Gunter, J.W. Niemantsverdriet, F.H. Ribeiro, G.A. Somorjai, Surface Science Approach to Modeling Supported Catalysts, *Catalysis Reviews*, 39 (1997) 77-168.
- [40] D.R. Mullins, The surface chemistry of cerium oxide, *Surface Science Reports*, 70 (2015) 42-85.
- [41] A. Trovarelli, P. Fornasiero, *Catalysis by ceria and related materials*, Imperial College Press London, 2002.
- [42] M.H. Zoellner, J. Dabrowski, P. Zaumseil, A. Giussani, M.A. Schubert, G. Lupina, H. Wilkens, J. Wollschläger, M. Reichling, M. Bäumer, T. Schroeder, Stacking behavior of twin-free type-B oriented $\text{CeO}_2(111)$ films on hexagonal $\text{Pr}_2\text{O}_3(0001)/\text{Si}(111)$ systems, *Physical Review B*, 85 (2012) 035302.
- [43] J.P. Liu, P. Zaumseil, E. Bugiel, H.J. Osten, Epitaxial growth of Pr_2O_3 on $\text{Si}(111)$ and the observation of a hexagonal to cubic phase transition during postgrowth N_2 annealing, *Applied Physics Letters*, 79 (2001) 671-673.
- [44] A. Schaefer, S. Gevers, V. Zielasek, T. Schroeder, J. Falta, J. Wollschläger, M. Bäumer, Photoemission study of praseodymia in its highest oxidation state: The necessity of in situ plasma treatment, *The Journal of Chemical Physics*, 134 (2011) 054701.
- [45] H. Wilkens, S. Gevers, S. Röhe, A. Schaefer, M. Bäumer, M.H. Zoellner, T. Schroeder, J. Wollschläger, Structural Changes of Ultrathin $\text{Cub-PrO}_2(111)/\text{Si}(111)$ Films Due to Thermally Induced Oxygen Desorption, *The Journal of Physical Chemistry C*, 118 (2014) 3056-3061.

- [46] S. Gevers, T. Weisemoeller, D. Bruns, A. Giussani, T. Schroeder, J. Wollschläger, Post-deposition annealing of praseodymia films on Si(111) at low temperatures, *Journal of Physics: Condensed Matter*, 23 (2011) 115904.
- [47] M.H. Zoellner, G. Niu, J.-H. Jhang, A. Schaefer, P. Zaumseil, M. Bäumer, T. Schroeder, Temperature-Dependent Reduction of Epitaxial $Ce_{1-x}Pr_xO_{2-\delta}$ ($x = 0 - 1$) Thin Films on Si(111): A Combined Temperature-Programmed Desorption, X-ray Diffraction, X-ray Photoelectron Spectroscopy, and Raman Study, *The Journal of Physical Chemistry C*, 117 (2013) 24851-24857.
- [48] G. Niu, M.H. Zoellner, T. Schroeder, A. Schaefer, J.-H. Jhang, V. Zielasek, M. Baumer, H. Wilkens, J. Wollschlager, R. Olbrich, C. Lammers, M. Reichling, Controlling the physics and chemistry of binary and ternary praseodymium and cerium oxide systems, *Physical Chemistry Chemical Physics*, (2015).
- [49] J. Höcker, W. Cartas, A. Schaefer, M. Bäumer, J.F. Weaver, J. Falta, J.I. Flege, Growth, Structure, and Stability of the High-Index $TbO_x(112)$ Surface on Cu(111), *The Journal of Physical Chemistry C*, 119 (2015) 14175-14184.
- [50] W. Cartas, R. Rai, A. Sathe, A. Schaefer, J.F. Weaver, Oxidation of a $Tb_2O_3(111)$ Thin Film on Pt(111) by Gas-Phase Oxygen Atoms, *The Journal of Physical Chemistry C*, 118 (2014) 20916-20926.
- [51] E.E. Wolf, *Methane conversion by oxidative processes: fundamental and engineering aspects*, Van Nostrand Reinhold, 1992.
- [52] T. Kuriyama, K. Kunimori, H. Nozoye, Adsorption of carbon monoxide on a SmO_x film, *Chemical Communications*, (1998) 501-502.
- [53] T. Kuriyama, K. Kunimori, H. Nozoye, Interaction of CO with the $SmO_x/Ru(001)$ interface, *Surface Science*, 402-404 (1998) 178-181.
- [54] Z.Q. Jiang, W.P. Zhou, D.L. Tan, R.S. Zhai, X.H. Bao, Evidence for perimeter sites over SmO_x -modified Rh(100) surface by CO chemisorption, *Surface Science*, 565 (2004) 269-278.
- [55] P.M. Albrecht, D.R. Mullins, Adsorption and Reaction of Methanol over $CeO_x(100)$ Thin Films, *Langmuir*, 29 (2013) 4559-4567.
- [56] V. Matolin, J. Libra, M. Skoda, N. Tsud, K.C. Prince, T. Skala, Methanol adsorption on a $CeO_2(111)/Cu(111)$ thin film model catalyst, *Surface Science*, 603 (2009) 1087-1092.
- [57] D.R. Mullins, M.D. Robbins, J. Zhou, Adsorption and reaction of methanol on thin-film cerium oxide, *Surface Science*, 600 (2006) 1547-1558.
- [58] J. Zhou, D.R. Mullins, Rh-Promoted Methanol Decomposition on Cerium Oxide Thin Films, *The Journal of Physical Chemistry B*, 110 (2006) 15994-16002.
- [59] R.M. Ferrizz, G.S. Wong, T. Egami, J.M. Vohs, Structure Sensitivity of the Reaction of Methanol on Ceria, *Langmuir*, 17 (2001) 2464-2470.
- [60] Q. Guo, Y. Zhao, C. Jiang, W.L. Mao, Z. Wang, Phase transformation in Sm_2O_3 at high pressure: In situ synchrotron X-ray diffraction study and ab initio DFT calculation, *Solid State Communications*, 145 (2008) 250-254.

- [61] M.A. VanHove, W.H. Weinberg, C.-M. Chan, Low-energy electron diffraction: experiment, theory and surface structure determination, Springer Science & Business Media, 2012.
- [62] C. Suzuki, J. Kawai, M. Takahashi, A.-M. Vlaicu, H. Adachi, T. Mukoyama, The electronic structure of rare-earth oxides in the creation of the core hole, *Chemical Physics*, 253 (2000) 27-40.
- [63] D.R. Mullins, S.H. Overbury, D.R. Huntley, Electron spectroscopy of single crystal and polycrystalline cerium oxide surfaces, *Surface Science*, 409 (1998) 307-319.
- [64] Z. Zhang, J.T. Yates, Band Bending in Semiconductors: Chemical and Physical Consequences at Surfaces and Interfaces, *Chemical Reviews*, 112 (2012) 5520-5551.
- [65] V. Stetsovych, F. Pagliuca, F. Dvořák, T. Duchoň, M. Vorokhta, M. Aulická, J. Lachnitt, S. Schernich, I. Matolínová, K. Veltruská, T. Skála, D. Mazur, J. Mysliveček, J. Libuda, V. Matolín, Epitaxial Cubic Ce₂O₃ Films via Ce–CeO₂ Interfacial Reaction, *The Journal of Physical Chemistry Letters*, 4 (2013) 866-871.
- [66] J.A. Rodríguez, J. Hrbek, Inverse oxide/metal catalysts: A versatile approach for activity tests and mechanistic studies, *Surface Science*, 604 (2010) 241-244.
- [67] J. Graciani, J.F. Sanz, Designing a new generation of catalysts: Water gas shift reaction example, *Catalysis Today*, 240, Part B (2015) 214-219.
- [68] A. Hornés, A.B. Hungría, P. Bera, A.L. Cámara, M. Fernández-García, A. Martínez-Arias, L. Barrio, M. Estrella, G. Zhou, J.J. Fonseca, J.C. Hanson, J.A. Rodríguez, Inverse CeO₂/CuO Catalyst As an Alternative to Classical Direct Configurations for Preferential Oxidation of CO in Hydrogen-Rich Stream, *Journal of the American Chemical Society*, 132 (2010) 34-35.
- [69] P.A. Redhead, Thermal desorption of gases, *Vacuum*, 12 (1962) 203-211.
- [70] C. Rhodes, G.J. Hutchings, A.M. Ward, Water-gas shift reaction: finding the mechanistic boundary, *Catalysis Today*, 23 (1995) 43-58.
- [71] J. Nakamura, J.M. Campbell, C.T. Campbell, Kinetics and mechanism of the water-gas shift reaction catalysed by the clean and Cs-promoted Cu(110) surface: a comparison with Cu(111), *Journal of the Chemical Society, Faraday Transactions*, 86 (1990) 2725-2734.
- [72] A.B. Mhadeshwar, D.G. Vlachos, Microkinetic Modeling for Water-Promoted CO Oxidation, Water–Gas Shift, and Preferential Oxidation of CO on Pt, *The Journal of Physical Chemistry B*, 108 (2004) 15246-15258.
- [73] A.A. Gokhale, J.A. Dumesic, M. Mavrikakis, On the Mechanism of Low-Temperature Water Gas Shift Reaction on Copper, *Journal of the American Chemical Society*, 130 (2008) 1402-1414.
- [74] C.V. Ovesen, P. Stoltze, J.K. Nørskov, C.T. Campbell, A kinetic model of the water gas shift reaction, *Journal of Catalysis*, 134 (1992) 445-468.
- [75] F.T. Wagner, T.E. Moylan, A comparison between water adsorbed on Rh(111) and Pt(111), with and without predosed oxygen, *Surface Science*, 191 (1987) 121-146.

- [76] D. Marrocchelli, B. Yildiz, First-Principles Assessment of H₂S and H₂O Reaction Mechanisms and the Subsequent Hydrogen Absorption on the CeO₂(111) Surface, *The Journal of Physical Chemistry C*, 116 (2011) 2411-2424.
- [77] C.-S. Chen, W.-H. Cheng, S.-S. Lin, Study of reverse water gas shift reaction by TPD, TPR and CO₂ hydrogenation over potassium-promoted Cu/SiO₂ catalyst, *Applied Catalysis A: General*, 238 (2003) 55-67.
- [78] W. Wang, S. Wang, X. Ma, J. Gong, Recent advances in catalytic hydrogenation of carbon dioxide, *Chemical Society Reviews*, 40 (2011) 3703-3727.
- [79] I.A. Fisher, A.T. Bell, A Mechanistic Study of Methanol Decomposition over Cu/SiO₂, ZrO₂/SiO₂, and Cu/ZrO₂/SiO₂, *Journal of Catalysis*, 184 (1999) 357-376.
- [80] M. Badlani, I. Wachs, Methanol: A “Smart” Chemical Probe Molecule, *Catalysis Letters*, 75 (2001) 137-149.
- [81] J.M. Tatibouët, Methanol oxidation as a catalytic surface probe, *Applied Catalysis A: General*, 148 (1997) 213-252.
- [82] X. Zhang, K.J. Klabunde, Superoxide (O₂⁻) on the surface of heat-treated ceria. Intermediates in the reversible oxygen to oxide transformation, *Inorganic Chemistry*, 31 (1992) 1706-1709.
- [83] C. Binet, M. Daturi, J.-C. Lavalley, IR study of polycrystalline ceria properties in oxidised and reduced states, *Catalysis Today*, 50 (1999) 207-225.
- [84] J. Guzman, S. Carrettin, A. Corma, Spectroscopic Evidence for the Supply of Reactive Oxygen during CO Oxidation Catalyzed by Gold Supported on Nanocrystalline CeO₂, *Journal of the American Chemical Society*, 127 (2005) 3286-3287.
- [85] S. Akhter, J.M. White, A static SIMS/TPD study of the kinetics of methoxy formation and decomposition on O/Pt(111), *Surface Science*, 167 (1986) 101-126.
- [86] A. Siokou, R.M. Nix, Interaction of Methanol with Well-Defined Ceria Surfaces: Reflection/Absorption Infrared Spectroscopy, X-ray Photoelectron Spectroscopy, and Temperature-Programmed Desorption Study, *The Journal of Physical Chemistry B*, 103 (1999) 6984-6997.
- [87] K.K. Kolasinski, K.W. Kolasinski, *Surface science: foundations of catalysis and nanoscience*, John Wiley & Sons, 2012.

Abbreviations

AES – Auger electron spectroscopy

CeO_x – Ceria

FFT – Fast Fourier transform

IRRAS – Infrared reflection-absorption spectroscopy

LEED – Low energy electron diffraction

LEEM – Low energy electron microscopy

MBE – Molecular beam epitaxy

MeOH – Methanol

ML – Monolayer

MLE – Monolayer equivalent

OCM – Oxidative coupling of methane

PrO_x – Praseodymia

REE – Rare earth element

REO – Rare earth oxide

RPVD – Reactive physical vapor deposition

SmO_x – Samaria

STM – Scanning tunneling microscopy

TbO_x – Terbia

TPD – Temperature programmed desorption

UHV – Ultra-high vacuum

WGS – Water gas shift

XPS – X-ray photoelectron spectroscopy

μLEED – Micro-illumination low energy electron diffraction

Curriculum Vitae

Jin-Hao Jhang

Born in Yunlin County, Taiwan, October 24th, 1984

Work Experience

PhD work

AG Bäumer, Institut für Angewandte und Physikalische Chemie (IAPC), Universität Bremen, September 2011 - 2015

Corporal

Taiwan Army (Conscription), 2010

Research assistant

National Science Council, Taiwan, 2008 - 2009

Teaching assistant

Department of Chemistry, National Taiwan Normal University, Taipei, Taiwan, 2007 - 2008

Education

PhD, Physical Chemistry

- Universität Bremen, Bremen, Germany, 2011 - 2015
- Thesis: Model Studies on Rare Earth Oxide Thin Films: Surface Chemistry and Catalytic Properties

Master, Chemistry with concentration in Physical Chemistry

- National Taiwan Normal University, Taipei, Taiwan, 2007 - 2009
- Thesis: Preparation of Hollow CdS Nanoparticles via Electrodeposition

Bachelor, Chemistry

- National Taiwan Normal University, Taipei, Taiwan, 2003 - 2007
- Thesis: Preparation and Application of Piezoelectric Crystal Sensor for Uric Acid Based on C₆₀-Uricase Immobilized Enzyme

Publications

Journal article

1. CO and D₂O chemistry on continuous and discontinuous samaria thin films on Pt(111), J.-H. Jhang, S. Keil, A. Schaefer, V. Zielasek, M. Bäumer, *Surface Science*, Submitted for Initial Review.
2. Methanol Adsorption and Reaction on Samaria Thin Films on Pt(111), J.-H. Jhang, A. Schaefer, V. Zielasek, J.F. Weaver, M. Bäumer, *Materials* **2015**, *8*, 6228 – 6256.
3. Controlling the Physicals and Chemistry of Binary and Ternary Praseodymium and Cerium Oxide Systems, G. Niu, M.H. Zoellner, T. Schroeder, A. Schaefer, J.-H. Jhang, V. Zielasek, M. Bäumer, H. Wilkens, J. Wollschläger, R. Olbrich, C. Lammers, M. Reichling, *Physical Chemistry Chemical Physics* **2015**.
4. Growth and Partial Reduction of Sm₂O₃(111) Thin Films on Pt(111): Evidence for the Formation of SmO(100), J.-H. Jhang, A. Schaefer, W. Cartas, S. Epuri, M. Bäumer, J.F. Weaver, *The Journal of Physical Chemistry C* **2013**, *117*, 21396 – 21406.
5. Temperature-Dependent Reduction of Epitaxial Ce_{1-x}Pr_xO_{2-δ} (x = 0 – 1) Thin Films on Si(111): A Combined Temperature-Programmed Desorption, X-ray Diffraction, X-ray Photoelectron Spectroscopy, and Raman Study, M.H. Zoellner, G. Niu, J.-H. Jhang, A. Schaefer, P. Zaumseil, M. Bäumer, T. Schroeder, *The Journal of Physical Chemistry C* **2013**, *117*, 24851 – 24857.
6. Electrodeposition of Long-Chain Alkylaryl Layers on Au Surfaces, S. Lin, C.-W. Lin, J.-H. Jhang, W.-H. Hung, *The Journal of Physical Chemistry C* **2012**, *116*, 17048 – 17054.
7. Hollow CdS Nanoparticles Formed through Electrochemical Deposition of Cd(OH)₂ on Graphite and Subsequent Treatment with H₂S, J.-H. Jhang, W.-H. Hung, *Materials Chemistry and Physics* **2011**, *129*, 512 – 516.

Additional information

- Exchange visitor in Department of Chemical Engineering, University of Florida, United States, 2012 and 2014
- Member of Deutsche Physikalische Gesellschaft
- User of Max-lab synchrotron radiation facility, Sweden
- User of National synchrotron radiation research center, Taiwan

Papers

Paper I.

Growth and Partial Reduction of $\text{Sm}_2\text{O}_3(111)$ Thin Films on Pt(111): Evidence for the Formation of $\text{SmO}(100)$, **J.-H. Jhang**, A. Schaefer, W. Cartas, S. Epuri, M. Bäumer, J.F. Weaver, *The Journal of Physical Chemistry C* **2013**, *117*, 21396 - 21406.

Paper II.

CO and D_2O Chemistry on Continuous and Discontinuous Samaria Thin Films on Pt(111), **J.-H. Jhang**, S. Keil, A. Schaefer, V. Zielasek, M. Bäumer, *Surface Science*, Submitted for Initial Review.

Paper III.

Methanol Adsorption and Reaction on Samaria Thin Films on Pt(111), **J.-H. Jhang**, A. Schaefer, V. Zielasek, J.F. Weaver, M. Bäumer, *Materials* **2015**, *8*, 6228 - 6256.

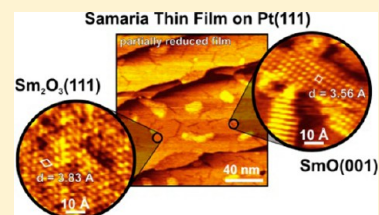
Growth and Partial Reduction of Sm₂O₃(111) Thin Films on Pt(111): Evidence for the Formation of SmO(100)

Jin-Hao Jhang,[†] Andreas Schaefer,^{*,†} William Cartas,[‡] Santosh Epuri,[‡] Marcus Bäumer,[†] and Jason F. Weaver^{*,‡}

[†]Institute of Applied and Physical Chemistry & Center for Environmental Research and Sustainable Technology, University of Bremen, Leobener Str., Bremen D-28359, Germany

[‡]Department of Chemical Engineering, University of Florida, Gainesville, Florida 32611, United States

ABSTRACT: We investigated the growth and partial reduction of Sm₂O₃(111) thin films on Pt(111) using low energy electron diffraction (LEED) and scanning tunneling microscopy (STM). We find that the Sm₂O₃(111) films are high quality and grow in a defective fluorite structure wherein the Sm cations adopt a hexagonal (1.37 × 1.37) lattice in registry with the Pt(111) surface, while oxygen vacancies are randomly distributed within the film. STM measurements show that Sm₂O₃(111) film growth on Pt(111) occurs by the Stranski-Krastanov mechanism, in which a single O–Sm–O trilayer initially forms, followed by the growth of well-defined, multilayer islands. The Sm₂O₃(111) films undergo partial reduction during annealing at 1000 K in ultrahigh vacuum. LEED and STM provide evidence that a fraction of the Sm₂O₃ in the first layer, closest to the Pt(111) substrate, decomposes to produce well-ordered domains of rocksalt SmO(100) during reduction, and that Sm₂O₃ from the third and higher layers concurrently spreads onto the first layer to form a more contiguous second layer of Sm₂O₃(111). We show that the SmO(100) and Sm₂O₃(111) lattices can form a coincidence structure with minimal strain to the Sm-atom sublattices, and that satellite features observed in the LEED patterns are consistent with the coexistence of SmO(100) and Sm₂O₃(111) domains as well as the proposed Sm₂O₃(111)/SmO(100) coincidence structure. Lastly, we find that reoxidation of the partially reduced films restores the original Sm₂O₃(111) crystal structure, and significantly improves the film quality, as reflected by a flatter film morphology and better connectivity among oxide domains. An implication from this study is that the formation of (100)-oriented monoxide structures is a general characteristic of the reduction of rare-earth oxide thin films on hexagonally close-packed metal surfaces.



INTRODUCTION

The oxides of the lanthanides, commonly called rare earth oxides (REOs), have received considerable attention because of their high potential for applications in diverse fields such as microelectronics and heterogeneous catalysis. In catalysis, rare earth oxides are employed in versatile applications, including the dehydrogenation and selective oxidation of organic compounds, the catalytic conversion of methane to synthesis gas, the oxidative coupling of methane and applications in three-way catalysis.^{1,2} The versatility of the REOs originates from the ease of valency changes of the rare earth metals, that is, the change of the *f*-orbital occupancy. Considering complete oxidation catalysis, the possible higher oxides in the REO series (e.g., CeO₂, Pr₆O₁₁, Tb₄O₇) are particularly interesting materials due to the high mobility of oxygen ions in the lattice³ and a wide structural variety.⁴ The lattice oxygen participates directly in the oxidation reaction (Mars-van-Krevelen mechanism⁵) and thus the selectivity of a REO catalyst can depend strongly on the oxygen storage and release properties. The higher oxides mentioned above are quite effective as complete oxidation catalysts, and ceria has been intensively studied in this respect.

In contrast, other rare earth oxides only form the sesquioxide (RE₂O₃) and tend to promote partial oxidation chemistry. For example, the sesquioxides samaria and lanthana exhibit high

selectivity in promoting partial oxidation processes, such as the oxidative coupling of methane.^{6–8} While the oxidation selectivity of REO catalysts originates generally from the ability of the REO to change structure and oxidation state, a fundamental understanding of the structure–reactivity relationships of REO catalysts is lacking. Interest in advancing this understanding provides considerable motivation for developing model surfaces of various REOs that are amenable to characterization using the diagnostic tools of ultrahigh vacuum (UHV) surface analysis.

Considerable progress has been made in the study of ceria thin films and structures on various transition metal substrates.^{9–20} This prior work demonstrates that high quality, crystalline CeO₂(111) thin films can be grown on low-index metal surfaces, particularly hexagonally close-packed surfaces including Cu(111),^{10,11} Ru(0001),^{14,21,22} Pt(111),^{9,12,20,23} Ni(111),¹⁴ Pd(111),¹³ and Rh(111).²⁴ This capability enables model studies of the chemical properties of well-defined ceria surfaces using a wide array of experimental methods. Because bulk CeO₂ adopts the cubic fluorite structure, the CeO₂(111) facet possesses the same hexagonal symmetry as hexagonally

Received: July 26, 2013

Revised: September 8, 2013

Published: September 16, 2013

close-packed metal surfaces and can consequently form a commensurate overlayer on these substrates with minimal strain to the ceria lattice. In contrast to ceria, however, few studies have explored the growth and properties of other REO thin films on metallic substrates. As a result, the basic understanding of catalytic trends across the REO series remains limited. Of particular interest is to determine how sesquioxides of the rare earth metals grow as thin films on crystalline metal surfaces since the RE_2O_3 form is common to the entire REO series.

Bulk rare-earth sesquioxides can form multiple crystal structures, though the C-type, bixbyite structure is the preferred structure for most of the REOs at normal pressures and temperatures. The bixbyite structure can be derived from the fluorite structure by removing two oxygen atoms from each unit cell of the fluorite structure.⁴ The resulting oxygen vacancies form an ordered superstructure in the bixbyite crystal and the metal cations relax from their original positions in the face-centered cubic sublattice. As a result, the volume of the bixbyite unit cell is about eight times larger than that of the fluorite unit cell, and the metal cations no longer exhibit the cubic symmetry of the fluorite structure. For example, the (111) plane of C-type Sm_2O_3 is characterized by a hexagonal unit cell with a lattice constant of 14.1 Å, where the lattice vector spans four distinct Sm–Sm bonds with lengths between about 3.3 and 3.8 Å.

Because of the lack of simple hexagonal symmetry, it is not obvious in advance how a sesquioxide that prefers the bixbyite structure in the bulk will grow as a thin film on a hexagonally, close-packed metal surface and indeed results differ among the few studies that have been reported. For example, Tao and Batzill have reported that $\text{Y}_2\text{O}_3(111)$ thin films grow in an incommensurate bixbyite structure on Pt(111), and obtain high quality films under UHV conditions.²⁵ In contrast, low energy electron diffraction (LEED) observations by Mullins suggest that $\text{Dy}_2\text{O}_3(111)$ films grow in a defective-fluorite structure on Ru(0001) that is commensurate with the substrate, even though bulk Dy_2O_3 prefers the bixbyite form.²⁶ An implication from these studies is that the oxide–substrate interaction plays an important role in determining the structure of sesquioxide thin films and probably the film quality as well.

In the present study, we characterized the growth and partial reduction of $\text{Sm}_2\text{O}_3(111)$ thin films on Pt(111) using LEED and scanning tunneling microscopy (STM). We find that high-quality $\text{Sm}_2\text{O}_3(111)$ films grow in a defective fluorite structure on Pt(111), and that the structural properties of the films can be modified through reduction-reoxidation cycles performed in UHV. Of particular significance is evidence that annealing in UHV causes the $\text{Sm}_2\text{O}_3(111)$ films to partially decompose to generate a mixture of rocksalt $\text{SmO}(100)$ and $\text{Sm}_2\text{O}_3(111)$. Our results provide a new model system for investigating the chemical properties of SmO_x surfaces, and can thus provide opportunities for advancing the fundamental understanding of factors governing the behavior of samaria-based catalysts.

More generally, the ability to generate high-quality samaria thin films further motivates efforts to develop other model REO surfaces, with the aim to enhance the understanding of trends along the REO series as well as to improve the understanding of existing systems. As has recently been shown for ceria islands grown on gold^{27,28} and copper,^{29,30} this approach has potential to provide a deeper understanding of the mechanisms important for eventually enhancing and tuning the catalytic properties of REOs. The ultimate goal of such model studies is to reach a level of understanding that enables the preparation of

REO catalysts with tunable activity and selectivity based on combining oxides with specific properties.

■ EXPERIMENTAL DETAILS

Our experiments were carried out in a UHV chamber with a typical base pressure of 2×10^{-10} Torr. Details of the UHV system are provided elsewhere.^{31,32} Briefly, the chamber is equipped with a scanning tunneling microscope, a four-grid LEED optics (OCI), a quadrupole mass spectrometer (Balzers), an ion sputter source, and an electron beam evaporator (McAllister Technical Services) for Sm deposition. We used an UHV 300 STM scan head (“beetle” type) produced by RHK and controlled with a RHK SPM 100 controller for these experiments. The microscope utilized Pt/Ir tips which were prepared by field-induced evaporation on a gold film. We typically applied $\sim 1 \mu\text{A}$ for 10 s when conditioning the tip of the UHV 300 scan head.

The Pt(111) single crystal used in this study is a circular disk (10 mm \times 1 mm) which is secured underneath a molybdenum top ramp for experiments in the STM chamber. We radiatively heated the sample using a tungsten filament and cooled the sample through a copper braid attached to a liquid-nitrogen cooled reservoir. We monitored the sample temperature using a type-K thermocouple that was spot-welded to the backside of the sample, and used a temperature controller interfaced to a DC power supply to maintain constant temperatures for isothermal experiments. We cleaned the sample by repeated cycles of sputtering with 600 eV Ar^+ ions at a sample temperature of 600 K with annealing to 1000 K, and also by heating in an O_2 background and flashing to 1000 K. We considered the surface to be clean when Auger electron spectra (AES) obtained from the Pt(111) sample exhibited negligible C(KLL) and O(KLL) peaks, a sharp LEED pattern characteristic of Pt(111) was observed, and large flat terraces were observed in STM images.

We grew samarium oxide films on Pt(111) by reactive physical vapor deposition (RPVD). We generated a Sm vapor flux using an electron beam evaporator with a tantalum crucible loaded with pieces of metallic Sm (Alfa Aesar, 99.9%). The evaporation was carried out in an O_2 background pressure of 5×10^{-7} Torr, with the Pt(111) crystal held at a temperature of 600 K. After discontinuing the Sm exposure, we annealed the sample at 1000 K and the same O_2 background pressure. We estimate that the average film growth rate employed in our experiments was 0.212 ± 0.006 ML/min, where this estimate is based on attenuation of the Pt(MNN) peak intensity at 238 eV observed in AES spectra and assumes an inelastic mean free path of 7.028 Å. We define the thickness of one monolayer (ML) of $\text{Sm}_2\text{O}_3(111)$ as equal to 3.18 Å which corresponds to the average separation between O–Sm–O trilayers along the $\langle 111 \rangle$ direction of the bixbyite structure of bulk c- Sm_2O_3 .³³ We started with a clean Pt(111) substrate to prepare each $\text{Sm}_2\text{O}_3(111)$ film discussed in this study.

We performed STM experiments at room temperature with the microscope operating in constant-current mode. We typically applied positive sample biases in the range of 0 to +1.0 V and tunneling currents in the range of 0.3–1.5 nA. We calibrated the lateral distances in the STM images of the $\text{Sm}_2\text{O}_3(111)$ thin films based on STM images of the $p(2 \times 2)$ superstructure of chemisorbed oxygen atoms on Pt(111) and assuming a lattice constant of 5.55 Å. We calibrated the heights measured perpendicularly to the surface based on the known height of a monatomic step on Pt(111) ($h = 2.3$ Å).

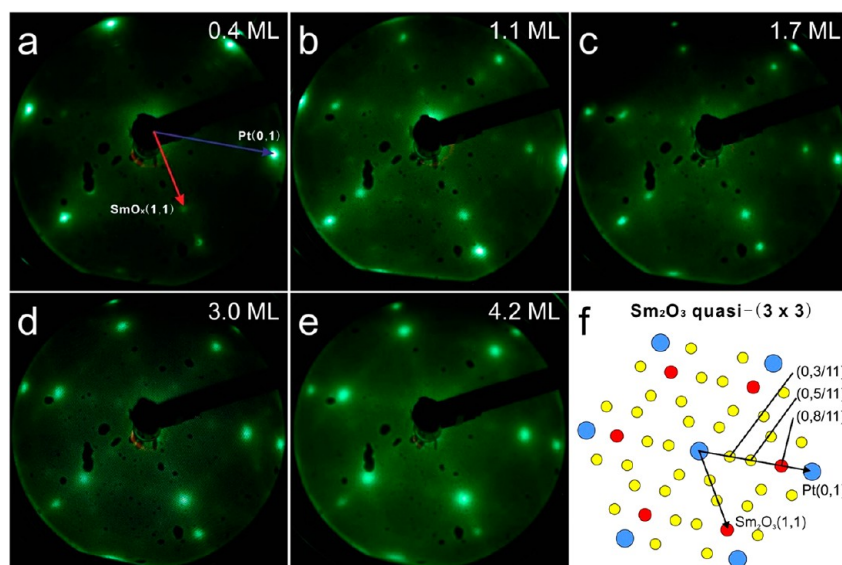


Figure 1. LEED patterns obtained after growing $\text{Sm}_2\text{O}_3(111)$ films on $\text{Pt}(111)$ to the coverages indicated followed by annealing in 5×10^{-7} Torr of O_2 at 1000 K for 10 min: (a) 0.4 ML of Sm_2O_3 shows a hexagonal (1.37×1.37) superstructure in registry with the $\text{Pt}(111)$ (1×1) spots, $E = 58$ eV, (b) 1.1 ML, $E = 48$ eV, (c) 1.7 ML, $E = 56$ eV, (d) 3.0 ML, $E = 52$ eV exhibit a quasi- (3×3) superstructure, (e) 4.2 ML, $E = 56$ eV; the quasi- (3×3) becoming blurry, and (f) shows a schematic representation of the quasi- (3×3) pattern that is determined from FFT analysis of a structural model of superposed, hexagonal Sm and Pt lattices that form a hexagonal (8×8) coincidence lattice with respect to the Sm lattice, i.e., (11×11) with respect to the Pt lattice. The labels are explained in more detail in the Discussion section.

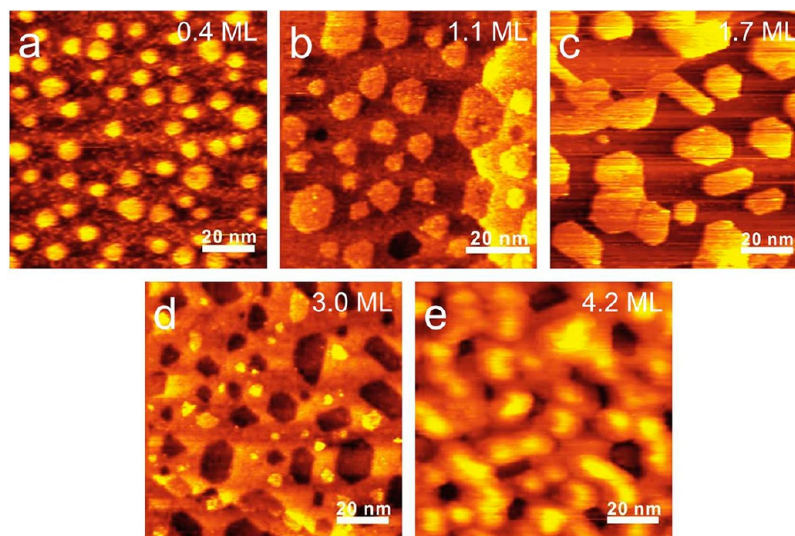


Figure 2. Topographic STM images ($100 \text{ nm} \times 100 \text{ nm}$) obtained after growing Sm_2O_3 films on $\text{Pt}(111)$ to the coverages indicated followed by annealing in 5×10^{-7} Torr of O_2 at 1000 K for 10 min: (a) 0.4 ML Sm_2O_3 (0.60 V, 0.83 nA), (b) 1.1 ML (0.60 V, 0.41 nA), (c) 1.7 ML (0.60 V, 1.19 nA), (d) 3.0 ML (0.60 V, 0.64 nA), and (e) 4.2 ML (0.60 V, 0.60 nA).

RESULTS

Growth of $\text{Sm}_2\text{O}_3(111)$ Thin Films on $\text{Pt}(111)$. After deposition of SmO_x onto the clean $\text{Pt}(111)$ surface, LEED shows only blurred $\text{Pt}(111)$ spots and an increase of the background intensity (not shown). To induce the formation of ordered SmO_x structures, we conducted a postannealing treatment in O_2 for each SmO_x film investigated (see the Experimental Details section). Other researchers have employed a similar approach to improve the ordering of rare earth oxide thin films, including $\text{CeO}_2(111)^{11,20,22}$ and $\text{Y}_2\text{O}_3(111)^{25}$. Figure 1a shows the LEED pattern obtained after postannealing in oxygen of a nominal oxide coverage of 0.4 ML. Bright substrate spots are visible accompanied by faint

spots of a hexagonal lattice in registry with $\text{Pt}(111)$ and forming a (1.37×1.37) structure, analogous to LEED patterns of $\text{CeO}_2(111)$ films grown on close-packed metal substrates.^{9–13,20,22–24} As the SmO_x coverage increases beyond 1 ML, the SmO_x related spots become more intense and the Pt spots are slightly attenuated. Overall, the spots are very sharp and thus indicative of a flat morphology of the SmO_x film.

For SmO_x coverages between ~ 1 and 3 ML, the LEED pattern exhibits additional spots (Figure 1b–d) which, at first glance, appear to adopt an arrangement that resembles a 3×3 superstructure with respect to the oxide lattice. However, close inspection reveals that the extra spots are arranged in the pattern depicted in Figure 1f. This pattern consists mainly of a hexagonal arrangement of spots centered around the SmO_x (1

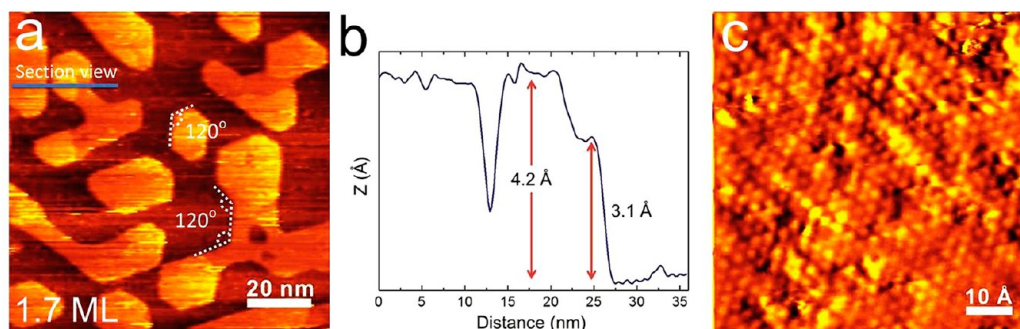


Figure 3. (a) Topographic STM image of a 1.7 ML $\text{Sm}_2\text{O}_3(111)$ film on Pt(111) showing hexagonal islands with enclosed angles of 120° ($100 \text{ nm} \times 100 \text{ nm}$, 0.60 V, 1.23 nA). (b) Height profile of an oxide island as estimated from the section view measurement in (a). (c) Atomically resolved STM image ($70 \text{ \AA} \times 70 \text{ \AA}$, 0.60 V, 0.59 nA) revealing a hexagonal arrangement of atoms on the islands as well as structural defects which appear as both bright and dark features.

$\times 1$) spots, resulting in a “quasi- 3×3 ” superstructure relative to the SmO_x lattice. The quasi- 3×3 superstructure is still visible after increasing the coverage to 3.0 ML, though the spots are more blurry which is indicative of a rougher film. This trend progresses when increasing to 4.2 ML nominal coverage (Figure 1e), in which case the SmO_x spots are very intense though even more blurry, and the Pt(111)-(1×1) spots are more attenuated. The LEED pattern obtained from the 4.2 ML film also exhibits higher background intensity, suggesting further roughening and thus a change in growth behavior.

The LEED observations provide evidence that samaria grows on Pt(111) as $\text{Sm}_2\text{O}_3(111)$ with an oxygen-deficient fluorite structure rather than the bixbyite structure. Our results specifically suggest that the Sm atoms adopt a face-centered cubic (FCC) lattice to achieve commensurability with the Pt(111) substrate, while oxygen vacancies are randomly distributed within the $\text{Sm}_2\text{O}_3(111)$ crystal structure. The Pt(111) substrate clearly forces the Sm atoms to arrange into a FCC (111) lattice, given that bulk Sm_2O_3 preferentially forms the bixbyite over a defective fluorite structure. A key difference between these structures is that the oxygen vacancies form an ordered superstructure in the bixbyite structure, resulting in a surface unit cell with dimensions that are about four times larger than that of the fluorite structure. We elaborate these observations and the $\text{Sm}_2\text{O}_3(111)/\text{Pt}(111)$ structure in the Discussion section.

We also conducted STM measurements after each preparation step presented above to further characterize the structure and growth behavior of the Sm_2O_3 film on Pt(111). We performed all STM measurements at room temperature. Figure 2 shows representative STM images for the five different Sm_2O_3 coverages discussed above. The predominant structural features during the initial stages of growth are small round islands with an average diameter of $\sim 95 \text{ \AA}$ and heights equal to $2.90 \pm 0.04 \text{ \AA}$ (Figure 2a). The island height is close to that of the separation between O–Sm–O trilayers (3.18 \AA) in the bixbyite form of bulk Sm_2O_3 . Considering tip convolution as well as effects caused by tunneling through a material with different electronic properties from the substrate (i.e., insulating in the case of bulk Sm_2O_3), it is reasonable to conclude that the islands observed at 0.4 ML correspond to a single O–Sm–O trilayer. We note that O–Sm–O trilayers represent the repeating structural element along the $\langle 111 \rangle$ direction of a defective fluorite or bixbyite Sm_2O_3 crystal. We thus refer to one O–Sm–O trilayer as a single “layer” of $\text{Sm}_2\text{O}_3(111)$ throughout the paper. “Wormlike” chain structures are also

discernible between the islands observed at 0.4 ML and are randomly oriented. The apparent height of these chain structures is $0.99 \pm 0.03 \text{ \AA}$, which is nearly three times smaller than the island heights. We speculate that the chain structures correspond to an initial SmO_x phase that acts as a precursor to the formation of O–Sm–O trilayer islands on Pt(111). While chain structures also form on pure Pt(111) during the initial stages of oxidation,^{32,34} Pt oxide chains are unlikely to form at the low O_2 pressures employed in the present oxidation treatment and, moreover, the PtO_x chains are stable in UHV only up to about 575 K. For these reasons, we assert that the chain structures observed after samaria deposition (Figure 2a) correspond to an initial SmO_x structure rather than a Pt oxide. Further support for this interpretation is our finding that the Sm_2O_3 coverages estimated from STM and AES show good agreement only when we assume that the observed chain structures are pure SmO_x . At 1.1 ML, the Sm_2O_3 islands have grown larger and begin to exhibit hexagonal shapes, while the chain structures between the islands appear to have coalesced and thickened, resulting in a more contiguous oxide layer (Figure 2b).

These morphological features are indicative of a Stranski-Krastanov growth mechanism wherein a single layer of $\text{Sm}_2\text{O}_3(111)$ (i.e., an O–Sm–O trilayer) wets the Pt(111) surface while $\text{Sm}_2\text{O}_3(111)$ islands nucleate and grow on top of the wetting layer. The appearance of hexagonal pits within the area between islands provides supporting evidence for the formation of a single wetting layer (Figure 2b). Coalesced hexagonal islands are the predominant structural element at 1.7 ML nominal coverage (Figure 2c). The film and the islands appear very flat, in agreement with the observation of sharp diffraction spots for this film (Figure 1c). Some of the islands seen in Figure 2c seem to exhibit two layers, as indicated by a change in image contrast across an island. Notably, the Sm_2O_3 domains appear to grow randomly across the Pt(111) surface, without a clear preference for nucleation at step edges.

At coverages above $\sim 3 \text{ ML}$, the morphology of the Sm_2O_3 layer begins to deviate from the atomically flat structures observed at lower coverage. As seen in Figure 2d, the 3.0 ML film exhibits large, flat domains with hexagonally shaped holes as well as small islands in the uppermost layer. The appearance of small islands on top of an incomplete Sm_2O_3 layer suggests that island growth becomes the dominant growth mode as the film thickens ($>3 \text{ ML}$). The roughening of the Sm_2O_3 layer that accompanies island growth is also consistent with the observation of more blurred samaria diffraction spots at

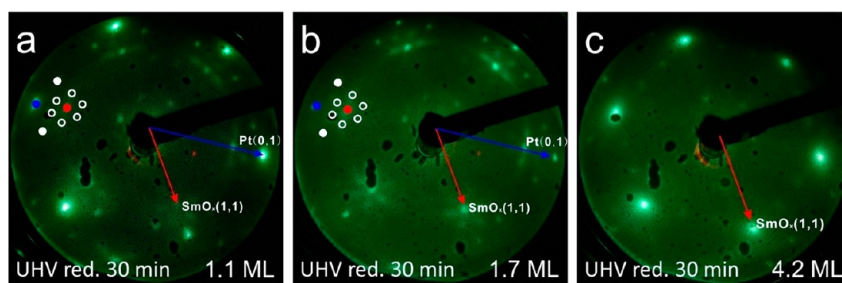


Figure 4. LEED patterns obtained after annealing $\text{Sm}_2\text{O}_3(111)$ films on $\text{Pt}(111)$ in UHV at 1000 K for 30 min. LEED patterns are shown for partially reduced films with initial Sm_2O_3 coverages of (a) 1.1 ML (64 eV), (b) 1.7 ML (58 eV), and (c) 4.2 ML (43 eV). Selected spots are highlighted to clarify the observed features. A $\text{Pt}(0,1)$ spot is marked with a solid blue circle, a main-order Sm spot (0, 8/11) from $\text{Sm}_2\text{O}_3(111)$ is marked with a solid red circle, the new satellite spots that form a hexagonal arrangement about the main-order Sm spot are marked with open circles, and two other spots near the Pt (0,1) spot are marked with solid white circles.

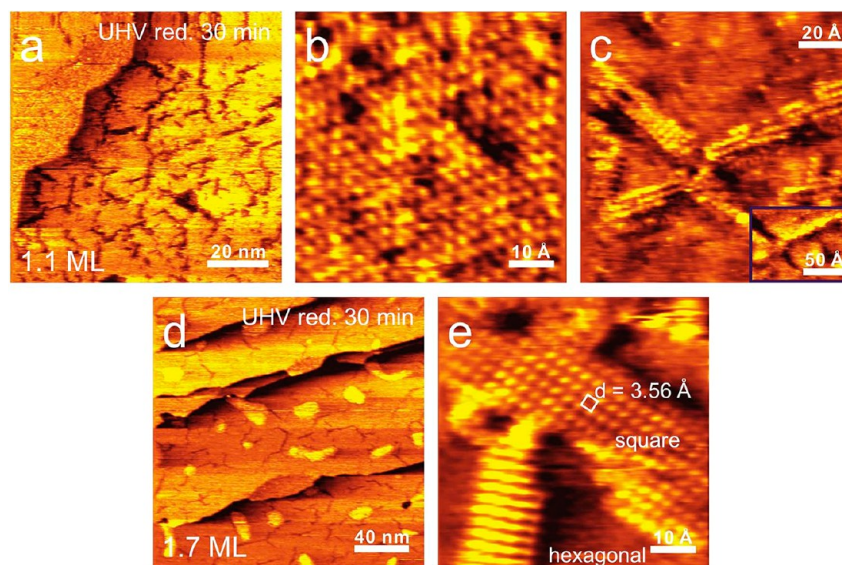


Figure 5. STM topographic and atomically resolved images obtained from 1.1 and 1.7 ML Sm_2O_3 films on $\text{Pt}(111)$ after partial reduction in UHV: (a) large-scale image of the partially reduced 1.1 ML film (100 nm \times 100 nm, 0.60 V, 0.53 nA), (b) atomically resolved image of a terrace region of the partially reduced 1.1 ML film showing the hexagonal $\text{Sm}_2\text{O}_3(111)$ lattice (60 Å \times 60 Å, 0.61 mV, 0.57 nA), (c) atomically resolved image of a crack-like region in (a) obtained by lowering the sample bias to 14.9 mV (120 Å \times 120 Å, $I = 0.50$ nA); the inset shows the same region of (c) with 0.60 V bias, (d) large-scale image of the partially reduced 1.7 ML film (200 nm \times 200 nm, 0.60 V, 1.22 nA), and (e) atomically resolved image of a crack formation obtained from the partially reduced 1.7 ML film, with the square unit cell indicated (60 Å \times 60 Å, 0.92 mV, 0.37 nA).

coverages above 3.0 ML (Figure 1d,e). The STM images obtained from a 4.2 ML film exhibit even larger islands on top of an incomplete oxide layer (Figure 2f), further demonstrating the dominance of island growth with increasing coverage under the conditions investigated. The images obtained from the 4.2 ML film are lower quality than those obtained from the thinner films because achieving stable tunneling conditions was challenging for the thicker and rougher layers.

Figure 3 shows higher resolution STM images and a line scan obtained from the 1.7 ML film. The typical hexagonal shape of the islands as well as the different contrast on the island structures is evident in Figure 3a. A line scan over a Sm_2O_3 island reveals that the first layer of the island exhibits a step height of 3.09 ± 0.05 Å, while the height of the second step is measured to be only 1.1 ± 0.05 Å. The measured island height is very close to that of the O–Sm–O trilayer separation (3.18 Å).³³ We note that the islands presumably reside on top of a single $\text{Sm}_2\text{O}_3(111)$ layer, which is conformal with the $\text{Pt}(111)$ substrate, and thus the measured height of 3.09 Å represents the separation between the first and second O–Sm–O trilayers of the film. The area on the island that exhibits an apparent

height of 1.1 Å may correspond to an intermediate structure that would develop into a new O–Sm–O trilayer during additional oxide deposition. However, a more likely interpretation is that the area of higher contrast corresponds to a completed trilayer on top of the island (i.e., the third trilayer measured from the $\text{Pt}(111)$ surface) but that tunneling through this layer differs from that through the first layer of the island such that the apparent height is considerably smaller than the separation between trilayers.

The atomically resolved image of the top level of a Sm_2O_3 island (Figure 3c) reveals a hexagonal arrangement of atoms, as already inferred from the LEED observations. We estimate a lattice constant of 3.83 ± 0.05 Å from the STM images, which agrees well with the value (3.81 Å) determined from LEED patterns obtained from the Sm_2O_3 -covered $\text{Pt}(111)$ surfaces. Since a positive bias was applied to the sample, the STM measurements probed empty states of the deposited Sm_2O_3 film which are expected to mainly exhibit Sm 4f characteristics. As such, the STM image shown in Figure 3c reveals the Sm atom positions and thus shows that the Sm atoms adopt a hexagonal arrangement on $\text{Pt}(111)$. The image further shows

that point defects are present in high concentrations on the island. The point defects are evident as both bright and dark features, with several exhibiting triangular shapes that are similar to structures observed on $\text{CeO}_2(111)$ surfaces,^{9,16,22,35,36} including oxygen vacancies and hydroxyl groups. The defects are randomly distributed on the surface of the Sm_2O_3 island, which is consistent with the conclusion that the Sm_2O_3 film grows on Pt(111) as a defective fluorite structure rather than the bixbyite structure.

Partial Reduction of $\text{Sm}_2\text{O}_3(111)$ by Annealing in UHV. To investigate the thermal stability of the deposited oxide layers, we annealed selected films to 1000 K for 30 min in UHV and characterized the resulting structures using LEED and STM. Figure 4 shows representative LEED patterns obtained after annealing the specified $\text{Sm}_2\text{O}_3(111)$ films in UHV. Annealing of the 1.1 ML film leads to the appearance of satellite spots in a hexagonal arrangement around the $\text{Sm}_2\text{O}_3(111)$ main order spots, where the satellite hexagon is rotated by 30° with respect to the oxide lattice. Also, the diffraction spots associated with the quasi- 3×3 superstructure appear to have vanished after annealing, though a hexagonal arrangement of spots centered at (0,0) is still visible. We obtained a similar result after annealing the 1.7 ML film to 1000 K (Figure 4b). The only difference is that the oxide and satellite spots are more intense compared with those observed at lower coverage (Figure 4a). Annealing of a thicker film with 4.2 ML nominal coverage does not lead to the appearance of extra satellite spots (Figure 4c), even after doubling the annealing time to 60 min.

We also used STM to examine the morphological and structural changes that occur during annealing in UHV, focusing on characterizing the thinner films. Figure 5 shows representative STM images obtained after partially reducing the 1.1 and 1.7 ML Sm_2O_3 films in the manner described above. After annealing, the low-coverage films (~ 1 to 2 ML) exhibit large, flat terraces that contain cracklike formations which are visible as dark depressions (Figure 5a). Atomically resolved images show that the hexagonal $\text{Sm}_2\text{O}_3(111)$ structure comprises the large terraces (Figure 5b). The “cracks” are oriented at 120° from one another and align with the main directions of the hexagonal structure of the film and/or substrate. By decreasing the applied bias drastically from 0.6 V to 0.9 mV, the crack formations change in contrast and appear as atomic scale protrusions (Figure 5c,e). The atomically resolved images reveal that the atoms within the cracks arrange into a square lattice with a mean lattice constant of 3.56 ± 0.03 Å. This value is very close to the Sm–Sm distance (3.52 Å) in the (100) plane of rocksalt SmO .³⁷ The STM measurements thus provide evidence that Sm_2O_3 films on Pt(111) can be partially reduced by annealing to 1000 K in UHV, resulting in coexisting $\text{Sm}_2\text{O}_3(111)$ and $\text{SmO}(100)$ structures. Notably, we did not observe indications for complete oxide decomposition and Sm–Pt alloy formation under the conditions studied, as elaborated in the Discussion. Annealing for longer times or at higher temperatures may result in complete decomposition of the Sm_2O_3 films, and would be interesting to pursue in future studies. Key implications of the annealing experiments are that $\text{SmO}(100)$ is stable on Pt(111) and likely serves as an intermediate phase in the complete reduction of the Sm_2O_3 films.

Reoxidation of the Partially Reduced Samaria Films. After characterizing the UHV-annealed films, we repeated the annealing treatment in 5×10^{-7} Torr of O_2 to determine if the

partial reduction is reversible. We find that this annealing treatment regenerates the original Sm_2O_3 crystal structure, and significantly improves the film flatness and connectivity among domains. Figure 6 shows LEED and STM results obtained after

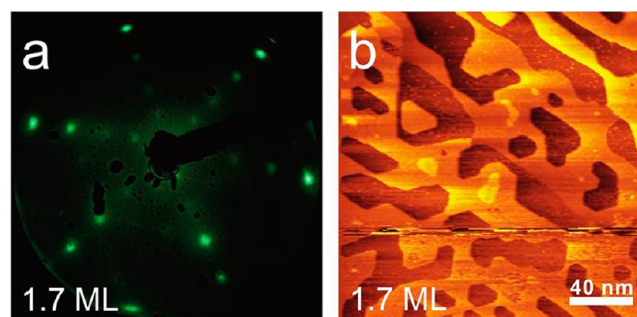


Figure 6. (a) LEED pattern obtained from a 1.7 ML $\text{Sm}_2\text{O}_3(111)$ film on Pt(111) after partial reduction and reoxidation at 1000 K in 5×10^{-7} Torr of O_2 . (b) STM image of the reoxidized 1.7 ML $\text{Sm}_2\text{O}_3(111)$ film revealing highly interconnected domains (200 nm \times 200 nm, 0.60 V, 0.89 nA).

reoxidizing the partially reduced 1.7 ML film at 1000 K. Reoxidation causes the satellites observed in the LEED pattern obtained after UHV annealing to vanish, while the quasi- 3×3 pattern reappears and is better resolved than that observed in the LEED pattern from the original 1.7 ML film (Figure 1c). Overall, we observe a high quality LEED pattern after reoxidation that is characterized by intense and sharp oxide spots as well as well-defined spots from the quasi- 3×3 superstructure and a low background intensity. These observations are indicative of an atomically flat film with large crystalline domains. Consistent with this interpretation, STM images show that the reoxidized film consists of flat, interconnected domains with a step height of 3.33 ± 0.05 Å (Figure 6b). A few small islands are also sparsely distributed on the large domains. A key finding is that the reoxidation treatment not only regenerates the crystalline $\text{Sm}_2\text{O}_3(111)$ structure but also produces a higher quality film, with respect to film flatness and connectivity among domains, compared with that obtained in the original preparation.

DISCUSSION

Growth and Structure of $\text{Sm}_2\text{O}_3(111)$ Films on Pt(111).

Our results demonstrate that $\text{Sm}_2\text{O}_3(111)$ thin films grow on Pt(111) in a defective fluorite structure in which the Sm cations arrange into a hexagonal sublattice in registry with the Pt(111) substrate, while the oxygen vacancies are randomly distributed within the Sm_2O_3 structure. The lattice constant of the hexagonal Sm structure (~ 3.82 Å) lies within the range of Sm–Sm distances reported for bulk Sm_2O_3 in the bixbyite structure.³³ The lattice constants determined from LEED and STM images are in excellent agreement, and the LEED experiments further show that the Sm lattice aligns with the high symmetry directions of the Pt(111) surface. The hexagonal 1.37×1.37 unit cell that we identified with LEED is indeed very similar to LEED patterns reported for fluorite $\text{CeO}_2(111)$ thin films grown on hexagonally close-packed metal substrates.^{9–13,20,22–24} Mullins has also reported evidence from LEED measurements that $\text{Dy}_2\text{O}_3(111)$ films form a defective fluorite structure on Ru(0001).²⁶ Consistent with our LEED observations, atomically resolved STM images show a regular,

hexagonal lattice as well as randomly distributed point defects, many of which must correspond to oxygen vacancies. The observation of randomly distributed point defects is consistent with the LEED and STM results which show that the Sm atoms form a regular, hexagonal structure rather than the larger unit cell of the bixbyite structure that results from vacancy ordering. The finding that $\text{Sm}_2\text{O}_3(111)$ forms a defective fluorite structure on Pt(111) suggests that formation of a hexagonal Sm lattice that is commensurate with the Pt(111) substrate is more energetically favorable than the formation of the bixbyite structure. An implication is that the Sm–Pt(111) interaction is strong enough to overcome the driving force for vacancy ordering which is responsible for the preferential formation of the bixbyite over the defective fluorite form of bulk Sm_2O_3 .

At coverages between about 1 and 3 ML, the LEED patterns that we obtain from the Sm_2O_3 films exhibit additional diffraction spots that arrange into the quasi- 3×3 pattern shown in Figure 1f. The extra spots begin to fade as the Sm_2O_3 films thicken above about 3 ML. Other researchers have observed similar LEED patterns obtained from ultrathin $\text{CeO}_2(111)$ films grown on metallic substrates, including Pt(111), and also report that the extra spots vanish as the oxide films become sufficiently thick.^{10,21,23} We performed an analysis which provides evidence that the quasi- 3×3 LEED pattern arises from double diffraction from a coincidence lattice formed between the hexagonal Sm sublattice and the Pt(111) substrate. In the analysis, we generated a real-space model of the superposed Sm and Pt lattices and then applied a fast Fourier transform (FFT) to simulate the diffraction pattern. In the real-space structure, the Sm and Pt(111) lattice vectors are parallel and form a hexagonal coincidence lattice, with sides that are 11 times longer than the Pt(111) lattice constant and 8 times longer than the lattice constant of the hexagonal Sm sublattice of $\text{Sm}_2\text{O}_3(111)$.

The FFT image obtained from the real-space model is schematically represented in Figure 1f, and agrees closely with the quasi- 3×3 LEED pattern that we measured. The extra spots generated by the FFT form hexagonal arrangements centered at the main-order Sm and Pt spots, with a spot-to-spot separation equivalent to $8/3$ of the Sm lattice constant. Along a line connecting the (0,0) and Pt(0,1) diffraction spots, the main-order Sm spot is located at the (0, $8/11$) position and diffraction from the coincidence lattice generates bright spots at the (0, $3/11$) and (0, $5/11$) positions or, equivalently, the (0, 0.27) and (0, 0.46) positions (cf. labels in Figure 1f). An 11×11 coincidence structure on Pt(111) can produce diffraction spots at all integer multiples of the $1/11$ positions; however, double diffraction processes cause certain scattered beams to be more intense than others. In particular, detailed analysis predicts that the most intense double-diffraction LEED spots arise from combinations of low-order overlayer and substrate reciprocal lattice vectors, and that the intensities diminish significantly for spots produced by higher-order combinations.³⁸ To further clarify the origin of the quasi- 3×3 LEED pattern, we calculated the scattering directions for double diffraction processes from the $\text{Sm}_2\text{O}_3(111)$ layer on Pt(111). Indeed, we find that combinations of low-order reciprocal lattice vectors from the overlayer and substrate only produce LEED spots at the $3/11$, $5/11$, and $8/11$ positions, while spots at other multiples of $1/11$ are produced by higher-order combinations. The good agreement between the simulated and measured LEED patterns of the superstructure suggests that the

Sm atoms of the oxide organize into the same hexagonal structure in the first oxide layer as in subsequent layers.

The manner in which the intensity of the quasi- 3×3 LEED spots vary with the film growth/processing conditions is also consistent with electron diffraction from a $\text{Sm}_2\text{O}_3(111)/\text{Pt}(111)$ coincidence lattice. For example, we find that the quasi- 3×3 pattern diminishes with increasing film thickness, which is consistent with attenuation of scattered electrons originating from the oxide-metal interface. Also, the superstructure pattern becomes most intense when the first layer is complete, and the second layer domains are large, as is the case for Sm_2O_3 films between 1 and 3 ML and is particularly true for the reoxidized films which exhibit large, interconnected domains.

Our results also show that, under the conditions studied, $\text{Sm}_2\text{O}_3(111)$ films grow on Pt(111) by a mechanism that is similar to the Stranski-Krastanov mechanism, wherein a single wetting layer develops initially, followed by the growth of oxide islands in multiple layers. The STM images show that the first layer initially forms as chain structures in high density that coexist with trilayer O–Sm–O islands. The chains likely correspond to an intermediate SmO_x structure that rearranges to form trilayer islands during additional deposition. As mentioned above, the formation of stable Pt oxide chains is unlikely under the high-temperature oxidation conditions employed in the present study.^{32,34} A single trilayer appears to be complete once the nominal oxide coverage reaches 1.1 ML, with this O–Sm–O trilayer constituting the first “layer” of the $\text{Sm}_2\text{O}_3(111)$ film. In contrast, at 1.7 ML nominal coverage, we estimate that second and third layer islands cover about 46% and 37% of the surface area, respectively, leaving the first layer exposed in 54% of the surface. Third layer islands thus begin to form well before the second layer is complete. In fact, the STM images obtained at higher coverages show that the second and higher layers contain an appreciable concentration of hexagonal holes, and remain incompletely formed up to a nominal $\text{Sm}_2\text{O}_3(111)$ coverage of 4.2 ML.

The formation of a conformal wetting layer on the Pt(111) substrate is indicative of a relatively strong Sm_2O_3 –Pt(111) interaction which forces the Sm atoms to adopt a regular, hexagonal structure. The failure of the second and higher layers to close may result from strain within the $\text{Sm}_2\text{O}_3(111)$ structure that is associated with the formation of a defective fluorite structure, especially given that this structure is unfavorable relative to the bixbyite form of bulk Sm_2O_3 . Although the Sm_2O_3 films undergo island thickening above ~ 1 ML, the film morphology is quite favorable up to about 3 ML as the second layer is well-connected with step edges located predominately within the hexagonal pits in the layer.

Partial Reduction of $\text{Sm}_2\text{O}_3(111)$ Films on Pt(111). Our results show that annealing in UHV at 1000 K causes a fraction of the $\text{Sm}_2\text{O}_3(111)$ film to partially reduce to rocksalt $\text{SmO}(100)$. The LEED patterns obtained from the partially reduced surface at Sm_2O_3 coverages between ~ 1 and 2 ML exhibit a hexagonal arrangement of satellite spots centered at the main-order $\text{Sm}_2\text{O}_3(111)$ spots, while the extra spots of the quasi- 3×3 pattern have vanished. STM images show that the partially reduced surface is comprised of large and flat $\text{Sm}_2\text{O}_3(111)$ terraces with cracks that appear as depressions within the film. Atomically resolved images reveal that the crack formations are occupied by a structure with a square periodicity with a lattice constant of 3.56 Å. As mentioned above, the measured lattice constant agrees well with that reported for the

rocksalt SmO(100) plane (3.52 Å). The (100) plane of a rocksalt monoxide is nonpolar and is the most stable facet of this material. Interestingly, bulk SmO is only stable under rather extreme conditions,^{4,39} implying that the oxide-Pt(111) interaction promotes the partial reduction of Sm₂O₃ to SmO.

We conclude that a fraction of the first Sm₂O₃(111) layer decomposes to SmO(100) during heating in UHV, while the third Sm₂O₃ layer concurrently spreads onto the first layer. The result is a nearly contiguous Sm₂O₃(111) second layer with exposed regions of SmO(100) evident as cracks from the first layer. The covered areas estimated from the STM images are consistent with this interpretation. For example, in the initial 1.7 ML Sm₂O₃ film, we estimate that the second and third layers constitute about 46% and 37% of the total surface area, respectively; that is, the first layer is visible in about 54% of the imaged areas. After partial reduction, the third layer is nearly depleted and the second layer appears to cover about 92% of the surface area, with the SmO(100) cracks accounting for the remaining area. We emphasize that the domain areas estimated from STM images represent only a small portion of the surface, and that variations in these areas can exist across the entire surface. Although this uncertainty exists, the area comparison is consistent with the idea that a large fraction of the third layer Sm₂O₃(111) moves into the second layer during partial reduction. It is worth noting that the density of Sm atoms is nearly identical in the Sm₂O₃(111) and SmO(100) planes based on the measured lattice constants. The similar Sm atom densities may facilitate the transformation of Sm₂O₃(111) to SmO(100) during reduction.

Additional evidence that reduction occurs mainly in the first oxide layer (i.e., the layer closest to the Pt(111) substrate) is the disappearance of the quasi-3 × 3 LEED pattern after partial reduction. Based on the interpretation given in the previous section, loss of the quasi-3 × 3 LEED pattern suggests that partial reduction eliminates large domains of the Sm₂O₃(111)/Pt(111) interface since sufficiently large coincidence regions of the Sm₂O₃(111) and Pt(111) lattices are needed to produce an observable quasi-3 × 3 pattern in LEED. The low bias used to atomically resolve the SmO(100) structure with STM also suggests that the SmO(100) structure lies on top of the Pt(111) surface. In particular, since bulk SmO exhibits metallic character,⁴ it should be possible to achieve electron tunneling through a single SmO(100) layer on Pt(111) using a very low potential, as observed, whereas larger potentials are needed to tunnel through a Sm₂O₃(111) layer. Notably, very low biases are typically required to atomically resolve close-packed metal surfaces due to the low electronic corrugation caused by electron delocalization. It should be mentioned, however, that a single oxide layer on a metallic surface can exhibit distinct electronic properties compared with the bulk oxide, so achieving atomic resolution using a low sample-to-tip bias is not necessarily proof that the corresponding bulk oxide is metallic. At the least, the different bias conditions needed to resolve the SmO(100) vs Sm₂O₃(111) structures on Pt(111) suggests that these structures have quite different electronic properties.

Characteristics of the LEED patterns obtained from the partially reduced surfaces are consistent with the coexistence of Sm₂O₃(111) and SmO(100) domains and the formation of a coincidence lattice between these structures. The satellite spots observed in the LEED pattern (Figure 4a, b) form a hexagonal arrangement centered on the main-order Sm₂O₃(111) spots, which suggests that partial reduction creates a new ordered

structure that adopts an epitaxial relationship with the hexagonal Sm sublattice of Sm₂O₃(111). The satellite spots thus seem inconsistent with the formation of an ordered Sm–Pt(111) alloy since such a structure is likely to produce new diffraction features that are clearly associated with the main-order Pt(111) spots. Notably, surface alloy structures that form in related systems (e.g., Ce–Pt(111)) differ significantly from the structures that we observe after partial reduction.^{40,41} To test these ideas, we explored viable ways to form epitaxial relationships between the Sm₂O₃(111) and SmO(100) lattices.

Figure 7a shows the optimal commensurate structure of the Sm₂O₃(111)/SmO(100) lattices that we identified. In this

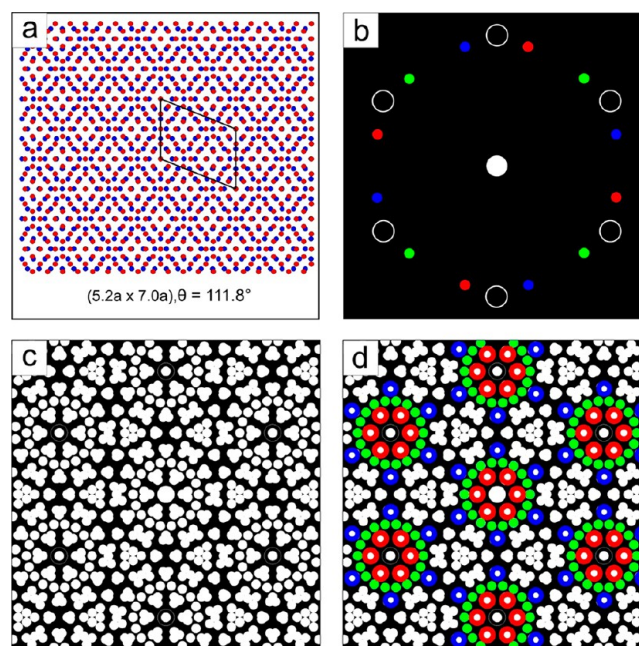


Figure 7. (a) Model of a commensurate overlayer structure of Sm₂O₃(111) on SmO(100). Blue circles represent Sm atoms in the hexagonal Sm₂O₃(111) lattice and red circles represent Sm atoms in the square SmO(100) lattice. The unit cell of the coincidence lattice is illustrated and the dimensions are given. (b) Simulated LEED pattern for three rotational domains of the square SmO(100) lattice (colored) coexisting with separate domains of Sm₂O₃(111) (open circles). The relative orientations of the lattices match those shown in the overlayer model. (c) Simulated LEED pattern of the three rotational domains of the coincidence lattice (filled) as an overlayer on Sm₂O₃(111) (open circles). (d) Simulated LEED pattern in (c) with specific arrangements of spots highlighted, as discussed in the text.

structure, the square lattice of SmO(100) is oriented such that its diagonal aligns along the unit cell vector and thus also along the long diagonal of the hexagonal unit cell of Sm₂O₃(111). Along the direction in which the diagonals are parallel, and defining the lattice constants of Sm₂O₃(111) and SmO(100) as a and b , respectively, we find a coincidence lattice defined by the relation $4\sqrt{2}b = 3\sqrt{3}a$, with $a = 3.81$ Å and $b = 3.50$ Å. The second lattice vector has a length equal to $\sqrt{29}(\sqrt{2}b)$ and forms an angle of 111.8° with the first lattice vector. To determine the epitaxial relationship, we fixed the value of a at the measured value and adjusted b to optimize the commensurability between the lattices. The optimal value of b differs by less than 2% from the value that we estimate from the STM images, and agrees to within 0.6% of the lattice constant of the bulk SmO(100) plane reported in the literature.

Thus, the SmO(100) and Sm₂O₃(111) lattices can form the epitaxial relationship depicted in Figure 7a with minimal strain to the structures.

The epitaxial Sm₂O₃(111)/SmO(100) structure can explain several of the features observed in the LEED patterns obtained from the partially reduced surfaces, though we are unable to reproduce all features of the measured LEED pattern. For example, the LEED pattern depicted in Figure 7b would result from separate, coexisting domains of Sm₂O₃(111) and SmO(100) in which the lattices adopt the relative orientation shown in the epitaxial model (Figure 7a). In this case, the square lattice of SmO(100) produces LEED spots on each side of the main-order Sm₂O₃(111) spots, giving rise to the appearance of triplets that reside along a ring centered on the (0,0) spot. Other researchers have reported LEED patterns that resemble that shown in Figure 7b,²⁰ and we have also observed an analogous pattern after annealing Sm₂O₃(111) films in UHV. In these cases, the LEED patterns are similar to those shown in Figures 4a and b, but only two satellite spots are observable at each main-order spot. We have not yet determined the conditions that cause the LEED pattern obtained from a partially reduced film to resemble that shown in Figure 7b, but we note that the LEED patterns shown in Figure 4a,b were highly reproducible. Although the calculated LEED pattern shown in Figure 7b qualitatively resembles patterns observed by others as well as the present study, the separation between the SmO(100) spots and the main-order Sm₂O₃(111) spots is larger in the calculated pattern compared with the measured patterns. This difference implies that reproducing the LEED pattern obtained from the partially reduced film requires consideration of factors other than only the coexistence of separate Sm₂O₃(111) and SmO(100) domains.

We also simulated LEED patterns for structural models that include the coincidence structure depicted in Figure 7a. For example, we performed FFT analysis of the real-space structural model but were unable to exactly reproduce the satellite structure seen in the measured LEED pattern. We find that the FFT analysis is sensitive to small variations in the lattice constants of the Sm₂O₃(111) and SmO(100) structures and may thus be unable to reliably reproduce the measured LEED pattern for this structure. We also used the LEEDpat software⁴² to simulate the LEED pattern of the proposed Sm₂O₃(111)/SmO(100) coincidence lattice superposed on the hexagonal Sm₂O₃(111) lattice. This simulation treats the coincidence lattice as a so-called simple overlayer on the hexagonal Sm₂O₃(111) structure wherein scattering centers from the overlayer are located only on the corners of the coincidence lattice unit cell. Such a simulation can reveal the possible locations of LEED spots that originate from the true coincidence structure formed between Sm₂O₃(111) and SmO(100), but does not provide information about the spot intensities. As seen in Figure 7c, the computed LEED pattern exhibits many more diffraction spots than are evident in the measured LEED patterns, with spots arising from three rotational domains of the coincidence lattice on Sm₂O₃(111).

In Figure 7d, we highlight specific arrangements to better illustrate features that appear in the predicted LEED pattern. Overlap of spots from the rotational domains of the coincidence lattice generates triplets that arrange into hexagonal formations (red and blue) centered around the main-order Sm₂O₃(111) spots, while eighteen individual spots (green) form rings around the main-order spots. The

orientation and spacing of the red hexagonal arrangement agrees well with the characteristics of the measured satellite structure obtained from the partially reduced Sm₂O₃(111) films; the measured vs computed separation between the main-order and satellite spots is 6.0a vs 6.1a, respectively. Notably, the LEED spots produced by the SmO(100) structure (Figure 7b) lie just outside of the satellite spots (Figure 7d, red) predicted for the coincidence lattice. The orientation and spacing of the blue hexagonal arrangement also closely matches a hexagonal arrangement centered on the (0,0) spot in the measured pattern (Figure 4a, b). The absence of many of the predicted superstructure spots from the measured LEED patterns may result from destructive interference caused by multiple-diffraction processes, neglect of the Pt(111) substrate in the LEED simulations, small domain sizes, instrumental limitations and energy-dependent effects in the electron scattering. More detailed studies are needed to fully characterize the structure of the partially reduced Sm₂O₃(111) films and test the proposed structure. Overall, however, the agreement between the simulated and measured LEED patterns supports the interpretation that the proposed Sm₂O₃(111)/SmO(100) coincidence structure develops during partial reduction of the Sm₂O₃(111) films on Pt(111) and is responsible for the satellite features observed in the LEED patterns.

Reoxidation of Partially Reduced Sm₂O₃(111) Films on Pt(111). Our results show that the original Sm₂O₃(111) crystal structure can be restored by oxidizing the partially reduced films, thus demonstrating that oxidation of SmO(100) to Sm₂O₃(111) is facile under the conditions studied. The reoxidation treatment also improves the film flatness and connectivity among domains of the ~1–2 ML Sm₂O₃(111) films compared with those obtained in the original preparation. An implication is that the extensive coalescence that occurs in the second layer during partial reduction is largely preserved when the surface is reoxidized. Interestingly, the fraction of first-layer areas that can be seen in STM images obtained from the reoxidized films is only slightly smaller than that observed in the original film, even though most of the first layer of the partially reduced film is covered. For example, we estimate that exposed areas of the first layer constitute about 54% of the total surface area in the original 1.7 ML film, but that this exposed area decreases to ~8% after partial reduction. After reoxidation, we find that the first layer accounts for about 39% of the exposed area in the images that we analyzed. These observations reveal that the reduction-reoxidation process significantly improves the connectivity among domains of the Sm₂O₃(111) films, but suggest that an appreciable fraction of the second layer of Sm₂O₃(111) migrates to the third layer during oxidation of the partially reduced film, thus preventing the formation of a conformal second layer. The apparent migration of Sm₂O₃ from the second to the third layer during reoxidation may mitigate strain that would develop in a conformal second layer of Sm₂O₃(111).

To conclude, we note that the present study appears to be the first to report the formation of a crystalline, rare-earth monoxide phase on a metallic substrate. Interestingly, however, comparing the present LEED results with those obtained in prior investigations suggests that CeO(100) is also produced during the thermal decomposition of CeO₂(111) thin films on hexagonally close-packed metal surfaces. We base this conclusion on the observation that LEED patterns with similar satellite features as shown in Figure 4 have been observed during the thermal reduction of CeO₂(111) films on Rh(111)

in UHV²⁴ as well as after annealing a low-coverage (0.7 ML) layer of Ce oxide on Pt(111) in an O₂ background at 1040 K.²⁰ Although the Ce oxide layer was annealed in O₂ in the latter case, the conditions appear to have caused partial reduction, resulting in a mixture of CeO(100) and CeO_x(111). These findings are interesting as they suggest the possibility of performing systematic UHV investigations with well-defined rare earth monoxide and sesquioxide structures using a given thin-film/substrate combination. This capability may provide new opportunities for determining how distinct structures and oxidation states influence the surface chemical properties of rare-earth oxide films, particularly the ability of the oxide to exchange oxygen with adsorbed reactants and thereby promote partial vs complete oxidation chemistry.

An important issue for future studies is to more fully characterize the structures that develop during the complete reduction of Sm₂O₃(111) films on Pt(111). Prior studies indeed show that multiple ordered structures can form as CeO₂(111) thin films thermally decompose, including ordered surface alloys once reduction of the ceria film is completed.^{12,24} Also, after partial reduction of a CeO₂(111) film on Pt(111), Luches et al.²⁰ have observed a complex LEED pattern that differs from those presented here for the SmO(100)/Sm₂O₃(111) structure. This observation may indicate that the CeO(100) phase decomposes to form distinct oxide structures prior to complete reduction or that the CeO(100) phase does not form at all under the specific reduction conditions that those researchers applied.

Lastly, it is important to point out that the total amount of SmO(100) produced in our experiments is difficult to estimate because a fraction of this phase presumably resides underneath the Sm₂O₃(111) second layer, and the exposed areas of SmO(100) are relatively small for the conditions studied. From the STM images, we estimate that the exposed regions of SmO(100) constitute about 8% and 13% of the total surface area for the partially reduced 1.7 and 1.1 ML films, respectively. It may be possible to generate films with larger areas of exposed SmO(100) under conditions that have not yet been studied, such as lower initial Sm₂O₃(111) coverage or higher reduction temperatures. We are planning studies to characterize other ordered structures that form during the reduction of Sm₂O₃(111) films and also determine if large domains of SmO(100) can be produced. This latter capability would facilitate systematic investigations of the surface chemistry of SmO(100) and Sm₂O₃(111) layers on Pt(111).

SUMMARY

We used LEED and STM to investigate the growth and partial reduction of Sm₂O₃(111) thin films on Pt(111) for oxide coverages up to ~4 ML. We find that the Sm₂O₃(111) thin films are high quality and grow as a defective fluorite structure on Pt(111) wherein the Sm atoms arrange into a well-ordered, hexagonal (1.37 × 1.37) sublattice in registry with the Pt(111) substrate, while oxygen vacancies within the film are randomly distributed. At coverages between about 1 and 3 ML, we observe a quasi-(3 × 3) LEED pattern that is consistent with double diffraction from an 11 × 11 coincidence lattice that forms between the hexagonal Sm₂O₃(111) and Pt(111) lattices. The observation of a hexagonal Sm₂O₃(111) structure suggests that a relatively strong interaction with the Pt(111) surface forces the Sm₂O₃ thin film to adopt the defective fluorite structure rather than the preferred bixbyite structure of bulk Sm₂O₃. STM measurements further reveal that the

Sm₂O₃(111) film grows by a mechanism that is analogous to the Stranski-Krastanov mechanism in that a single wetting layer forms followed by the growth of well-defined, multilayer islands. Although island thickening occurs after completion of the wetting layer, the Sm₂O₃(111) films are high quality and characterized by large, atomically flat domains.

We also investigated the partial reduction and reoxidation of Sm₂O₃(111) thin films on Pt(111). Our results suggest that annealing the ~1–2 ML films at 1000 K in UHV causes a fraction of the wetting layer to decompose to SmO(100) while Sm₂O₃(111) in the third layer concurrently migrates into the second layer. The result is a film that consists of a nearly contiguous Sm₂O₃(111) second layer, and a first layer mixture of Sm₂O₃(111) and SmO(100) domains where the latter is evident as cracks in the second layer. LEED patterns obtained from the partially reduced films exhibit satellite spots that adopt a hexagonal arrangement centered on the main-order Sm₂O₃(111) spots. We show that the SmO(100) and Sm₂O₃(111) lattices can form a coincidence structure with minimal strain, and that the satellite features observed with LEED are consistent with the proposed Sm₂O₃(111)/SmO(100) coincidence structure as well as separate, coexisting domains of Sm₂O₃(111) and SmO(100). Lastly, we find that oxidation of the partially reduced films restores the Sm₂O₃(111) crystal structure, and significantly improves the film flatness and connectivity among oxide domains. Overall, our results demonstrate that high quality Sm₂O₃(111) thin films can be grown on Pt(111), and that the morphology and Sm oxidation states within the films can be modified by partial reduction and reoxidation. Our results further suggest that the formation of well-ordered domains of (100)-oriented monoxide may be a general characteristic in the reduction of rare earth oxide thin films on hexagonally close-packed metal surfaces. This possibility is intriguing since the ability to prepare well-defined layers of monoxide and higher oxides of the rare earth metals could provide new opportunities for investigating the surface chemistry of this class of materials and clarifying how the surface oxidation states that exist influence selectivity toward partial vs complete oxidation chemistry.

AUTHOR INFORMATION

Corresponding Authors

*E-mail: weaver@che.ufl.edu. Tel: 352-392-0869. Fax: 352-392-9513.

*E-mail: aschaefer@uni-bremen.de. Tel: +49-421-218-63175. Fax: +49-421-218-63188.

Notes

The authors declare no competing financial interest.

ACKNOWLEDGMENTS

We thank Suhrita Mukherjee and Andrew Auld for assistance with experiments. We also gratefully acknowledge financial support for this work provided by the National Science Foundation, Division of Chemistry through grant number 1026712. Finally, we are grateful to the Deutsche Forschungsgemeinschaft (DFG) for financial support through grant number BA-1710/19-1.

REFERENCES

- (1) Rosynek, M. P. Catalytic Properties of Rare Earth Oxides. *Catal. Rev.: Sci. Eng.* **1977**, *16*, 111–154.
- (2) Trovarelli, A. *Catalysis by Ceria and Related Materials*; Imperial College Press: London, 2002.

- (3) Antoshin, G. V.; Minachev, K. M.; Dmitriev, R. V. Mobility of Oxygen and Catalytic Properties of Rare Earth Oxides with Respect to Oxidation of Hydrogen. *Russ. Chem. Bull.* **1967**, *16*, 1793–1795.
- (4) Adachi, G.; Imanaka, N. The Binary Rare Earth Oxides. *Chem. Rev.* **1998**, *98*, 1479–1514.
- (5) Doornkamp, C.; Ponc, V. The Universal Character of the Mars and Van Krevelen Mechanism. *J. Mol. Catal. A: Chem.* **2000**, *162*, 19–32.
- (6) Hussein, G. A. M. Rare Earth Metal Oxides: Formation, Characterization and Catalytic Activity - Thermoanalytical and Applied Pyrolysis Review. *J. Anal. Appl. Pyrolysis* **1996**, *37*, 111–149.
- (7) Dedov, A. G.; Loktev, A. S.; Moiseev, I. I.; Aboukais, A.; Lamonier, J. F.; Filimonov, I. N. Oxidative Coupling of Methane Catalyzed by Rare Earth Oxides: Unexpected Synergistic Effect of the Oxide Mixtures. *Appl. Catal., A* **2003**, *245*, 209–220.
- (8) Campbell, K. D.; Zhang, H.; Lunsford, J. H. Methane Activation by the Lanthanide Oxides. *J. Phys. Chem.* **1988**, *92*, 750–753.
- (9) Grinter, D. C.; Ithnin, R.; Pang, C. L.; Thornton, G. Defect Structure of Ultrathin Ceria Films on Pt(111): Atomic Views from Scanning Tunneling Microscopy. *J. Phys. Chem. C* **2010**, *114*, 17036–17041.
- (10) Staudt, T.; Lykhach, Y.; Hammer, L.; Schneider, M. A.; Matolin, V.; Libuda, J. A Route to Continuous Ultra-Thin Cerium Oxide Films on Cu(111). *Surf. Sci.* **2009**, *603*, 3382–3388.
- (11) Matolin, V.; Libra, J.; Matolinova, I.; Nehasil, V.; Sedlacek, L.; Sutara, F. Growth of Ultra-Thin Cerium Oxide Layers on Cu(111). *Appl. Surf. Sci.* **2007**, *254*, 153–155.
- (12) Schierbaum, K.-D. Ordered Ultra-Thin Cerium Oxide Overlayers on Pt(111) Single Crystal Surfaces Studied by LEED and XPS. *Surf. Sci.* **1998**, *399*, 29–38.
- (13) Alexandrou, M.; Nix, R. M. The Growth, Structure and Stability of Ceria Overlayers on Pd(111). *Surf. Sci.* **1994**, *321*, 47–57.
- (14) Mullins, D. R.; Radulovic, P. V.; Overbury, S. H. Ordered Cerium Oxide Thin Films Grown on Ru(0001) and Ni(111). *Surf. Sci.* **1999**, *429*, 186–198.
- (15) Berner, U.; Schierbaum, K.; Jones, G.; Wincott, P.; Haq, S.; Thornton, G. Ultrathin Ordered CeO₂ Overlayers on Pt(111): Interaction with NO₂, NO, H₂O, and CO. *Surf. Sci.* **2000**, *467*, 201–213.
- (16) Esch, F.; Fabris, S.; Zhou, L.; Montini, T.; Africh, C.; Fornasiero, P.; Comelli, G.; Rosei, R. Electron Localization Determines Defect Formation on Ceria Substrates. *Science* **2005**, *309*, 752–755.
- (17) Rodriguez, J. A.; Ma, S.; Liu, P.; Hrbek, J.; Evans, J.; Pérez, M. Activity of CeO_x and TiO_x Nanoparticles Grown on Au(111) in the Water-Gas Shift Reaction. *Science* **2007**, *318*, 1757–1760.
- (18) Suchorski, Y.; Wrobel, R.; Becker, S.; Weiss, H. CO Oxidation on a CeO_x/Pt(111) Inverse Model Catalyst Surface: Catalytic Promotion and Tuning of Kinetic Phase Diagrams. *J. Phys. Chem. C* **2008**, *112*, 20012–20017.
- (19) Lykhach, Y.; Johánek, V.; Aleksandrov, H. A.; Kozlov, S. M.; Happel, M.; Skála, T.; Petkov, P. S.; Tsud, N.; Vayssilov, G. N.; Prince, K. C.; et al. Water Chemistry on Model Ceria and Pt/Ceria Catalysts. *J. Phys. Chem. C* **2012**, *116*, 12103–12113.
- (20) Luches, P.; Pagliuca, F.; Valeri, S. Morphology, Stoichiometry, and Interface Structure of CeO₂ Ultrathin Films on Pt(111). *J. Phys. Chem. C* **2011**, *115*, 10718–10726.
- (21) Kaemena, B.; Senanayake, S. D.; Meyer, A.; Sadowski, J. T.; Falta, J.; Flege, J. I. Growth and Morphology of Ceria on Ruthenium (0001). *J. Phys. Chem. C* **2013**, *117*, 221–232.
- (22) Lu, J. L.; Gao, H. J.; Shaikhutdinov, S.; Freund, H. J. Morphology and Defect Structure of the CeO₂(111) Films Grown on Ru(0001) as Studied by Scanning Tunneling Microscopy. *Surf. Sci.* **2006**, *600*, 5004–5010.
- (23) Breinlich, C.; Essen, J. M.; Barletta, E.; Wandelt, K. Growth, Structure and Electronic Properties of Ultrathin Cerium Oxide Films Grown on Pt(111). *Thin Solid Films* **2011**, *519*, 3752–3755.
- (24) Eck, S.; Castellarin-Cudia, C.; Surnev, S.; Ramsey, M. G.; Netzer, F. P. Growth and Thermal Properties of Ultrathin Cerium Oxide Layers on Rh(111). *Surf. Sci.* **2002**, *520*, 173–185.
- (25) Tao, J. G.; Batzill, M. Ultrathin Y₂O₃(111) Films on Pt(111) Substrates. *Surf. Sci.* **2011**, *605*, 1826–1833.
- (26) Mullins, D. R. Adsorption of CO and C₂H₄ on Rh-loaded Thin-Film Dysprosium Oxide. *Surf. Sci.* **2006**, *600*, 2718–2725.
- (27) Zhao, X.; Ma, S.; Hrbek, J.; Rodriguez, J. A. Reaction of Water with Ce-Au(111) and CeO_x/Au(111) Surfaces: Photoemission and STM Studies. *Surf. Sci.* **2007**, *601*, 2445–2452.
- (28) Senanayake, S. D.; Stacchiola, D.; Evans, J.; Estrella, M.; Barrio, L.; Pérez, M.; Hrbek, J.; Rodriguez, J. A. Probing the Reaction Intermediates for the Water–Gas Shift over Inverse CeO_x/Au(111) Catalysts. *J. Catal.* **2010**, *271*, 392–400.
- (29) Yang, F.; Graciani, J. S.; Evans, J.; Liu, P.; Hrbek, J.; Sanz, J. F.; Rodriguez, J. A. CO Oxidation on Inverse CeO_x/Cu(111) Catalysts: High Catalytic Activity and Ceria-Promoted Dissociation of O₂. *J. Am. Chem. Soc.* **2011**, *133*, 3444–3451.
- (30) Senanayake, S. D.; Stacchiola, D.; Rodriguez, J. A. Unique Properties of Ceria Nanoparticles Supported on Metals: Novel Inverse Ceria/Copper Catalysts for CO Oxidation and the Water-Gas Shift Reaction. *Acc. Chem. Res.* **2013**, *46*, 1702–1711.
- (31) Crew, W. W.; Madix, R. J. A Variable-Temperature Scanning Tunneling Microscope for the Study of Surface-Reactions in Ultrahigh-Vacuum. *Rev. Sci. Instrum.* **1995**, *66*, 4552–4556.
- (32) Devarajan, S. P.; Hinojosa, J. A., Jr.; Weaver, J. F. STM Study of High-Coverage Structures of Atomic Oxygen on Pt(111): p(2 × 1) and Pt Oxide Chain Structures. *Surf. Sci.* **2008**, *602*, 3116–3124.
- (33) Guo, Q.; Zhao, Y.; Jiang, C.; Mao, W. L.; Wang, Z. Phase Transformation in Sm₂O₃ at High Pressure: In situ Synchrotron X-ray Diffraction Study and ab initio DFT Calculation. *Solid State Commun.* **2008**, *145*, 250–254.
- (34) Hawkins, J. M.; Weaver, J. F.; Asthagiri, A. Density Functional Theory Study of the Initial Oxidation of the Pt(111) Surface. *Phys. Rev. B* **2009**, *79* (12), 125434.
- (35) Nörenberg, H.; Briggs, G. A. D. Defect Formation on CeO₂(111) Surfaces after Annealing Studied by STM. *Surf. Sci.* **1999**, *424*, L352–L355.
- (36) Namai, Y.; Fukui, K.-i.; Iwasawa, Y. Atom-Resolved Noncontact Atomic Force Microscopic Observations of CeO₂(111) Surfaces with Different Oxidation States: Surface Structure and Behavior of Surface Oxygen Atoms. *J. Phys. Chem. B* **2003**, *107*, 11666–11673.
- (37) Ellinger, F. H.; Zachariasen, W. H. The Crystal Structure of Samarium Metal and of Samarium Monoxide. *J. Am. Chem. Soc.* **1953**, *75*, 5650–5652.
- (38) Palmberg, P. W.; Rhodin, T. N. Analysis of Low-Energy Electron-Diffraction Patterns from Simple Overlayer Surface Structures. II. *J. Chem. Phys.* **1968**, *49* (1), 147–155.
- (39) Leger, J. M.; Yacoubi, N.; Loriers, J. Synthesis of rare earth monoxides. *J. Solid State Chem.* **1981**, *36*, 261–270.
- (40) Baddeley, C. J.; Stephenson, A. W.; Hardacre, C.; Tikhov, M.; Lambert, R. M. Structural and Electronic Properties of Ce Overlayers and Low-Dimensional Pt-Ce Alloys on Pt(111). *Phys. Rev. B* **1997**, *56* (19), 12589–12598.
- (41) Essen, J. M.; Becker, C.; Wandelt, K. Pt_xCe_{1-x} Surface Alloys on Pt(111): Structure and Adsorption. *e-J. Surf. Sci. Nanotechnol.* **2009**, *7*, 421–428.
- (42) Hermann, K.; Van Hove, M. A. *LEEDpat: LEED pattern analyzer*, version 3.0: Fritz-Haber-Institut: Berlin, 2013.

CO and D₂O chemistry on continuous and discontinuous samaria thin films on Pt(111)

Jin-Hao Jhang, Simona Keil, Andreas Schaefer¹, Volkmar Zielasek², Marcus Bäumer

Institute of Applied and Physical Chemistry, University of Bremen, Leobener Str. UFT, D-28359 Bremen, Germany

Abstract

The chemistry of CO and D₂O, individually adsorbed or co-adsorbed, on epitaxial thin films of samaria on Pt(111) was studied by temperature programmed desorption spectroscopy (TPD). Continuous thin films as well as discontinuous films composed of samaria islands on bare Pt(111) were prepared. Their comparative study indicates that Sm₂O₃ islands provide lattice oxygen at their perimeter for CO oxidation on adjacent exposed Pt area where CO adsorption takes place. CO₂ production was observed only on as-prepared discontinuous films. While, in particular on thermally reduced samaria islands, TPD after D₂O adsorption revealed D₂ production which indicates a pathway for D₂O dissociation, no evidence for the water gas shift reaction of CO and residual OD species on the surface was found after co-adsorption of CO and D₂O. Instead, interaction between CO and OD species at the perimeter of islands on reduced discontinuous SmO_x thin films obviously promotes D₂ formation without yielding CO₂ as desorbing product.

¹) Present address: Division of Synchrotron Radiation Research, Lund University, Box 118, SE-221 00 Lund, Sweden

²) Corresponding author (E-Mail: zielasek@uni-bremen.de)

Keywords: water gas shift reaction, catalysis, rare earth oxides, samaria, platinum, TPD, H₂O, D₂O, CO

Introduction

The water-gas shift (WGS) reaction and its reverse counterpart have been considered as among the most relevant reactions in the fields of sustainable chemistry and energy conversion. Starting with only water and CO, the WGS generates two benefits, namely (1) CO oxidation and (2) H₂ production, and therefore is of interest when it comes to controlling toxic exhaust gas emissions or feeding fuel cells, respectively [1-3]. Current catalysts used in industry for the WGS reaction are iron-chromium-magnesium and zinc-aluminum-copper mixture oxides [1, 2, 4]. They require complex activation steps, and especially for the Zn-Al-Cu oxide catalyst, operation at low temperature (ca. 200 °C) is mandatory because of the tendency of copper to sinter [5, 6]. Therefore, scientists are looking for new catalytic systems with higher thermal stability and ease of use for the WGS reaction and have thereby focused on combinations of transition metals and oxides, such as, e.g, Pt/CeO_x, Au/CeO_x, or Pt/TiO_x [7-13].

Model studies of the WGS reaction in surface science have focused on understanding mechanisms of the reaction. Currently, two possible pathways of the WGS reaction involving oxide surfaces are being proposed, both leading to water dissociation and oxidation of the CO adsorbed on the transition metal [3, 14-17]. In the so-called redox mechanism, CO directly reduces the oxide catalyst upon formation of CO₂. Subsequently, the reduced oxide is reoxidized by water, resulting in H₂ formation. In the associative mechanism, CO is oxidized by surface OH groups that are formed by dissociative water adsorption on the oxide catalyst. In principle, the WGS reaction may follow both, the redox and the associative pathway on an oxide-metal catalyst. So far there are only few experimental hints as to how the nature of oxide-metal systems affects the efficiency of either of the WGS reaction mechanisms. Here, for instance, the basicity

and acidity of surface sites, the oxidation states of the oxide, oxygen mobility, and reactions at surface vacancies or, in particular, the oxide-metal interface on a catalyst may play major roles. For instance, Graciani and Sanz have described that a strong interaction between oxide nanoparticles and a metal substrate may induce formation of nano-mixed oxides at the oxide-metal substrate interface by sharing oxygen atoms which leads to reduction of the oxide and may enhance the catalytic reactivity of the oxide in the WGS reaction [13]. To gain more insight, systemic studies of the chemistry of CO and water, individually as well as in combination, on appropriate models for oxide-metal catalysts are essential.

In the series of rare earth oxides (REO), so far only ceria (CeO_x)-based catalysts have been studied intensively for the WGS reaction [18-23], and it is also ceria and ceria-metal systems, for which studies of the interaction of the reactants CO and water under ambient pressure and in ultrahigh vacuum condition are available [24-27]. Ceria as a reducible oxide is able to dissociate water and oxidize CO. Due to formation of highly stable intermediates on ceria which stop the reaction, however, ceria alone is not an active WGS catalyst. To destabilize the intermediates and complete the WGS reaction, ceria-metal systems are considered in which ceria is able to dissociate water and the metal is used for CO adsorption and producing less stable intermediates at the perimeter sites between ceria and the metal [13].

We could show in previous work [28, 29] that samaria thin films grown on Pt(111) can be thermally reduced in UHV and reoxidized in O_2 at elevated temperatures. Furthermore, by precisely controlling the film growth parameters, high-quality continuous as well as discontinuous epitaxial samaria (SmO_x) thin films can be prepared. Therefore, we consider the

samarium-Pt system as highly valuable to test concepts for metal-REO WGS catalysts. Studies of methanol chemistry on the SmO_x -Pt system [29] showed us that SmO_x as a basic oxide is capable of methanol dehydrogenation and oxidation. Also we found out that a discontinuous SmO_x thin film (oxide islands in the neighborhood of exposed Pt surface area) exhibits a higher reactivity than a continuous SmO_x thin film or a bare Pt(111) surface, indicating cooperative effects on the metal-oxide system. In the present temperature-programmed desorption spectroscopy (TPD) [30-32] study, we have investigated the reaction of CO and water (D_2O) individually as well as after co-adsorption on both continuous SmO_x thin films and SmO_x islands grown on Pt(111). We will demonstrate in the following how the samarium film status influences its chemical reactivity with regards to CO and water and present tests for the WGS reaction by co-adsorbing CO and water on the samarium-Pt system. While our model studies do not yet provide direct evidence for efficient WGS catalysis by the samarium-Pt(111) system, they reveal insight into an intriguing CO-OD interaction thereon.

Experimental section

All experiments were performed in an UHV system (base pressure $< 5 \times 10^{-10}$ mbar) which consists of two major chambers, one housing an ion sputter source (SPECS), an e-beam evaporator (Omicron EFM3), and a quadrupole mass spectrometer (QMS) (HIDEN Analytical) for TPD, the other equipped with a four-grid LEED system (OMICRON) as well as an X-ray source (OMICRON) and a hemispherical electron analyzer (Leybold E10) for x-ray photoelectron spectroscopy (XPS). A Pt single crystal in shape of a circular disk (9 mm diameter) cut and polished in (111) orientation (Surface Preparation Laboratory) was mounted on a molybdenum sample plate and utilized as a substrate for the deposition of samarium thin films in

the UHV system. For sample temperature measurements, a type-K thermocouple was spot-welded to the backside of the Pt crystal. The Pt(111) surface was cleaned by repeated cycles of Ar⁺ sputtering at an ion energy of 1 KeV in an argon background pressure ($p = 5 \times 10^{-5}$ mbar) at room temperature for 20 min and annealing in UHV at 1000 K for 15 min. Afterwards, the crystal was annealed in oxygen background pressure ($p = 5 \times 10^{-7}$ mbar) for 10 min at 1000 K in order to remove any carbon contaminations. We considered a surface clean when XPS (Al K α radiation) showed both, C and O 1s emission signals below the detection limits, corresponding to atomic ratios of C/Pt and O/Pt below 0.02.

Epitaxial samaria thin films were prepared on the Pt(111) substrate by reactive physical vapor deposition (RPVD) of samarium metal in oxygen background ($P = 5 \times 10^{-7}$ mbar). As reported in detail in our previous work [28, 29] the substrate temperature is kept at 600 K during deposition and, for annealing, subsequently increased to 1000 K for 10 min while maintaining the background oxygen pressure. In order to estimate the film thicknesses the attenuation of the Pt 4f_{7/2} peak intensity in XPS spectra was used, assuming an inelastic mean free path (IMFP) of 25.03 Å [33]. The IMFP value is based on considering a bulk c-type Sm₂O₃ film (density: 8.347 g/cm³) grown on Pt(111). In the following, one monolayer (ML) of Sm₂O₃(111) is defined as an O-Sm-O trilayer in the <111> direction of the c-Sm₂O₃(111) structure which corresponds to an average film thickness of 3.18 Å [34]. By depositing 1.3 ± 0.1 ML and 4.3 ± 0.1 ML SmO_x, respectively, a continuous Sm₂O₃ thin film and a discontinuous Sm₂O₃ thin film (oxide islands, leaving parts of Pt(111) area exposed) were prepared. For simplicity, the continuous and the discontinuous thin films are denoted “thin film” and “islands”, respectively, in the following.

TPD experiments were carried out after dosing Langmuir equivalents of CO (4.7 grade, Linde) or D₂O from a liquid reservoir via a gas doser onto the sample held at 96 K in a background pressure below 5×10^{-10} mbar. D₂O was chosen instead of H₂O because the latter is abundant in the background pressure even at UHV conditions and therefore causes relatively high background signals for H₂O and H₂ in the QMS. The liquid D₂O reservoir was purified by at least 10 freeze-pump-thaw cycles. In the present work, 5 Langmuir of CO and 10 Langmuir of D₂O were dosed onto the samples before each TPD. Only for calibrating the exposed Pt areas, we overdosed CO onto samples in order to safely achieve the saturation coverage of 0.68 monolayer equivalent (MLE) CO on Pt(111) [35]. One MLE is defined as the surface atomic density of Pt(111) being $1.52 \times 10^{15} \text{ cm}^{-2}$.

Each TPD experiment was carried out by warming up the sample from 100 K to 800 K with a well-controlled heating rate of 1 K/s (controller by Schlichting Physikalische Instrumente) in front of an aperture to the QMS which recorded seven masses ($m/z = 28$ (CO), 44 (CO₂), 20 (D₂O), 19 (DOH), 18 (OD and H₂O), 4 (D₂) and 3 (DH)). For data presentation in the following, the ionization probabilities of the particular molecules in the QMS have been accounted for by normalizing the recorded intensities. Calibration of the recorded TPD signal intensities in terms of product yields was performed by preparing, as reference, a coverage of 1/3 MLE CO on bare Pt(111) via monitoring the associated $(\sqrt{3} \times \sqrt{3})R30^\circ$ structure in LEED and then integrating the intensity of the corresponding CO signal during TPD [35]. Based on this calibration, 5 Langmuir of CO dosed on Pt(111) yielded a CO coverage of 0.40 ± 0.01 MLE. It should be noted that conversion of D₂O-TPD signal intensities to absolute yields is hindered by the background water and hydrogen pressure in the UHV system. They render an unambiguous ascription of related

masses to a single fragment difficult. For instance, $m/z = 18$ may represent OD as well as H_2O . Furthermore, H/D exchange reactions in the QMS need to be taken into account as well. In fact, since $m/z = 3$ (DH) as D_2 -related mass was detected in the QMS, both, D_2 - and DH-TPD signals were taken into account in order to estimate D_2 yields.

Results and Discussion

I. CO chemistry

First, results on CO adsorption and reaction on an as-prepared Sm_2O_3 thin film and on as-prepared Sm_2O_3 islands will be reported. The TPD data for $m/z=28$ (CO) and $m/z=44$ (CO_2) are compiled in comparison to those obtained from a bare Pt(111) surface in Figure 1. For the bare Pt(111) surface only a CO desorption peak at 400 K – 500 K is observed. If there was a high concentration of surface defects (or steps) on a Pt(111) substrate, an additional CO desorption peak should be visible at 570 K [36].

For the as-prepared Sm_2O_3 thin film (total coverage 4.3 ML), a sharp CO desorption peak is observed at 113 K. There is no CO desorption in the temperature range 400-500 K, indicating that the Pt(111) surface was in fact fully covered by the Sm_2O_3 thin film. Considering a first-order desorption of CO from the Sm_2O_3 surface with the frequency factor of $10^{13} s^{-1}$, we estimate the activation energy of desorption as $28.7 kJ mol^{-1}$ by using Redhead's equation [37]. In comparison, Kuriyama et al., e.g. observed similarly weak adsorption and quick desorption of CO from SmO_x films grown on a Ru(0001) substrate (they found a desorption temperature of 125 K) [38].

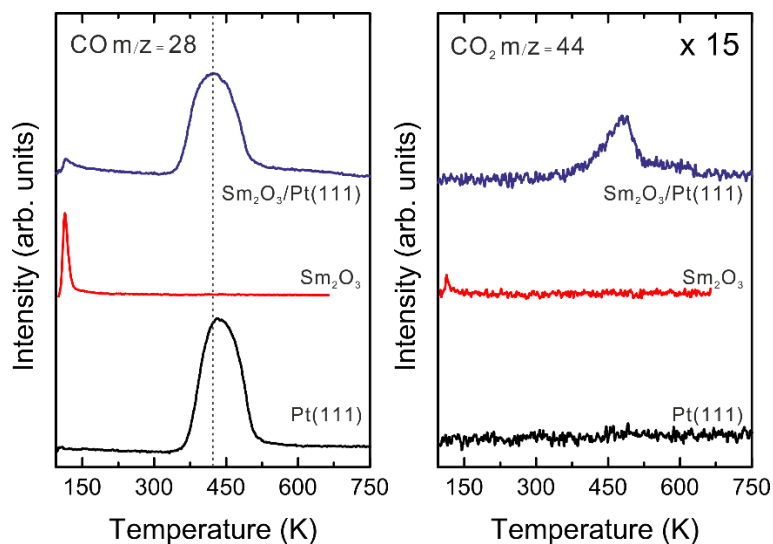


Figure 1: CO- and CO₂-TPD spectra collected from a clean Pt(111) surface, an as-prepared Sm₂O₃ thin film, and as-prepared Sm₂O₃ islands, respectively, after dosing 5 L CO at 96 K.

The CO-TPD spectrum from the as-prepared Sm₂O₃ islands (1.3 ML) on Pt(111) shows both desorption features from both, Pt(111) and the Sm₂O₃ thin film. The CO desorption peak contributed by exposed Pt areas exhibits a somewhat lower maximum desorption temperature (420 K) and is broader compared to the bare Pt(111) surface. Kuriyama et al. [39] observed a similar behavior of the major CO-TPD feature when a Ru(0001) surface was covered by SmO_x islands. It should be mentioned that only at low coverage of SmO_x on Ru(0001) (below 0.31 ML) they observed an additional CO desorption peak at 350 K which was assigned to CO desorption from perimeter sites between SmO_x islands and the Ru surface where, as the authors speculated, excess oxygen may exist which repels neighboring CO molecules. Since we did not observe any additional CO peak in the CO-TPD spectrum from the (1.3 ML) Sm₂O₃ islands on Pt(111), there is no evidence for excess oxygen on Sm₂O₃ perimeter sites in our case.

Estimating the activation energy for CO desorption from Sm₂O₃ islands on Pt(111) by

considering first-order desorption and a frequency factor of 10^{13} s^{-1} , we obtain a value of $111.28 \text{ kJ mol}^{-1}$ which is $\sim 4.1 \text{ kJ mol}^{-1}$ lower than for the bare Pt(111) surface. This decrease of the CO desorption activation barrier indicates that the mean distance between adjacent CO molecules has decreased and, thereby, enhanced the effects of the long-range repulsive CO-CO interaction. By integrating the CO peak areas from bare Pt(111) and the as-prepared Sm_2O_3 islands, respectively, we find for both samples a CO desorption of 0.40 MLE, in total. For the bare Pt(111) surface this coverage is below saturation which has been reported as 0.68 MLE at 100 K [35]. As will be demonstrated below, the Sm_2O_3 islands cover 35% of the Pt(111) surface area. Therefore the similar amount of CO desorbing from both samples is surprising and indicates a CO spillover from Sm_2O_3 surface to exposed Pt areas. The concomitant decrease of the mean distance between CO molecules may explain the decrease of the activation barrier for CO desorption from the Sm_2O_3 islands compared to bare Pt(111) observed in the TPD experiments.

In contrast to bare Pt(111) and to the as-prepared continuous Sm_2O_3 film, a small CO_2 desorption peak (0.014 MLE) at 485 K is observed for the as-prepared Sm_2O_3 islands. Observing CO_2 desorption at that temperature range at which CO desorbs from Pt(111) implies that CO oxidation most likely takes place at the perimeter sites between Sm_2O_3 islands and exposed Pt areas. There, Sm_2O_3 can provide the oxygen required to produce CO_2 from CO adsorbed at Pt sites. As mentioned above, there is no evidence for excess oxygen at perimeter sites between Sm_2O_3 islands and Pt. Therefore, we rule out any contribution of excess oxygen to CO oxidation and conceive (1) the redox mechanism ($\text{CO} + \text{O}_{\text{lattice}} \rightarrow \text{CO}_2$) and (2) the associative mechanism ($\text{CO} + \text{OH}_{\text{ad}} \rightarrow \text{CO}_2 + \frac{1}{2} \text{H}_2$), as discussed in the introduction, as the two possible CO oxidation

pathways on the sample surface [22, 40, 41]. The formation of hydroxyls on REO surfaces during thin film preparation or any sample cooling procedures in UHV has been demonstrated by XPS [42, 43] and, therefore, reaction (2) is also considered in our case. However, our TPD monitoring shows that there is no H₂ production (m/z = 2) as would be expected concomitantly with the CO₂ evolution from reaction (2). Accordingly, we conclude that it is reaction (1) and the lattice oxygen of Sm₂O₃ on perimeter sites of the islands which contribute mainly to CO oxidation.

Consequently, the amount of lattice oxygen available for CO₂ formation should decrease during a CO-TPD experiment. As a test to this hypothesis, repeated CO-TPD experiments were performed on an as-prepared sample of Sm₂O₃ islands on Pt(111). The results, shown in Figure 2, reveal a clear maximum yield of CO₂ in the 1st CO-TPD experiment whereas the relative yield of CO₂ continuously decreases over repeated CO TPD experiments. As mentioned above, only 0.014 MLE of CO₂ is detected in the 1st TPD, indicating that only a similarly small amount of lattice oxygen is available for CO oxidation. To demonstrate that it is indeed the lattice oxygen which plays a major role for CO oxidation, we performed CO TPD experiments also on samples of Sm₂O₃ islands which were thermally reduced by annealing at 1000 K for 30 min [28] and found no CO₂ evolution at all (data not shown). Obviously, only the as-prepared Sm₂O₃ islands are able to provide lattice oxygen available for CO oxidation, which is essential for the redox pathway of the WGS reaction. As demonstrated by the absence of CO₂ production on a Sm₂O₃ film and the spill-over of CO to Pt(111) areas and as indicated by the low yield of the CO₂ from Sm₂O₃ islands it is probably only a small amount of lattice oxygen from island perimeter sites which contribute to CO oxidation.

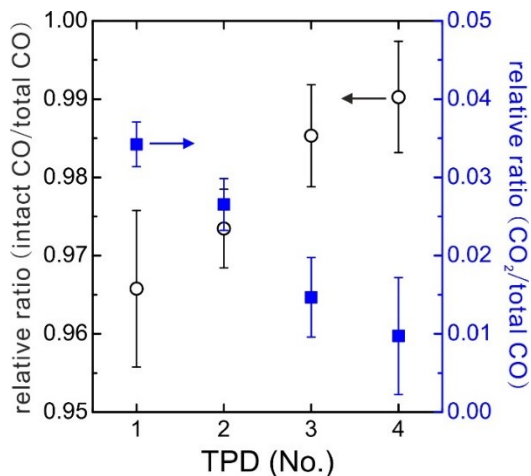


Figure 2: CO_2 and intact CO yields collected from the as-prepared Sm_2O_3 islands over repeated CO TPD runs normalized to total CO_x desorption.

II. D_2O chemistry

a) As-prepared continuous and discontinuous Sm_2O_3 thin films on Pt(111)

All D_2O -related masses ($m/z = 20$ (D_2O), 19 (DOH), and 18 (OD and H_2O)) were recorded, as mentioned in the experimental section) showed similar features in TPD spectra in the case of the as-prepared Sm_2O_3 thin film and the as-prepared Sm_2O_3 islands. Also, compared to each other, both recorded D_2 -related masses ($m/z = 4$ (D_2) and 3 (DH)) exhibited the same behavior. Therefore, in the following only the main D_2O and D_2 masses ($m/z = 20$ and 4 , respectively) are shown in the figures. Hydrogen present in the detected products suggests either H_2O contamination of the D_2O reservoir or isotope exchange reactions of desorbing products at the chamber wall and/or in the QMS ion source [44]. Studying isotope effects in water desorption from Ru(0001), Denzler et al. found that in case of a H_2O and/or H_2 contamination in a D_2O sample an additional D_2O desorption peak at ~ 210 K should be observed, indicative of a relatively strong bond between D_2O and $\text{H}_2\text{O}/\text{H}_2$ which stabilizes adsorbed D_2O molecules [45]. Since there is no additional D_2O peak observed at ~ 210 K in our experiments, we rule out a H_2O

and/or H₂ contamination in the D₂O reservoir. The hydrogen present in the observed products must be mainly originating from isotope exchange reactions in the QMS.

D₂O-TPD from bare Pt(111) yields a D₂O peak at 190 K, which can be assigned to bilayer (BL) D₂O desorption [46, 47], and a tiny D₂ peak (< 0.01 MLE) at ~ 400 K (see Figure 3). The shape of the D₂O peak reveals a typical zero-order desorption indicating that the bilayer D₂O does not react with the Pt(111) surface. As also reported by others, water does not dissociate on a flat or stepped Pt(111) surface.[46, 48] Therefore, we ascribe the small amount of D₂ desorption to D₂O dissociation most likely at defects on the Pt substrate.

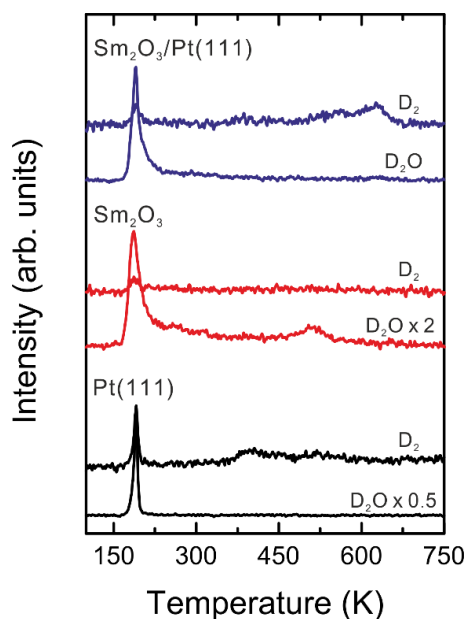


Figure 3: D₂O- and D₂-TPD spectra collected from the Pt(111), the as-prepared Sm₂O₃ thin film, and the as-prepared Sm₂O₃ islands.

Compared to Pt(111), the D₂O-TPD spectra from both, the thin Sm₂O₃ film and the Sm₂O₃ islands show a broader peak at 190 K accompanied by a tail up to ca. 250 K – 300 K. The tail must be assigned to D₂O recombination on Sm₂O₃ because it is not observed on the clean Pt(111) surface. It suggests that the Sm₂O₃ surface is able to dissociate D₂O below 190 K. Given

the D₂O dissociation products OD (nucleophilic) and D (electrophilic) and their nature on oxide surfaces [49-51], it is expected that OD binds to Sm cation sites or surface vacancies whereas D adsorbs at O anion sites. To the best of our knowledge, so far no water-TPD experiments on samaria surfaces have been reported. However, similar findings were observed on other oxide surfaces. For instance, Mullins et al. have used XPS to show that water from hydroxyl recombination desorbs from an oxidized CeO₂(111) surface between 200 K and 300 K [53, 54].

It should be noted that, in general, bilayer water structures are not observed on surfaces on which the interaction between water with the surface is stronger than the interaction between water molecules. Because of the interaction between the first water layer and the surface, the first water layer does not provide a suitable template for the formation of the bilayer water structure. Often, oxide surfaces represent this class of surfaces. In contrast, bilayer water structures are often observed on non-reactive metal surfaces such as, e.g., Pt(111), Pd(111), Ru(0001), or Au(111) [52]. Since D₂O is able to dissociate on samaria surfaces, one may expect that the first D₂O layer is unlikely to be a template for the bilayer structure. Thus, we assign the D₂O peak observed at 190 K for both, the continuous as-prepared Sm₂O₃ thin film and the as-prepared Sm₂O₃ islands on Pt(111) simply to non-recombinative molecular D₂O desorption.

Above 300 K, the Sm₂O₃ thin film and the Sm₂O₃ islands vary with respect to the D₂O chemistry thereon. We observed an additional D₂O recombination peak at 520 K from the thin film, whereas no D₂O recombination but a small D₂ peak (ca. 0.013 ± 0.005 MLE) at 600 K was observed for the islands. The D₂O recombination peak from the thin film with a peak onset at 450 K is clear evidence that D₂O can be dissociated to OD and D on the film and that these

species must be stable up to ca. 450 K. Since the desorption temperature (peak maximum at 480 K) of recombinative D₂O from the thin film is lower than the D₂ desorption temperature (600 K) from the islands, there is obviously even stronger binding of OD and D species to the Sm₂O₃ islands, blocking the route of D₂O recombination and resulting in D₂ formation at higher temperature. The high desorption temperature of D₂ also implies an remarkable stability of surface OD species. The different reactive nature of the Sm₂O₃ film and Sm₂O₃ islands may be due to electronic effects induced by the Pt substrate or vacancy or defect sites on the Sm₂O₃ islands which, compared to the continuous film (4.3 ML coverage) are relatively thin (1.3 ML total coverage).

b) Reduced continuous and discontinuous SmO_x thin films/Pt(111)

To complete the WGS reaction via the redox mechanism, reoxidation of a reduced oxide surface by water is required. In the associative mechanism, although the reduction/oxidation reaction of an oxide surface is not directly involved in the WGS reaction, the oxidation condition of the oxide surface may affect its activity for WGS by promoting or limiting water dissociation. In a previous study [29] we demonstrated that thermal reduction of epitaxial Sm₂O₃ thin films leads to significant changes of chemical reactivity and behavior. In the present work we focused on how the D₂O chemistry responds to different SmO_x oxidation conditions and performed D₂O TPD experiments on both, reduced SmO_x thin films and reduced SmO_x islands. In particular, the possibility of SmO_x reoxidation by D₂O, as required for WGS, was investigated. The TPD results are compiled in Figure 4.

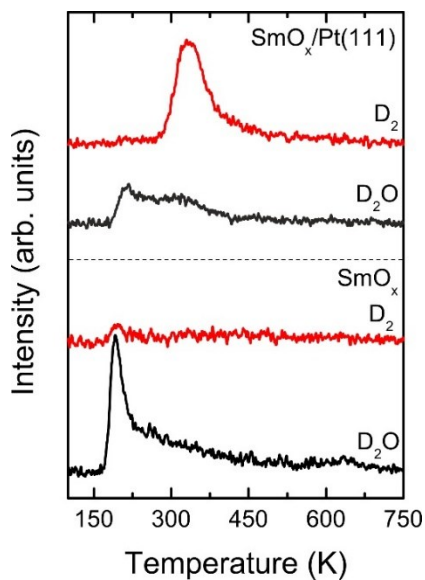


Figure 4: D_2O - and D_2 -TPD spectra collected from the reduced SmO_x thin film and the reduced SmO_x islands.

For reduced SmO_x thin films, a D_2O desorption peak at 190 K was observed, just as for the as-prepared Sm_2O_3 thin film. The tail of this D_2O desorption peak is somewhat more pronounced and reaches higher temperature (ca. 450 K) compared to the as-prepared film while the high-temperature D_2O recombination peak shifts to higher temperature at around 650 K. Integrating the tail areas in D_2O -TPD spectra collected from the as-prepared and reduced thin film, respectively, yields 1.8 times more recombinative D_2O desorbing from the reduced thin film. From our previous study [29] and other studies on reduced metal oxides [55-57], it is known that thermal reduction generates vacancies on metal oxide surfaces. Studies of water adsorption and dissociation on CeO_x and TiO_x surfaces have revealed that surface vacancies on reduced oxide surfaces promote the dissociation of water and stabilize OH and H species [53, 54, 58-60]. In accordance, our TPD data demonstrate that more D_2O molecules do dissociate on the reduced surface and that the products (OD and D) bind stronger to the reduced surface than to the as-

prepared (and fully oxidized) surface.

The D₂O-TPD spectra from the reduced SmO_x islands show significant differences compared to those from the as-prepared islands. The main D₂O desorption peak shifted from 190 K (as-prepared islands) to 206 K, suggesting an increase of the D₂O-SmO_x interaction not observed for the reduced SmO_x thin film. Furthermore, a broad D₂O desorption feature was observed between 250 K and 400 K. By integrating the tail areas of the TPD peaks for the as-prepared and the reduced samples of SmO_x islands, we found that 4.5 times more D₂O molecules are produced by recombination on the reduced islands. For comparison, thermal reduction of the continuous SmO_x film led to an increase of recombinative D₂O desorption by a factor of only 1.8, as discussed before, suggesting that thermal reduction affects the islands more profoundly than the thin film. In fact, in a previous STM study, we found the response of samaria thin films to thermal reduction being strongly dependent on the SmO_x film thickness. At total coverages below 3 ML, thermal reduction causes significant geometric reordering and electronic changes in the film due to the formation of SmO(100) domains [28] on the Pt(111) substrate which may lead to the observed increase of the D₂O-SmO_x interaction on reduced SmO_x islands (1.3 ML coverage).

In contrast to the as-prepared islands, the reduced islands also showed pronounced D₂ production detected as a TPD peak at 325 K which is close to the desorption temperature of molecular hydrogen from a bare Pt(111) surface. [61, 62] Probably, D from D₂O dissociation on the reduced SmO_x surface diffuses to the exposed Pt areas wherefrom it then desorbs as D₂. Obviously, this pathway is hindered on as-prepared Sm₂O₃ islands. The clear D₂ desorption peak

observed for the reduced SmO_x islands indicates that OD or O must remain on the reduced surface as residual products of water dissociation. The amount of D_2 produced is 0.05 (± 0.005) MLE. If we consider only the reaction of $\text{D}_2\text{O} \rightarrow \text{D}_2 + \text{O}$, then there must be 0.05 MLE of oxygen atoms staying on the reduced surface, if we consider only $2 \text{D}_2\text{O} \rightarrow \text{D}_2 + 2 \text{OD}$ then there must be 0.10 MLE of OD species on the surface. Thus, repeated D_2O TPD experiments were carried out on the reduced surface to learn if the D_2O reaction affects the surface chemistry and, in particular, contributes to reoxidation of the SmO_x islands. As shown in Figure 5, repeated D_2O TPD runs on the reduced SmO_x islands reveal a clear maximum of the D_2 peak intensity during the 1st TPD, whereas from the second TPD on, the diminished D_2O -TPD feature does not change significantly. Obviously, the reduced SmO_x surface is significantly altered by residual oxygen and/or OD species on the surface stemming from the initial TPD and reaches a somehow saturated condition which results in less D_2 formation.

Intriguingly, the D_2O desorption behavior from the reduced surface is not affected over repeated TPD experiments as the left panel of Fig. 5 shows. This observation indicates that the SmO_x surface is not fully oxidized back to its as-prepared condition during the first TPD run. One may argue that the surface could be thermally reduced during each TPD experiment by heating up to 800 K and, therefore, our experiments do not show complete reoxidation. However, if the surface was reduced in each TPD experiment, there should be no significant decrease of the D_2 production after the 1st TPD, in contrast to our experimental observation.

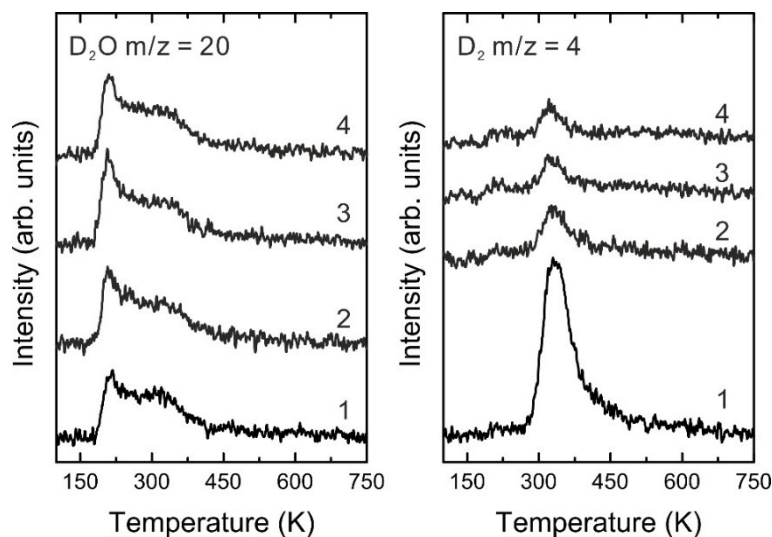


Figure 5: D₂O- and D₂-TPD spectra collected from the reduced SmO_x islands treated over repeated D₂O TPD experiments.

In summary, our studies of water chemistry on SmO_x films and islands show that some of the adsorbed D₂O dissociated at samaria sites and produced oxygen or OD and D species on these surfaces. Especially on a reduced SmO_x surface, D₂O dissociation is promoted and OD species are obviously stabilized up to higher temperature. On reduced SmO_x islands, D species (generated by D₂O dissociation) spill over to the exposed Pt areas while the residual OD and/or oxygen species from D₂O dissociation remain on the reduced SmO_x surface. Hence, at this stage, we have learned that in particular samples which exhibit samaria islands and exposed Pt surface area in the neighborhood show some potential for driving the WGS reaction which requires hydroxyl formation for the associative mechanism or reoxidation of the catalyst surface in the redox mechanism. With respect to the latter pathway, however, our experiments suggest that dissociative adsorption of D₂O on reduced SmO_x islands does not restore the film to its as-prepared, fully oxidized state.

A clear indication of SmO_x oxidation or reduction is wetting or dewetting of SmO_x islands on Pt(111), as shown by our previous STM work [28]. Concomitantly with $\text{SmO}(100)$ formation, the reduction process leads to SmO_x islands spreading on the Pt substrate surface. Vice versa, oxidation leads to SmO_x dewetting. Therefore, monitoring wetting and dewetting by estimating the exposed Pt(111) area from the absolute amount of CO adsorbed at saturation can be taken as an indication for reduction and oxidation. For that purpose, a saturated amount (32 L) of CO was dosed on the bare Pt(111), the as-prepared samaria islands on Pt(111), the same sample after thermal reduction, and the reduced sample after 4 cycles of D_2O -TPD experiments, respectively. In a subsequent TPD experiment, the amount of desorbed CO was quantified. The total Pt(111) area deduced therefrom (assuming the saturation coverage of 0.68 MLE on Pt(111)) is shown in Figure 6 (a).

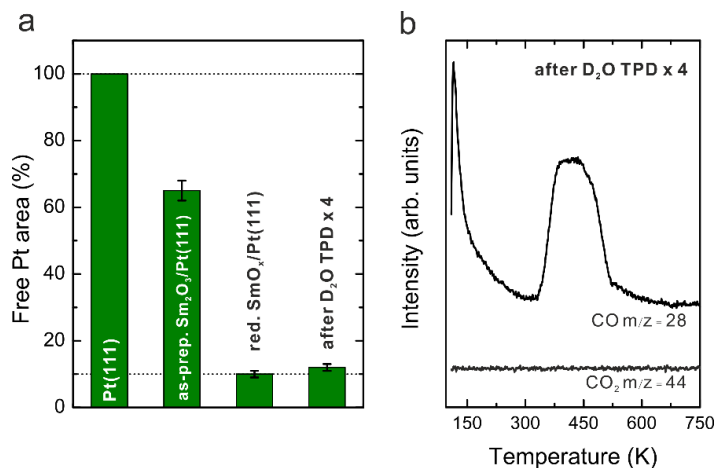


Figure 6: (a) Free Pt areas (%) estimated from different samples, and (b) CO and CO_2 TPD spectra collected by dosing 32 L CO on the reduced SmO_x islands after repeated D_2O -TPD experiments.

65 (\pm 3) % of the total Pt substrate surface area are exposed on the sample with the as-

prepared Sm_2O_3 islands. After thermal reduction (1000 K for 30 min in UHV), the free Pt area decreases to merely 10 (± 1) %, indicating that the SmO_x film spreads onto the Pt(111) surface. Moreover, given that reduced SmO_x islands cover ca. 90 % of the Pt(111) surface, it is reasonable to assume that the D_2O -TPD peak (observed in Figure 5) desorbs mainly from the reduced SmO_x surface. The free Pt area slightly increases by 2 (± 1) % on the sample after 4 runs of D_2O TPD experiments were performed which suggests that only minor dewetting of the SmO_x film takes place and confirms that D_2O does not show a pronounced capability of reoxidizing reduced SmO_x .

Still, as pointed out before, some OD or O species produced from D_2O dissociation must remain on the reduced SmO_x surface after repeated D_2O TPD runs. We probed their reactivity in terms of WGS by adsorbing a saturated amount (32 L) of CO on the surface. A subsequent TPD (results are compiled in Figure 6 (b)) showed no CO_2 evolution, i.e., neither of the two CO oxidation pathways (redox reaction and associative reaction) does work in this case. As mentioned before, the CO oxidation is expected to take place on the perimeter sites between samaria islands and exposed Pt areas. Obviously, in contrast to an as-prepared sample the perimeter sites of the reduced islands cannot provide oxygen available for CO oxidation, even after exposure to D_2O . Although some OD and/or O species must have built up on the SmO_x surface due to D_2O dissociation, they are not reactive towards CO oxidation.

III. Co-adsorption of CO and D_2O on discontinuous SmO_x thin films on Pt(111)

So far, we have learned that CO mainly adsorbs on Pt surface sites and, above room temperature, can be oxidized to CO_2 by reacting with lattice oxygen on perimeter sites of as-prepared Sm_2O_3

islands. D₂O, on the other side, mainly dissociates on samaria surface sites and probably forms OD species thereon. D₂O dissociation is promoted on reduced SmO_x surfaces, especially on the reduced SmO_x islands. Although our model studies in UHV do not directly show efficient WGS turnover for the SmO_x-Pt(111) system, it may still be of interest for tests at elevated pressures and temperatures at which WGS catalysts are usually operated. In this respect, any insight into the interaction of CO and OD species which, intriguingly, even above room temperature stably reside on the SmO_x-Pt(111) system, may be relevant. Therefore, we reversed the exposure of samaria islands to water and CO, i.e., we first dosed CO and then exposed the surface to D₂O. In detail, 5 Langmuir of CO were pre-dosed on samples of as-prepared and of reduced Sm₂O₃ islands at 96 K and afterwards the samples were heated up to 200 K in order to remove molecular CO from the samaria islands but not from bare Pt areas. Then the samples were cooled down again to 96 K, exposed to 10 Langmuir of D₂O (molecular D₂O adsorbs on both, samaria islands and the CO-covered Pt surface) and subsequently a TPD experiment was performed.

The results are compiled in Figure 7, where, for easy comparison of all TPD features, the intensity of the CO-TPD spectrum collected from the as-prepared Sm₂O₃ islands is divided by a factor of 10. For the as-prepared Sm₂O₃ islands, CO desorption from the surface covered by CO and D₂O showed a similar behavior as after only CO was adsorbed. Also CO₂ production was observed and the TPD feature and the estimated CO₂ yield were similar to the results obtained after exposing the surface only to CO. Apparently, D₂O as co-adsorbate on the sample does not influence the behavior of CO desorption and reaction. In contrast, the D₂O and D₂ TPD signals showed slight differences compared to those of pure D₂O adsorption on the as-prepared Sm₂O₃ islands. In comparison, the D₂O TPD peak shifted down by 15 K (from 190 K to 175 K),

indicating destabilization of the attractive D_2O - D_2O interaction, probably due to repulsive D_2O -CO interaction. A similar decrease of the D_2O desorption barrier was reported for a CO-covered Pt(111) surface [63]. Because CO only adsorbs on Pt areas, the observed downshift of the D_2O TPD peak implies that non-dissociative D_2O desorption (at 175 K) is mainly contributed from exposed Pt areas covered by CO, perhaps also from the perimeter sites between Sm_2O_3 islands and Pt but not from the Sm_2O_3 islands. A D_2O desorption due to recombination after dissociative D_2O adsorption on Sm_2O_3 islands is visible as a tail in the TPD spectrum in the temperature range up to 250 K. The lack of D_2 desorption shows that the CO_2 evolution is not due to the WGS reaction ($CO + D_2O \rightarrow CO_2 + D_2$) of the co-adsorbed CO and D_2O species on the as-prepared Sm_2O_3 islands. Thus, surface OD species on the Sm_2O_3 surface are not efficient to oxidize CO and CO can only be oxidized by oxygen from the SmO_x lattice, as reported in section II.a.

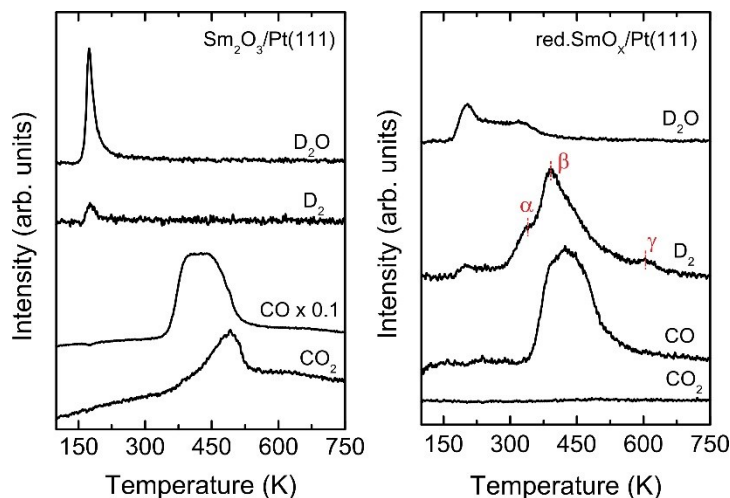


Figure 7: TPD spectra collected from the as-prepared and the reduced SmO_x islands with 5 L pre-dosed CO and 10 L D_2O .

TPD after co-adsorption of CO and D₂O on reduced SmO_x islands (right panel of Fig. 7) showed a much smaller CO coverage than from the as-prepared island, as expected due to wetting of the Pt(111) surface by SmO_x islands during thermal reduction. No CO₂ formation was observed on the reduced surface, implying that there is no oxygen on the perimeter sites available for CO oxidation. Similar to observations after dosing only D₂O, the D₂O-TPD signal collected from the reduced SmO_x islands suggests promotion of D₂O dissociation and higher stability of OD (and D) surface species when compared to the as-prepared islands also after co-adsorption of CO and D₂O. Intriguingly, in contrast to the as-prepared SmO_x islands, however, the reduced SmO_x islands show a pronounced D₂-TPD signal (0.15 MLE) in a broad temperature range between 300 K and 650 K. We identify three contributions denoted α , β , γ in the following which form this broad D₂ signal. The peak α was also observed in the case of individual D₂O reaction on reduced SmO_x islands. We assigned it to D₂ desorption from exposed Pt areas after D spillover from the SmO_x islands to Pt areas. The intensity of the peak α , however, turned out smaller by a factor of ca. 2 when CO was pre-dosed. Probably, parts of the Pt surface sites are blocked by CO, leading to a reduced spillover of D from SmO_x and, consequently, reduced D₂ desorption from the Pt surface.

The broad D₂ desorption features labeled β and γ were not observed in the case of individual D₂O reaction without pre-dosed CO. They appear in the same temperature region as CO desorption from Pt and the total yield estimated from β and γ corresponds to 0.125 MLE D₂. This considerable amount of D₂ detected only after pre-dosing CO suggests that CO on the exposed Pt areas near the perimeter sites to the SmO_x islands assists the decomposition of OD on the SmO_x islands. We have concluded from D₂O TPD experiments that OD is more stable on a

reduced SmO_x surface than on an oxidized surface which indicates that oxygen of hydroxyls binds on the reduced surface stronger than on the as-prepared one. Theoretical work on CeO_x surfaces by Marrocchelli and Yildiz reasoned that there is a local accumulation of positive charge in the neighborhood of surface vacancies which leads to an increased Coulombic interaction between the O of hydroxyl and the surface vacancies [64]. Accordingly, we speculate that the O-D bond is weaker on the reduced SmO_x islands surface due to vacancies. Alternatively, one may conceive that CO and surface OD species react and produce formate as an intermediate species on the surface which further decompose to CO and D_2 as products, and, again, leave oxygen on the reduced surface ($\text{CO} + \text{OD} \rightarrow \text{DOC O} \rightarrow 1/2 \text{D}_2 + \text{CO} + \text{O}$). Decomposition of formate species to CO has been discussed in certain reactions, such as, e.g., the reverse WGS reaction [65, 66] and methanol decomposition [67].

Repeated CO / D_2O TPD experiments revealed that, while the D_2O -TPD feature does not change significantly over the repeated TPD runs (Figure 8 a), the intensity of the D_2 -TPD peak drops dramatically after the 1st TPD run. CO and CO_2 -TPD spectra which were also recorded (data not shown) showed no significant changes during repeated TPD experiments. In particular, no CO_2 evolution was observed, implying that the WGS reaction does not take place under the conditions of our TPD experiments. For comparison, the yields of D_2 estimated from the D_2O -TPD experiments on the reduced SmO_x islands with and without pre-dosed CO on exposed Pt areas are shown in Figure 8 (b). In the 1st TPD run, the yield of D_2 from the experiment with pre-dosed CO is a factor of 3 larger than for the experiment without pre-dosed CO. It then drops by a larger factor from 1st and 2nd TPD experiment as compared to the experiments without pre-dosed CO which suggests that the assistance of CO for D_2 formation during the 1st TPD is essential.

After the 1st TPD run, a relatively small D₂ signal between 450 K and 650 K is observed, and the yield of D₂ decreases by a factor of 4. Possibly, the reduced SmO_x surface is reoxidized by oxygen left over from the OD dissociation or reaction, most likely at perimeter sites between SmO_x islands and exposed Pt areas. This process may refill surface vacancies there and thereby reduce the rate of D₂O dissociation. As a result, probably also the interaction of CO and OD species is limited and therefore less D₂ formation was detected in subsequent TPD runs.

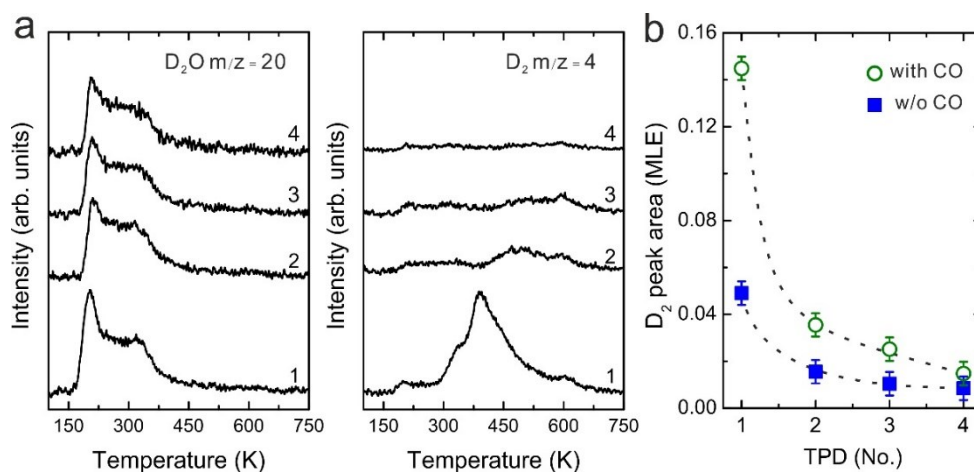


Figure 8: (a) D₂O- and D₂-TPD spectra collected from the reduced SmO_x islands with repeated TPD experiments by preparing 5 L pre-dosed CO and 10 L D₂O. (b) The D₂ yields estimated from the D₂O reaction on the reduced SmO_x islands with and w/o pre-dosed CO.

Unlike the production of D₂, the D₂O-TPD signal features do not change significantly over repeated TPD experiments. We therefore assume that, in contrast to D₂ production, D₂O desorption is mainly contributed by surface sites of the reduced SmO_x islands and not by their perimeters. The indifference of the D₂O-TPD feature with respect to repeated TPD experiments implies that the chemical behavior of the reduced surface of the islands is not affected. Based on the TPD results, we conclude that the interaction of CO and OD species at the island perimeters produces D₂ and thereby leaves O on the surface to reoxidize perimeter sites but not surface sites

of the SmO_x islands. The existence of the perimeter sites therefore seems important for driving the interaction of CO and OD species.

Conclusions

TPD experiments were performed to elucidate the chemistry of CO and D_2O as well as their interaction on continuous samaria thin films and samaria islands on Pt(111). Our results reveal that, above room temperature, CO only adsorbs on exposed Pt areas whereas D_2O may dissociate on samaria surfaces. The D_2O dissociation can be promoted by reducing the SmO_x surfaces and, in particular, by reducing SmO_x islands which exhibit perimeter sites at their boundary to bare Pt(111) area. The existence of such perimeter sites appears to be necessary for CO_2 production which, however, always consumes oxygen from the SmO_x lattice. Under the conditions of our experiments, although D_2O dissociation is promoted and must produce OD and/or O species on reduced SmO_x surfaces, these species do not show the capability of oxidizing CO to CO_2 . Therefore, our TPD experiments under UHV conditions do not provide any evidence for the WGS reaction on our epitaxial samaria-Pt(111) system, neither via the redox nor the associative mechanism. In comparison to reducible oxides, such as ceria and titania which have been employed for WGS catalysis, reduced oxygen mobility and limited flexibility of the oxidation state of samaria may play a role and suppress the WGS redox mechanism. Intriguingly, however, our TPD data reveal an interaction between CO and OD species on the perimeter sites between the reduced SmO_x islands and Pt which leads to a pronounced D_2 production without forming CO_2 . To the best of our knowledge, these are the first data to demonstrate that samaria shows potential for hydrogen production. Overall, they demonstrate the important role that the perimeter sites between metal and oxide may play for chemical reactions

on samaria-based catalysts.

Acknowledgements

Funding by the Deutsche Forschungsgemeinschaft is gratefully acknowledged.

References

- [1] D.S. Newsome, The water-gas shift reaction, *Catalysis Reviews*, 21 (1980) 275-318.
- [2] C. Ratnasamy, J.P. Wagner, Water gas shift catalysis, *Catalysis Reviews*, 51 (2009) 325-440.
- [3] C. Rhodes, G.J. Hutchings, A.M. Ward, Water-gas shift reaction: finding the mechanistic boundary, *Catalysis Today*, 23 (1995) 43-58.
- [4] R.J.B. Smith, M. Loganathan, S. Shantha Murthy, A review of the water gas shift reaction kinetics, *International Journal of Chemical Reactor Engineering*, 8 (2010) 1542-6580.
- [5] M.V. Twigg, M.S. Spencer, Deactivation of supported copper metal catalysts for hydrogenation reactions, *Applied Catalysis A: General*, 212 (2001) 161-174.
- [6] G. Jacobs, B.H. Davis, Low temperature water-gas shift catalysts, *Catalysis: Volume 20*, The Royal Society of Chemistry, 2007, pp. 122-285.
- [7] A. Luengnaruemitchai, S. Osuwan, E. Gulari, Comparative studies of low-temperature water-gas shift reaction over Pt/CeO₂, Au/CeO₂, and Au/Fe₂O₃ catalysts, *Catalysis Communications*, 4 (2003) 215-221.
- [8] I.D. González, R.M. Navarro, W. Wen, N. Marinkovic, J.A. Rodríguez, F. Rosa, J.L.G. Fierro, A comparative study of the water gas shift reaction over platinum catalysts supported on CeO₂, TiO₂ and Ce-modified TiO₂, *Catalysis Today*, 149 (2010) 372-379.
- [9] A.M. Duarte de Farias, D. Nguyen-Thanh, M.A. Fraga, Discussing the use of modified ceria as support for Pt catalysts on water-gas shift reaction, *Applied Catalysis B: Environmental*, 93 (2010) 250-258.
- [10] D. Andreeva, V. Idakiev, T. Tabakova, L. Ilieva, P. Falaras, A. Bourlinos, A. Travlos, Low-temperature water-gas shift reaction over Au/CeO₂ catalysts, *Catalysis Today*, 72 (2002) 51-57.
- [11] F. Boccuzzi, A. Chiorino, M. Manzoli, D. Andreeva, T. Tabakova, L. Ilieva, V. Iadakiev,

Gold, silver and copper catalysts supported on TiO₂ for pure hydrogen production, *Catalysis Today*, 75 (2002) 169-175.

[12] P. Panagiotopoulou, D.I. Kondarides, Effect of morphological characteristics of TiO₂-supported noble metal catalysts on their activity for the water–gas shift reaction, *Journal of Catalysis*, 225 (2004) 327-336.

[13] J. Graciani, J.F. Sanz, Designing a new generation of catalysts: Water gas shift reaction example, *Catalysis Today*, 240 Part B (2015) 214-219.

[14] J. Nakamura, J.M. Campbell, C.T. Campbell, Kinetics and mechanism of the water-gas shift reaction catalysed by the clean and Cs-promoted Cu(110) surface: a comparison with Cu(111), *Journal of the Chemical Society, Faraday Transactions*, 86 (1990) 2725-2734.

[15] A.B. Mhadeshwar, D.G. Vlachos, Microkinetic modeling for water-promoted CO oxidation, water–gas shift, and preferential oxidation of CO on Pt, *The Journal of Physical Chemistry B*, 108 (2004) 15246-15258.

[16] A.A. Gokhale, J.A. Dumesic, M. Mavrikakis, On the mechanism of low-temperature water gas shift reaction on copper, *Journal of the American Chemical Society*, 130 (2008) 1402-1414.

[17] C.V. Ovesen, P. Stoltze, J.K. Nørskov, C.T. Campbell, A kinetic model of the water gas shift reaction, *Journal of Catalysis*, 134 (1992) 445-468.

[18] S. Hilaire, X. Wang, T. Luo, R.J. Gorte, J. Wagner, A comparative study of water-gas-shift reaction over ceria supported metallic catalysts, *Applied Catalysis A: General*, 215 (2001) 271-278.

[19] Q. Fu, H. Saltsburg, M. Flytzani-Stephanopoulos, Active nonmetallic Au and Pt species on ceria-based water-gas shift catalysts, *Science*, 301 (2003) 935-938.

[20] S.D. Senanayake, D. Stacchiola, J.A. Rodriguez, Unique properties of ceria nanoparticles

supported on metals: novel inverse ceria/copper catalysts for CO oxidation and the water-gas shift reaction, *Accounts of Chemical Research*, 46 (2013) 1702-1711.

[21] R.J. Gorte, Ceria in catalysis: From automotive applications to the water–gas shift reaction, *AIChE Journal*, 56 (2010) 1126-1135.

[22] R.J. Gorte, S. Zhao, Studies of the water-gas-shift reaction with ceria-supported precious metals, *Catalysis Today*, 104 (2005) 18-24.

[23] T. Bunluesin, R.J. Gorte, G.W. Graham, Studies of the water-gas-shift reaction on ceria-supported Pt, Pd, and Rh: Implications for oxygen-storage properties, *Applied Catalysis B: Environmental*, 15 (1998) 107-114.

[24] A. Trovarelli, Catalytic properties of ceria and CeO₂-containing materials, *Catalysis Reviews*, 38 (1996) 439-520.

[25] D.R. Mullins, The surface chemistry of cerium oxide, *Surface Science Reports*, 70 (2015) 42-85.

[26] C. Sun, H. Li, L. Chen, Nanostructured ceria-based materials: synthesis, properties, and applications, *Energy & Environmental Science*, 5 (2012) 8475-8505.

[27] K. Mudiyansele, S.D. Senanayake, L. Feria, S. Kundu, A.E. Baber, J. Graciani, A.B. Vidal, S. Agnoli, J. Evans, R. Chang, S. Axnanda, Z. Liu, J.F. Sanz, P. Liu, J.A. Rodriguez, D.J. Stacchiola, Importance of the metal–oxide interface in catalysis: in situ studies of the water–gas shift reaction by ambient-pressure X-ray photoelectron spectroscopy, *Angewandte Chemie International Edition*, 52 (2013) 5101-5105.

[28] J.-H. Jhang, A. Schaefer, W. Cartas, S. Epuri, M. Bäumer, J.F. Weaver, Growth and partial reduction of Sm₂O₃(111) thin films on Pt(111): Evidence for the formation of SmO(100), *The Journal of Physical Chemistry C*, 117 (2013) 21396-21406.

- [29] J.-H. Jhang, A. Schaefer, V. Zielasek, J. Weaver, M. Bäumer, Methanol adsorption and reaction on samaria thin films on Pt(111), *Materials*, 8 (2015) 6228-6256.
- [30] R.J. Madix, The application of flash desorption spectroscopy to chemical reactions on surfaces: Temperature programmed reaction spectroscopy, *Critical Reviews in Solid State and Materials Sciences*, 7 (1978) 143-152.
- [31] E.M. Stuve, S.W. Jorgensen, R.J. Madix, The adsorption of H₂O on clean and oxygen-covered Pd(100): Formation and reaction of OH groups, *Surface Science*, 146 (1984) 179-198.
- [32] M.L. Burke, R.J. Madix, Effect of CO on hydrogen thermal desorption from Fe(100), *Surface Science*, 237 (1990) 20-34.
- [33] C.J. Powell, A. Jablonski, NIST electron effective-attenuation-length database - Version 1.3, National Institute of Standards and Technology, Gaithersburg, MD, 2011.
- [34] Q. Guo, Y. Zhao, C. Jiang, W.L. Mao, Z. Wang, Phase transformation in Sm₂O₃ at high pressure: In situ synchrotron X-ray diffraction study and ab initio DFT calculation, *Solid State Communications*, 145 (2008) 250-254.
- [35] G. Ertl, M. Neumann, K.M. Streit, Chemisorption of CO on the Pt(111) surface, *Surface Science*, 64 (1977) 393-410.
- [36] D.M. Collins, W.E. Spicer, The adsorption of CO, O₂, and H₂ on Pt: I. Thermal desorption spectroscopy studies, *Surface Science*, 69 (1977) 85-113.
- [37] P.A. Redhead, Thermal desorption of gases, *Vacuum*, 12 (1962) 203-211.
- [38] T. Kuriyama, K. Kunimori, H. Nozoye, Adsorption of carbon monoxide on a SmO_x film, *Chemical Communications*, (1998) 501-502.
- [39] T. Kuriyama, K. Kunimori, H. Nozoye, Interaction of CO with the SmO_x/Ru(001) interface, *Surface Science*, 402–404 (1998) 178-181.

- [40] S. Royer, D. Duprez, Catalytic Oxidation of carbon monoxide over transition metal oxides, *ChemCatChem*, 3 (2011) 24-65.
- [41] K.L. Feilberg, S.R. Sellevag, C.J. Nielsen, D.W.T. Griffith, M.S. Johnson, CO + OH → CO₂ + H: The relative reaction rate of five CO isotopologues, *Physical Chemistry Chemical Physics*, 4 (2002) 4687-4693.
- [42] D.D. Sarma, M.S. Hegde, C.N.R. Rao, Study of surface oxidation of rare-earth metals by photoelectron spectroscopy, *Journal of the Chemical Society, Faraday Transactions 2: Molecular and Chemical Physics*, 77 (1981) 1509-1520.
- [43] F.P. Netzer, J.A.D. Matthew, Surfaces of rare earth metals, *Reports on Progress in Physics*, 49 (1986) 621-681.
- [44] G. Held, D. Menzel, Isotope effects in structure and kinetics of water adsorbates on Ru(001), *Surface Science*, 327 (1995) 301-320.
- [45] D.N. Denzler, S. Wagner, M. Wolf, G. Ertl, Isotope effects in the thermal desorption of water from Ru(001), *Surface Science*, 532–535 (2003) 113-119.
- [46] G.B. Fisher, J.L. Gland, The interaction of water with the Pt(111) surface, *Surface Science*, 94 (1980) 446-455.
- [47] M. Kinne, T. Fuhrmann, J.F. Zhu, B. Tränkenschuh, R. Denecke, H.P. Steinrück, Coadsorption of D₂O and CO on Pt(111) Studied by in Situ High-Resolution X-ray Photoelectron Spectroscopy, *Langmuir*, 20 (2004) 1819-1826.
- [48] A. Picolin, C. Busse, A. Redinger, M. Morgenstern, T. Michely, Desorption of H₂O from Flat and Stepped Pt(111), *The Journal of Physical Chemistry C*, 113 (2009) 691-697.
- [49] Y. Lykhach, V. Johánek, H.A. Aleksandrov, S.M. Kozlov, M. Happel, T. Skála, P.S. Petkov, N. Tsud, G.N. Vayssilov, K.C. Prince, K.M. Neyman, V. Matolín, J. Libuda, Water chemistry on

model ceria and Pt/ceria catalysts, *The Journal of Physical Chemistry C*, 116 (2012) 12103-12113.

[50] M. Fronzi, S. Piccinin, B. Delley, E. Traversa, C. Stampfl, Water adsorption on the stoichiometric and reduced $\text{CeO}_2(111)$ surface: a first-principles investigation, *Physical Chemistry Chemical Physics*, 11 (2009) 9188-9199.

[51] S. Gritschneider, M. Reichling, Structural elements of $\text{CeO}_2(111)$ surfaces, *Nanotechnology*, 18 (2007) 044024.

[52] M.A. Henderson, The interaction of water with solid surfaces: fundamental aspects revisited, *Surface Science Reports*, 46 (2002) 1-308.

[53] L. Kundakovic, D.R. Mullins, S.H. Overbury, Adsorption and reaction of H_2O and CO on oxidized and reduced $\text{Rh/CeO}_x(111)$ surfaces, *Surface Science*, 457 (2000) 51-62.

[54] D.R. Mullins, P.M. Albrecht, T.-L. Chen, F.C. Calaza, M.D. Biegalski, H.M. Christen, S.H. Overbury, Water dissociation on $\text{CeO}_2(100)$ and $\text{CeO}_2(111)$ thin films, *The Journal of Physical Chemistry C*, 116 (2012) 19419-19428.

[55] H. Nörenberg, G.A.D. Briggs, Defect formation on $\text{CeO}_2(111)$ surfaces after annealing studied by STM, *Surface Science*, 424 (1999) L352-L355.

[56] S. Eck, C. Castellarin-Cudia, S. Surnev, M.G. Ramsey, F.P. Netzer, Growth and thermal properties of ultrathin cerium oxide layers on $\text{Rh}(111)$, *Surface Science*, 520 (2002) 173-185.

[57] U. Diebold, J. Lehman, T. Mahmoud, M. Kuhn, G. Leonardelli, W. Hebenstreit, M. Schmid, P. Varga, Intrinsic defects on a $\text{TiO}_2(110)(1\times 1)$ surface and their reaction with oxygen: a scanning tunneling microscopy study, *Surface Science*, 411 (1998) 137-153.

[58] B. Chen, Y. Ma, L. Ding, L. Xu, Z. Wu, Q. Yuan, W. Huang, Reactivity of hydroxyls and water on a $\text{CeO}_2(111)$ thin film surface: The role of oxygen vacancy, *The Journal of Physical*

Chemistry C, 117 (2013) 5800-5810.

[59] V. Matolín, I. Matolínová, F. Dvořák, V. Johánek, J. Mysliveček, K.C. Prince, T. Skála, O. Stetsovych, N. Tsud, M. Václavů, B. Šmíd, Water interaction with CeO₂(111)/Cu(111) model catalyst surface, *Catalysis Today*, 181 (2012) 124-132.

[60] S.D. Senanayake, D. Stacchiola, J. Evans, M. Estrella, L. Barrio, M. Pérez, J. Hrbek, J.A. Rodriguez, Probing the reaction intermediates for the water–gas shift over inverse CeO_x/Au(111) catalysts, *Journal of Catalysis*, 271 (2010) 392-400.

[61] K. Christmann, G. Ertl, T. Pignet, Adsorption of hydrogen on a Pt(111) surface, *Surface Science*, 54 (1976) 365-392.

[62] P. Bene, L. Klaus, C. George, The dissociative adsorption of hydrogen on defect-'free' Pt(111), *Journal of Physics: Condensed Matter*, 22 (2010) 304006.

[63] F.T. Wagner, T.E. Moylan, S.J. Schmiegel, Hydrophilic versus hydrophobic coadsorption: Carbon monoxide and water on Rh(111) versus Pt(111), *Surface Science*, 195 (1988) 403-428.

[64] D. Marrocchelli, B. Yildiz, First-principles assessment of H₂S and H₂O reaction mechanisms and the subsequent hydrogen absorption on the CeO₂(111) Surface, *The Journal of Physical Chemistry C*, 116 (2011) 2411-2424.

[65] C.-S. Chen, W.-H. Cheng, S.-S. Lin, Study of reverse water gas shift reaction by TPD, TPR and CO₂ hydrogenation over potassium-promoted Cu/SiO₂ catalyst, *Applied Catalysis A: General*, 238 (2003) 55-67.

[66] W. Wang, S. Wang, X. Ma, J. Gong, Recent advances in catalytic hydrogenation of carbon dioxide, *Chemical Society Reviews*, 40 (2011) 3703-3727.

[67] I.A. Fisher, A.T. Bell, A mechanistic study of methanol decomposition over Cu/SiO₂, ZrO₂/SiO₂, and Cu/ZrO₂/SiO₂, *Journal of Catalysis*, 184 (1999) 357-376.

Article

Methanol Adsorption and Reaction on Samaria Thin Films on Pt(111)

Jin-Hao Jhang ¹, Andreas Schaefer ^{1,*}, Volkmar Zielasek ¹, Jason F. Weaver ² and Marcus Bäumer ¹

¹ Institute of Applied and Physical Chemistry & Center for Environmental Research and Sustainable Technology, University Bremen, Leobener Strasse UFT, Bremen 28359, Germany; E-Mails: jhang@uni-bremen.de (J.-H.J.); zielasek@uni-bremen.de (V.Z.); mbaeumer@uni-bremen.de (M.B.)

² Department of Chemical Engineering, University of Florida, Gainesville, FL 32611, USA; E-Mail: jweaver@che.ufl.edu

* Author to whom correspondence should be addressed; E-Mail: andreas.schaefer@uni-bremen.de; Tel.: +49-421-2186-3176; Fax: +49-421-2186-3188.

Academic Editor: Jan Ingo Flege

Received: 13 August 2015 / Accepted: 9 September 2015 / Published: 17 September 2015

Abstract: We investigated the adsorption and reaction of methanol on continuous and discontinuous films of samarium oxide (SmO_x) grown on Pt(111) in ultrahigh vacuum. The methanol decomposition was studied by temperature programmed desorption (TPD) and infrared reflection absorption spectroscopy (IRRAS), while structural changes of the oxide surface were monitored by low-energy electron diffraction (LEED). Methanol dehydrogenates to adsorbed methoxy species on both the continuous and discontinuous SmO_x films, eventually leading to the desorption of CO and H_2 which desorbs at temperatures in the range 400–600 K. Small quantities of CO_2 are also detected mainly on as-prepared Sm_2O_3 thin films, but the production of CO_2 is limited during repeated TPD runs. The discontinuous film exhibits the highest reactivity compared to the continuous film and the Pt(111) substrate. The reactivity of methanol on reduced and reoxidized films was also investigated, revealing how SmO_x structures influence the chemical behavior. Over repeated TPD experiments, a SmO_x structural/chemical equilibrium condition is found which can be approached either from oxidized or reduced films. We also observed hydrogen absence in TPD which indicates that hydrogen is stored either in SmO_x films or as OH groups on the SmO_x surfaces.

Keywords: rare earth oxide; thin film; samaria; inverse catalysts; temperature programmed desorption (TPD)

1. Introduction

Rare earth oxides (REOs), especially the oxides of lanthanum and cerium, find their main applications as catalysts in the chemical industry. Lanthana is mostly employed for so called “fluid cracking” to break up long-chain hydrocarbons, whereas ceria, at times with additives of praseodymia, is employed as an oxygen storage material for exhaust gas cleaning in heterogeneous reactions (e.g., CO oxidation, NO reduction in automotive catalysts) [1]. Basic research has thus mainly focused on ceria and lanthana [2]. Nevertheless the other oxides of the rare earth elements have also shown promising potential in diverse fields like microelectronics [3] or in heterogeneously catalyzed reactions for which the selective formation of an intermediate product has increased importance. As examples, reactions such as the oxidation of organic compounds [4], the oxidative coupling of methane [5–7], and the water-gas shift reaction [8,9] can be mentioned.

The versatility of certain rare earth oxides, as for many transition metal oxides, has its origin in the ability of the metal ion to easily switch its oxidation state. All rare earth elements can exist in a trivalent state (3+) and form a sesquioxide, RE_2O_3 . Only cerium, praseodymium, and terbium can form a dioxide with the metal in the 4+ oxidation state [10]. Also, these oxides form many structural phases with intermediate oxygen contents. In their stable forms under atmospheric conditions CeO_2 , Pr_6O_{11} and Tb_4O_7 have shown superior lattice oxygen mobility and a number of stable intermediate crystallographic phases. This property makes them good catalysts for total oxidation reactions and ceria has been studied extensively also in the field of surface science. Additionally, it has recently been found that inverse model catalyst systems of CeO_x nanoparticles grown for example on Au and Cu substrates exhibit high reactivity for the water-gas shift reaction [9,11,12]. However, only few studies so far attempt to study model systems of REOs other than ceria [13–15]. Apart from CeO_x , PrO_x and TbO_x , REOs only form sesquioxides (RE_2O_3) which exhibit a relatively low mobility of lattice oxygen. The lower oxygen mobility can be beneficial for the selectivity of certain chemical conversions such as, for example, the oxidative coupling of methane (OCM). In the OCM reaction sesquioxides like La_2O_3 , Sm_2O_3 or Eu_2O_3 , among other sesquioxides and certain REO mixtures, have shown an increased C2 selectivity [6]. Oxides of Sm or Eu could be of special interest, because they possess the capability to change their oxidation state to 2+, as reported under extreme conditions for the bulk oxides [10]. However, surface science studies of sesquioxide model systems are scarce or lacking completely in the context of model catalysis, and the relationship between surface structure and reactivity of the oxides is still largely unknown.

In a previous study combining scanning tunneling microscopy (STM) and low-energy electron diffraction (LEED) we have demonstrated that a high-quality $\text{Sm}_2\text{O}_3(111)$ thin film can be grown on Pt(111) by reactive physical vapor deposition (RPVD) [13]. Growing a thin oxide film on a conducting substrate allows for employing the whole set of surface science methodology to study structure, stability, and reactivity of the oxide surface. Furthermore structures may be stabilized which are not stable in bulk oxides under atmospheric conditions [16]. If discontinuous films of the oxide are prepared, the influence

of the metal-oxide interface at the boundary of the oxide islands to the Pt substrate can be studied and possible cooperative effects of the two materials revealed.

As shown in Ref. [13], samaria grows in a defective fluorite structure on Pt(111), in which the Sm atoms form a well-ordered (1.37×1.37) hexagonal sub-lattice in registry with Pt(111), whereas oxygen vacancies are distributed randomly within the film. We found that the Sm_2O_3 films can be reduced thermally, forming domains of $\text{SmO}(001)$, and re-oxidized by annealing in molecular oxygen. Hence, a reduction re-oxidation cycle is in principle possible on SmO_x thin films. In the present article we report a study of the adsorption of methanol (MeOH) on as-prepared, reduced, and re-oxidized SmO_x surfaces. MeOH is considered as a versatile probe molecule for characterizing chemical properties of metal oxide surfaces. It has been shown that the dissociation and oxidation of MeOH on metal oxides are strongly affected by the nature of metal oxides. The reaction products can indicate the nature of active sites on metal oxide surfaces because Lewis and Brønsted acid sites dehydrate MeOH to form dimethyl ether, redox sites oxidatively dehydrogenate MeOH to form formaldehyde, and basic sites dehydrogenate MeOH to form CO and CO_2 . Studies of MeOH oxidation reaction also have been performed on diverse ceria surfaces, e.g., $\text{CeO}_2(111)$, $\text{CeO}_x(111)$, and $\text{CeO}_x(100)$ using classical surface science tools [17–19]. The results reveal that formaldehyde and H_2O as products are formed on the $\text{CeO}_2(111)$ surface, whereas CO, CO_2 , and H_2 are produced from both $\text{CeO}_x(111)$ and $\text{CeO}_x(100)$ surfaces, suggesting that the chemical behavior of the ceria surface can be altered by its surface structure as well as oxidation states.

In this article we study the adsorption and reaction of MeOH on a continuous film, only a few O-Sm-O trilayers thick, compared to a discontinuous film of SmO_x islands which form at sub-monolayer coverage and leave Pt(111) area exposed. In addition, we investigate the effect of reduction and reoxidation of the oxide film on the reactivity and discuss the influence of the presence of both oxide and metal surface sites in close proximity on the reaction mechanism. By combining temperature-programmed desorption (TPD), infrared reflection-absorption spectroscopy (IRRAS), and LEED with structural information previously determined by STM, we find strong correlations between the $\text{SmO}_x/\text{Pt}(111)$ film structure and its chemical properties.

2. Experimental Section

The experiments were carried out in two UHV chambers each with a base pressure below 5×10^{-10} mbar. The first chamber is equipped with a quadrupole mass spectrometer (HIDEN Analytical Ltd., Warrington, UK), an e-beam evaporator (EFM3 by Scienta Omicron, Taunusstein, Germany), an ion sputter source (SPECS GmbH, Berlin, Germany), a four-grid LEED (Scienta Omicron, Taunusstein, Germany), a X-ray gun (Scienta Omicron, Taunusstein, Germany), and a hemispherical electron analyzer (E10 by former Leybold AG, Hanau, Germany). The second chamber houses an IR spectrometer with MCT detector for infrared reflection absorption spectroscopy (IRRAS, Vertex 80v by Bruker Optic GmbH, Ettlingen, Germany) and an e-beam evaporator (EFM3), ion source and a combined LEED/AES optics (SPECS GmbH, Berlin, Germany).

The oxide films were grown on a Pt(111) single crystal (SPL). The crystal is a circular disk (9 mm diameter) which was mounted on a molybdenum sample plate. A type-K thermocouple was spot-welded onto the backside of the Pt(111) crystal for temperature measurement. The Pt(111) crystal surface was cleaned by repeated cycles of Ar^+ sputtering (1 keV) at room temperature for 20 min with annealing

in UHV at 1000 K for 15 min, followed by annealing in O₂ ($P = 5 \times 10^{-7}$ mbar) for 10 min at the same temperature. The surface is considered clean when the C and O signals in X-ray photoelectron spectroscopy (XPS) or Auger electron spectroscopy (AES) were below the detection limits (XPS: atomic ratios of C/Pt and O/Pt < 0.02; AES: atomic ratios of C/Pt and O/Pt < 0.03).

Samaria thin films were grown by reactive physical vapor deposition (RPVD) in O₂ background ($P = 5 \times 10^{-7}$ mbar) at 600 K crystal temperature followed by post-annealing in O₂ background ($P = 5 \times 10^{-7}$ mbar) at 1000 K for 10 min. The estimation of the film thickness is based on attenuation of the Pt 4f_{7/2} peak intensity in XPS spectra (Al K_α radiation). An inelastic mean free path of 25.03 Å is used for the Pt 4f_{7/2} photoelectrons with the kinetic energy of 1414.7 eV in the XPS/TPD chamber. In the IRRAS chamber, the film thickness is estimated by measuring the attenuation of the Pt (NOO) peak intensity at 168 eV in AES spectra and an inelastic mean free path of 5.53 Å. The IMFP values from NIST database are determined by considering a bulk c-Sm₂O₃ (density: 8.347 g/cm³) grown on Pt(111). The thickness of one monolayer (ML) of Sm₂O₃ (111) is defined as equal to 3.18 Å, which corresponds to the average length of a trilayer O-Sm-O along the <111> direction of a c-Sm₂O₃ bixbyite structure. For TPD experiments, 0.9 ± 0.1 ML and 2.8 ± 0.1 ML Sm₂O₃ thin films were grown on the Pt(111) substrate. A 0.7 ± 0.2 ML Sm₂O₃ thin film was prepared for the IRRAS experiments. A well ordered Sm₂O₃ (111) thin film exhibits a hexagonal (1.37×1.37) lattice pattern in registry with Pt(111)-(1×1) in LEED. In the coverage range of 1 to 3 ML, additional spots can be observed which originates from a quasi- 3×3 superstructure relative to the Sm₂O₃ lattice. For further details see [13].

MeOH TPD was performed by dosing 15 Langmuir (L) of MeOH purified by five freeze-pump-thaw cycles onto a sample held at 96 K at a background pressure below 5.0×10^{-10} mbar. The temperature was ramped with a well-controlled rate of 1 K/s from 100 to 800 K. The signal of six masses ($m/z = 2$ (H₂), 18 (H₂O), 28 (CO), 29 (CH₂O), 31 (CH₃OH) and 44 (CO₂)) were monitored. Repeated TPD experiments were performed immediately after a previous TPD experiment when the sample has returned to < 100 K and further MeOH could be dosed. The intensities of recorded masses were normalized to the ionization probability of the respective molecule. To better identify small desorption features some spectra were multiplied by factors given in the respective figure. For the quantification of products, we define one monolayer equivalent (MLE) as the surface atomic density of Pt(111), being 1.52×10^{15} cm⁻². For calibration of the TPD signal intensity 1/3 MLE of CO was dosed to clean Pt(111) at room temperature, forming a ($\sqrt{3} \times \sqrt{3}$)R30° diffraction pattern in LEED. The integral intensity of the CO desorption signal corresponding to 1/3 MLE is then taken as the reference for all yields determined in this study.

IRRAS results were obtained by guiding infrared light through a KBr window to the sample at an angle of incidence of ~83° to the sample surface normal. The reflected beam passes through another KBr window and impinges onto a nitrogen cooled HgCdTe (MCT) detector. Spectra were recorded with a resolution of 2 cm⁻¹ and over 200 scans were averaged between 600–4000 cm⁻¹. Additionally, for the IRRAS experiments 15 Langmuir of MeOH were dosed to the sample at 96 K and a background pressure below 5×10^{-10} mbar. For the heating series the sample was heated to the respective temperature, held for one minute and then rapidly cooled again to ~96 K before the measurement was started.

3. Results and Discussion

3.1. MeOH on Clean Pt(111)

To determine the contribution of the Pt(111) substrate to the MeOH reaction, we carried out a MeOH TPD experiment on a clean Pt(111) surface by dosing 15 Langmuir of MeOH on the surface at a substrate temperature of 96 K. The TPD spectrum is shown in Figure 1a. In the TPD spectrum, the multilayer and monolayer desorption of MeOH are observed at 140 and 180 K, respectively. All signals detected below 250 K are caused by fragmentation of MeOH in the mass spectrometer. As products, only H₂ and CO are observed with peak positions at 315 and 420 K, respectively. The yields of products will be quantified in units of monolayer equivalents (MLE) in the following. One MLE is defined as the surface atomic density of Pt(111), that is, $1.52 \times 10^{15} \text{ cm}^{-2}$. The integral intensity of the TPD peak of 1/3 MLE CO on Pt(111) was employed for calibration as described in the experimental section. Only small yields of CO (0.04 ± 0.01 MLE) and H₂ (0.07 ± 0.01 MLE) are produced from the reaction on Pt(111). The average ratio of H₂ to CO is approximately two, suggesting complete decomposition of the reacting MeOH and desorption of products via $\text{CH}_3\text{OH} \rightarrow \text{CO} + 2 \text{H}_2$. The amount of CO is equal to the amount of reacted MeOH on Pt(111), *i.e.*, only 0.04 ± 0.01 MLE MeOH do react, showing that Pt(111) exhibits minor activity for MeOH decomposition. Our result is in good quantitative agreement with previous MeOH TPD experiments on clean Pt(111) which found a maximum amount of 0.047 MLE MeOH decomposing [20]. Previous studies suggest that defects on the Pt(111) surface play an essential role for promoting the MeOH reaction, and that the intermediates of the MeOH reaction leading to final products (CO and H₂) are nearly undetectable on Pt(111) experimentally [21–23]. Theoretical studies of the MeOH reaction on Pt(111) have been performed as well, but there is still no agreement/conclusion on whether the first step of MeOH reaction on Pt(111) proceeds by the C-H bond scission to form hydroxymethyl or by O-H bond scission to form methoxy [24,25].

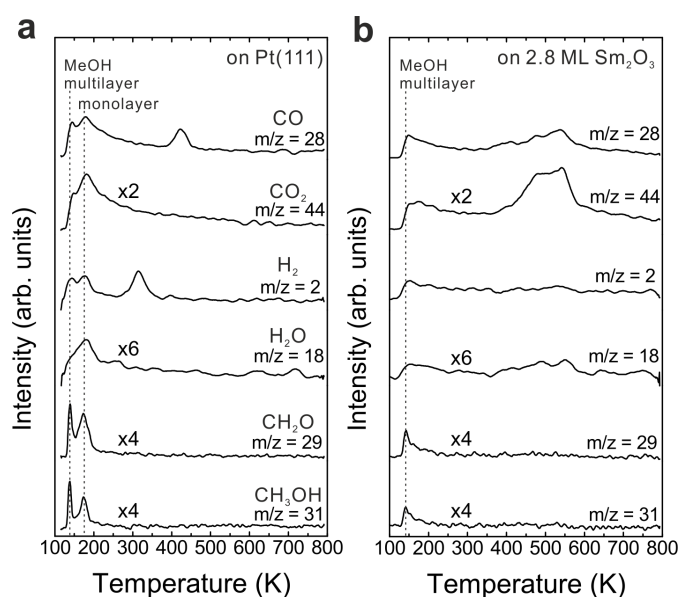


Figure 1. TPD spectra recorded from (a) a clean Pt(111) and (b) a 2.8 ML as-prepared Sm₂O₃ thin film.

3.2. As-Prepared Continuous Sm₂O₃ Film

Figure 1b shows TPD traces obtained after dosing 15 Langmuir of MeOH on a Sm₂O₃ thin film with a nominal thickness of 2.8 ± 0.1 ML at the surface temperature of 96 K. No peaks are observed in the temperature range of H₂ and CO desorption from MeOH reaction on Pt(111), suggesting that the Pt substrate is fully covered by the Sm₂O₃ thin film. Compared to the desorption features from Pt(111), a smaller MeOH multilayer desorption peak appears at the same temperature as from the bare Pt(111) surface. Furthermore, the desorption feature of a MeOH monolayer can be hardly discerned which suggests that most of the adsorbed MeOH monolayer is able to react on the Sm₂O₃ surface. Different from the MeOH decomposition on Pt [26], the MeOH reaction on the Sm₂O₃ film leads to CO and CO₂ as the main products detected in the range of 400–600 K in the TPD spectrum. No other products are observed. Quantification reveals that 0.13 ± 0.01 MLE CO and almost the same amount of CO₂ (0.14 ± 0.01 MLE) are produced. In addition, the MeOH turnover values hence are 0.27 MLE on the continuous Sm₂O₃ thin film compared to 0.04 MLE on Pt(111) showing that the Sm₂O₃ thin film exhibits much higher reactivity than a bare Pt(111) surface.

The production of CO₂ is intriguing because it indicates that there is oxygen from the oxide available for CO₂ formation. We consider three possible sources for this “active” oxygen contributing to CO₂ formation: (1) surface OH, (2) lattice oxygen and (3) weakly bound molecular oxygen species on the SmO_x surface. Surface OH could react with CO and form, via carboxyl (HOCO) and/or formate (HCOO) species as intermediates, CO₂ and H as products [26,27]. The lattice oxygen on the Sm₂O₃ surface could contribute by fully oxidizing MeOH to CO₂, via reduction of the oxide. A similar behavior has been found on lanthana thin films grown on an Al₂O₃ (0001) substrate by examining CO oxidation to CO₂ which, as a result, leads to reduction of the lanthana thin films [28]. Gorte *et al.* demonstrated the existence of weakly bound oxygen on a CeO₂(111) surface which desorbs in a temperature range between 800 and 1200 K [29]. We checked our Sm₂O₃ thin films for such a species by recording an O₂ TPD spectrum (not shown) between 300–1000 K with a heating rate of 1 K/s, but did not observe O₂ desorption. Therefore, we conclude that both surface OH and lattice oxygen can be oxygen sources for the CO₂ formation, while no weakly bound oxygen species is present on the Sm₂O₃ thin film.

Quantifying our MeOH TPD result for the closed Sm₂O₃ film reveals that a considerable amount of H (1.08 MLE) is missing in the balance, *i.e.*, not desorbing from the surface. Amounts of missing H in TPD suggests that H atoms remain on or in the SmO_x/Pt(111) sample, possibly via OH formation on the SmO_x surface and/or by diffusion into the SmO_x film or even into the Pt substrate. Considering one trilayer (O-Sm-O) in a bulk Sm₂O₃ in bixbyite structure, there are only 0.40 MLE top-layer O exposed, meaning that only a maximum of 0.40 MLE H can react with top-layer O forming OH. Consequently, a minimum of 0.68 MLE H must diffuse into the oxide and/or to the Pt-oxide interface, or into the Pt substrate.

To determine if MeOH adsorption, reaction and desorption of the products alter the chemical properties of the samaria surface, we performed repeated MeOH TPD experiments. The corresponding TPD spectra obtained from the 2.8 ML as-prepared Sm₂O₃ thin film are shown in Figure 2a. The second MeOH TPD experiment was carried out immediately after the first TPD run and involved cooling to 96 K and adsorbing 15 Langmuir of MeOH again. The spectra exhibit significant changes in the CO, CO₂ and H₂ TPD features. We observe that CO and H₂ desorb concurrently in large TPD peaks at 540 K. Compared to the 1st TPD results, the CO₂ desorption peak intensity is lower by a factor of

seven and the integrated intensity of the CO peak is higher by a factor of 2.15, while the peak maxima have a ratio of 3.6. The strong decrease of the CO₂ desorption peak suggests that most of the “active” oxygen was removed from the surface during the 1st TPD run. Afterwards, the third TPD and the fourth TPD were also carried out immediately after their previous TPD run. There is no significant difference between the third and the fourth TPD, however, both of them show that the CO, CO₂, and H₂ desorption peaks shift to higher temperature by 30 K compared to the second TPD. Overall, the product yields slightly decrease after the second TPD experiment. The fact that MeOH reacting on the SmO_x thin film forms CO, CO₂ and H₂ as the main products suggests that dehydrogenation of MeOH is the dominant reaction. MeOH dehydrogenating to methoxy species (CH₃O⁻) has been well-studied, especially on metal oxides. Moreover, the methoxy species can further completely dehydrogenate to CO and H₂ as the final products. Hence, according to our TPD result, SmO_x is a basic oxide as revealed by the MeOH reaction. MeOH reacting on an acidic surface would undergo a dehydration reaction and form dimethyl ether as the final product [30,31] which we do not observe. Furthermore, the TPD result suggests that the C–H bond scission of methoxy species is the rate-determining step because the desorption temperature of the products is identical. As soon as the C–H scission takes place, H₂ and CO (also CO₂) are formed and desorb from the surface immediately.

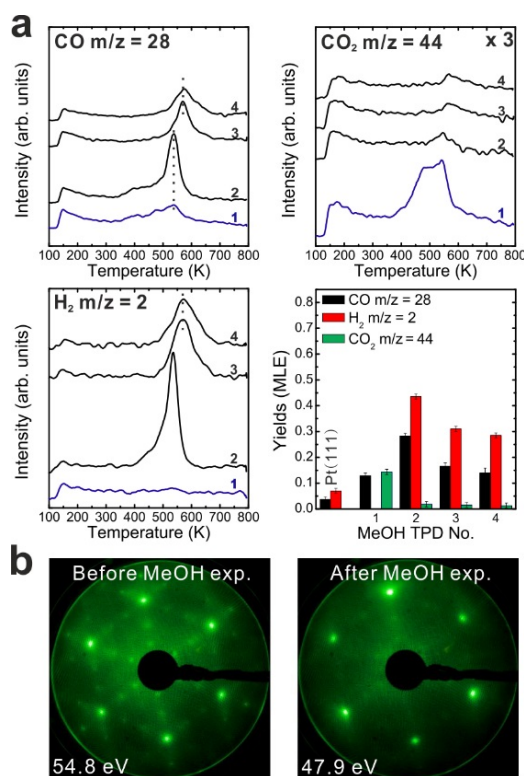


Figure 2. (a) Repeated TPD series collected on a 2.8 ML as-prepared Sm₂O₃ thin film and the estimated yields of products, (b) LEED results obtained before and after the repeated MeOH TPD experiments.

The decrease of the CO₂ yield during repeated TPD experiments suggests that surface OH and/or lattice oxygen species consumed for CO oxidation are not replenished and should leave surface defects/vacancies behind which could enhance the binding strength between methoxy species and the

SmO_x surface. From this point of view, more surface defects/vacancies are created over repeated TPD runs which may explain why product TPD features change and the peaks shift to higher temperatures, meaning that the chemical behavior of SmO_x is changed by the MeOH reaction. It should be mentioned here, that IRRAS data to be presented later support this interpretation.

A deficit of H in the desorption balance is mainly observed in the first TPD experiment, but also occurs in the subsequent TPD experiments. The amount of missing H dramatically decreases from 1.08 MLE to 0.32 MLE after the first TPD which indicates that adsorbed H forming surface OH or diffusing into the oxide can achieve a saturation concentration which is maintained even after the individual TPD experiments. Therefore, less hydrogen from MeOH decomposition can be adsorbed on or by the oxide and must desorb after the first TPD. Nevertheless, we have to point out that the subsequent TPD spectra still indicate that a small amount of H is missing according to the yield estimation. Some of the H may diffuse into the Pt substrate, some may form the background H₂ desorption signal during sample annealing to 800 K which is not accounted for by integrating the coherent H₂ desorption peak for the yield estimation.

We also conducted LEED experiments before and after the MeOH TPD experiments on the Sm₂O₃ thin film to learn if the film structure is affected by the MeOH reaction. Before we carried out TPD experiments on the film, the LEED pattern exhibits Sm₂O₃ main spots, weak Pt(111) spots and faint quasi-3 × 3 spots which originate from the coincidence lattice formed at the Sm₂O₃(111)-Pt(111) interface, as discussed in the experimental section. After the TPD experiments structural changes are indicated by the diffraction pattern. The quasi-3 × 3 spots become blurry and only the main spots from SmO_x(111) can be observed. Since the quasi-3 × 3 pattern requires sufficiently large coincidence areas of the Sm₂O₃(111) and Pt(111) lattices, the disappearance of the quasi-3 × 3 pattern suggests that the surface structure of the 2.8 ML as-prepared Sm₂O₃ film changes during the TPD experiments, resulting in a loss of order of the coincidence lattice. This structural change is caused by the MeOH reaction, generating further defects/vacancies in the surface, and not simply by the sample heating during the desorption experiments. A test experiment during which we simply annealed an as-prepared Sm₂O₃ thin film from 100 to 800 K in UHV several times with a well-controlled heating rate of 1 K/s resulted in no visible changes of the diffraction pattern.

3.3. Reduced and Re-Oxidized Continuous Sm₂O₃ Film

In a previous structural study of SmO_x thin films on Pt(111) we showed that reduction/reoxidation treatments can alter their surface structure [13]. To obtain insight into correlations of structural and chemical properties of SmO_x thin films, it is instructive to study if and how reduction and reoxidation affect the film's chemical properties. Hence, we thermally reduced the 2.8 ML as-prepared Sm₂O₃ film after the repeated MeOH TPD experiments by annealing in UHV at 1000 K for 30 min. The same treatment was utilized in our previous work [13] and in studies on ceria thin films [32,33]. Annealing of a Sm₂O₃ film to 1000 K in UHV can partially reduce the film and generate SmO (100) domains [13].

XPS was used to characterize the films before and after the annealing. Both O 1s and Sm 3d photoemission peaks (see Figure S1 in the Supplementary Information for the XPS data) shift to higher binding energies by 1.0 eV after the thermal reduction. These shifts cannot only be chemical shifts but represent a band bending effect as reported by other XPS studies [34]. A band bending can occur

when the electronic structure of the crystalline film surface or the interface between the film and a metallic substrate changes [35], e.g., caused by defect/vacancy formation or SmO formation located on the Sm₂O₃ film or at its interface to the Pt(111) substrate which may produce new electronic surface or interface states within the samaria band gap. It is not possible to deduce from our data the origin of the observed band bending. We take the observed shift in the spectra as an indication for the reduction of the oxide film.

After the reduction treatment, repeated TPD experiments were conducted on the reduced SmO_x thin film. The results are summarized in Figure 3a. In the first TPD spectrum, relatively small amounts of products are observed compared to the 2.8 ML as-prepared film. Two CO desorption peaks appear at 550 and 680 K as well as a tiny H₂ peak at 690 K. CO₂ is also observed in this temperature range. Only 0.12 ± 0.01 MLE MeOH react on the reduced film, which is less than half of the reaction yield observed for the as-prepared film. Again, neither MeOH recombination nor H₂O or CH₂O desorption are observed. Less CO₂ (0.04 ± 0.01 MLE) is produced from the MeOH reaction on the reduced SmO_x film as compared to the as-prepared Sm₂O₃ film in the first TPD run, confirming that less “active” oxygen (surface OH and/or lattice oxygen) is available on the reduced film for CO₂ formation. Reaction on the reduced SmO_x gives rise to new desorption peaks of CO (and CO₂) at 680 K and H₂ at 690 K, which appear at higher temperatures than those observed on the as-prepared Sm₂O₃ thin film. These new desorption peaks indicate that oxide reduction causes the binding between methoxy and the SmO_x surface to strengthen, most likely due to surface defect/vacancy formation, as we also concluded for the as-prepared Sm₂O₃ thin films after repeated TPD runs. This interpretation is supported by IRRAS data discussed below. The changes observed in the MeOH-TPD spectra after reducing the Sm₂O₃ film reveal that the MeOH reaction on SmO_x surface is affected strongly by the film conditions.

Compared to the first TPD traces, both the CO and H₂ features are significantly different in the second TPD spectra. Instead of two CO peaks, a broad feature is observed in the second spectrum. Additionally, a broad H₂ TPD feature appears in the same temperature range between 500 K and 700 K. The complex structure of the TPD features may reflect desorption of products from several different sites at or close to defects/vacancies in the oxide surface. The CO₂ TPD feature does not change much during the second TPD experiment, only its intensity slightly decreases. During further TPD runs, the features of CO, CO₂ and H₂ desorption peaks do not change significantly. At least two peaks of each product are observed and both peaks slightly downshift to lower temperatures by 15 K from the second TPD to the fourth TPD. The yields of CO and H₂ increase after the first TPD, but remain constant after the second TPD run, whereas the yield of CO₂ continuously decreases after the first TPD. Similar behavior was also observed on the as-prepared Sm₂O₃ thin film as discussed above. Although the CO₂ yield decreases after the first TPD, a minimum amount of CO₂ is always detectable in TPD spectra recorded from SmO_x surfaces, indicating replenishment of minor amounts of “active” oxygen after each TPD experiment which may be linked to the reaction of CO with surface OH groups. During sample cooling to 96 K before each subsequent TPD experiment, a small amount of background H₂O is probably adsorbed forming OH on the SmO_x surface, *i.e.*, the background pressure of H₂O may provide a minimum amount of OH on the SmO_x surface available for producing CO₂.

LEED results obtained from the reduced thin film are shown in Figure 3b. Before TPD experiments, the LEED pattern of the reduced SmO_x film exhibits SmO_x main spots, quasi-3 × 3 spots, and

$(2\sqrt{3} \times 2\sqrt{3})R30^\circ$ spots. The $(2\sqrt{3} \times 2\sqrt{3})R30^\circ$ pattern was not observed in our previous study, and may correspond to ordered oxygen vacancies or yet unidentified SmO_x structures. We are not able to make a clear assignment at this stage and further structural studies are necessary. After TPD experiments there is no significant change in the LEED pattern, in contrast to what we observed with the as-prepared Sm_2O_3 film, suggesting that the long range order of the reduced SmO_x film is not significantly affected by the MeOH reaction. However, we cannot exclude that the MeOH reaction induces some structural change at the surface of reduced SmO_x films, considering that the TPD spectra show slight changes over the repeated TPD experiments.

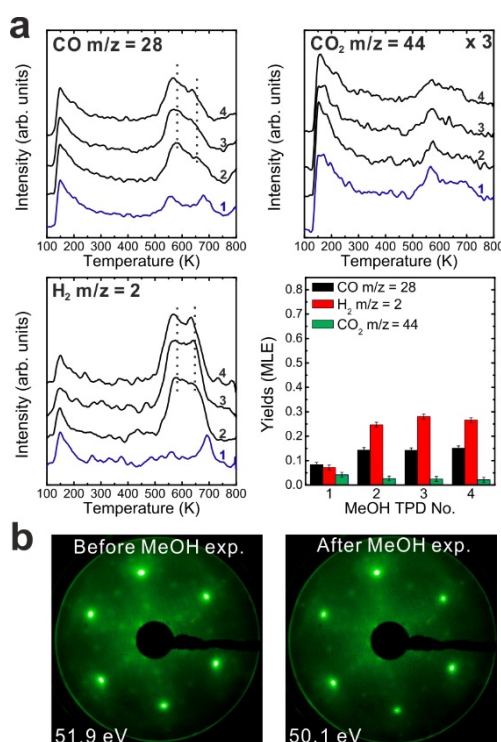


Figure 3. (a) Repeated TPD series on a 2.8 ML SmO_x film after a treatment of thermal reduction and the estimated yields of products, and (b) LEED results before and after the repeated MeOH TPD experiments.

Subsequent to the reduction treatment of the as-prepared Sm_2O_3 film and the TPD experiments performed thereafter, we carried out a reoxidation treatment in order to determine whether a full reduction-reoxidation cycle can restore the chemical activity of the as-prepared film. As shown in our previous study, the reduced SmO_x film can be reoxidized by thermal annealing in molecular oxygen [13]. Here reoxidation of the 2.8 ML reduced SmO_x film was performed by annealing the film in an O_2 background ($P = 5 \times 10^{-7}$ mbar) at 1000 K for 10 min. After annealing in oxygen, both Sm 3d and O 1s peaks in XPS spectra (shown in Figure S1) shifted back by 1.0 eV toward lower binding energies indicating reoxidation. Figure 4a shows the first and second MeOH TPD spectra of the reoxidized film. Surprisingly, small amounts of CH_2O and H_2O are observed as products. Also CO, CO_2 and H_2 are observed with an identical desorption maximum at 550 K.

Figure 4b shows TPD spectra collected from repeated MeOH TPD experiments. After the first TPD experiment, the intensities of CO and H_2 peaks increase, whereas the intensity of the CO_2 peak

slightly decreases in the second TPD spectrum. After the second TPD experiment, no CH_2O and H_2O can be detected. The CO , CO_2 and H_2 TPD features are similar to the TPD features which we observed from the reduced film, showing a broad feature between 550 and 700 K in the rest of TPD spectra. These results indicate that the reoxidation process does not restore the chemical behavior of the 2.8 ML as-prepared film but generates some oxygen species on or in the film which specifically promotes CH_2O and H_2O formation during the first and second TPD experiments. The CH_2O formation suggests incomplete MeOH dehydrogenation. Moreover, the formation of formaldehyde requires both, weak acidic and basic sites on the reoxidized SmO_x surface in order to limit C-H bond breaking and prevent strong adsorption of CH_2O on the surface. We, therefore, propose two possible explanations for this observation: first, a special oxygen species such as, e.g., superoxide (O_2^-) may form on the SmO_x surface by reoxidation. Such oxygen species have been found and identified on other oxides. For instance, it has been investigated for CeO_x by electron spin resonance (ESR), Raman, and IR spectroscopy [36–38]. These oxygen species act as weaker basic sites than lattice oxygen for nearby methoxy species and might be able to break one C-H bond but not promote further dehydrogenation. Instead, these oxygen species might form OH groups reacting with adjacent OH and leaving the oxide surface as H_2O at the same desorption temperature as formaldehyde. Second, the reoxidation process could improve the flatness of the film resulting in less surface defects, meaning an increase of coordinating numbers of both Sm cations and O anions. Ideally, the CO formation requires four available undercoordinated O anions to dehydrogenate one MeOH molecule via OH formation. An increase of the coordination number of a large fraction of surface O anions could therefore lead to incomplete MeOH dehydrogenation to CH_2O [18,19].

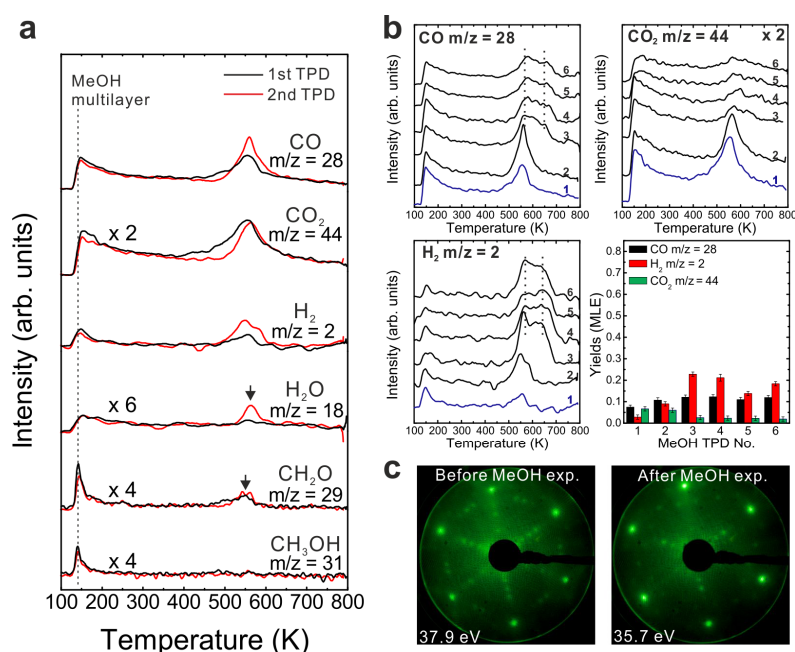


Figure 4. (a) The first and second TPD spectra collected from a 2.8 ML SmO_x thin film after the treatment of reoxidation, and (b) the repeated TPD series collected on the same sample and the estimated yields of products, and (c) LEED results before and after the repeated MeOH TPD experiments.

Overall, the variation of results observed by TPD for as-prepared, reduced, and reoxidized SmO_x films indicates that the chemical properties of the SmO_x surface can be tuned by reduction and oxidation procedures.

LEED results of the reoxidized film before and after MeOH TPD are shown in Figure 4c. Before the TPD experiments, the LEED pattern of the reoxidized SmO_x film shows Sm_2O_3 main spots, weak Pt spots, quasi- 3×3 spots, and additional 2×2 spots with respect to the Sm_2O_3 main spots. The additional 2×2 spots confirm that the surface structure of the as-prepared Sm_2O_3 film is not perfectly restored by the reoxidation treatment. The origin of the 2×2 superstructure may be a regular pattern of the proposed special oxygen species located at certain lattice positions or certain oxygen-vacancy ordering but requires further investigation. Over the TPD experiments, the same pattern consisting of SmO_x main spots + quasi- 3×3 and $(2\sqrt{3} \times 2\sqrt{3})R30^\circ$ spots was found for the reduced 2.8 ML SmO_x film both before and after repeated MeOH TPD experiments. It strongly suggests that, after repeated MeOH TPD runs, the reoxidized film ends up at a similar structural condition as the reduced film, which is consistent with what we observe in TPD—reactions on the reoxidized film gives rise to similar TPD features as observed from the reduced film after the second TPD experiment. Overall, both LEED and TPD results suggest that the reoxidation indeed generates oxygen species on/in the 2.8 ML reduced film but does not restore the film to the exact same structure and chemical behavior as the as-prepared one.

3.4. As-Prepared Sm_2O_3 Islands on Pt(111)

MeOH TPD spectra obtained from an as-prepared $0.9 (\pm 0.1)$ ML Sm_2O_3 film on Pt(111) shows, in contrast to the 2.8 ML SmO_x deposit, both MeOH multilayer and monolayer desorption at 140 and 180 K, respectively (Figure 5a). The presence of a strong MeOH monolayer signal indicates that the Pt(111) surface is not fully covered by the Sm_2O_3 thin film because the molecular desorption of MeOH from a monolayer is expected mainly for Pt(111). By estimating the yield of the MeOH monolayer we determine that only ~50% of the Pt(111) surface is covered by the as-prepared Sm_2O_3 thin film. More details regarding this estimation will be discussed below in Section 3.6. Also, the TPD spectra exhibit both the H_2 peak and the CO peak typical for a Pt(111) surface, providing further evidence that there are uncovered Pt areas. Compared to the 1st TPD spectrum obtained from clean Pt(111), the H_2 TPD peak at 315 K is smaller whereas the CO peak at 420 K is larger for the 0.9 ML Sm_2O_3 deposit on Pt(111). In the following, these two peaks are named the Pt-related H_2 peak and the Pt-related CO peak, respectively. The corresponding H_2 and CO yields are 0.05 ± 0.01 MLE and 0.12 ± 0.01 MLE, respectively. In comparison to the yields obtained during MeOH TPD on a clean Pt(111) surface (0.07 ± 0.01 MLE of H_2 and 0.04 ± 0.01 MLE of CO, as mentioned above), we observe three times more Pt-related CO produced on Pt(111) partially covered by Sm_2O_3 , suggesting a cooperative-effect between SmO_x and Pt, possibly via adsorption sites at the boundary of the SmO_x islands at the interface to the Pt substrate. The amount of Pt-related CO suggests that 0.24 MLE H_2 should be produced in the balance, but we only observed 0.05 MLE Pt-related H_2 which indicates that a considerable amount of H remains on and/or diffuses into the sample at this temperature.

The H_2 and CO desorption peaks that appear at higher temperatures (450–600 K) have no analog in MeOH TPD spectra obtained from bare Pt(111) and must, therefore, be contributions from the SmO_x surface. Both the SmO_x -related H_2 peak and the CO peak are relatively broad TPD features with an

identical position of their maximum at 515 K. Additionally, there is a broad H₂ feature in the region of 400–450 K which is not observed in the case of the 2.8 ML SmO_x thin film. Its desorption maximum is at a temperature close to that of the Pt-related CO peak. Since we do not observe this H₂ peak in the MeOH TPD spectra collected from clean Pt(111), we conclude that this H₂ peak is contributed by the SmO_x-Pt interface at the surface, *i.e.*, the boundary of SmO_x islands where adjacent SmO_x and Pt surface sites exist. As observed in TPD results from the 2.8 ML film, H missing in the balance is also seen for the SmO_x-related H₂ and CO peaks on the 0.9 ML as-prepared Sm₂O₃/Pt(111) system, especially in the first TPD experiment suggesting, as discussed before, OH formation at the surface and/or H diffusion into the sample. According to the yield estimation from both first TPD results, there is a total deficit (sum over Pt- and SmO_x-related TPD peaks) of 0.54 MLE H in desorption from the 0.9 ML Sm₂O₃ film, which is half the amount of the missing H in the balance of MeOH TPD on the continuous 2.8 ML Sm₂O₃ film, in good correlation with the ratio of the respective surface area covered by Sm₂O₃. The result suggests that the Pt(111) substrate does not play a predominant role for storing the missing H. A relatively small CO₂ peak appears as a broad feature in the temperature range of 350–600 K in the MeOH TPD spectra obtained from the 0.9 ML as-prepared Sm₂O₃ film. Compared to 0.14 MLE of CO₂ produced from the as-prepared continuous Sm₂O₃ film in the first TPD, only 0.04 MLE of CO₂ are produced on the SmO_x islands on Pt(111), meaning that only ~30% of the amount of “active” oxygen on the continuous film must be available on the discontinuous film, in good accordance with the ratio of the total Sm₂O₃ coverages of both samples (0.9:2.8).

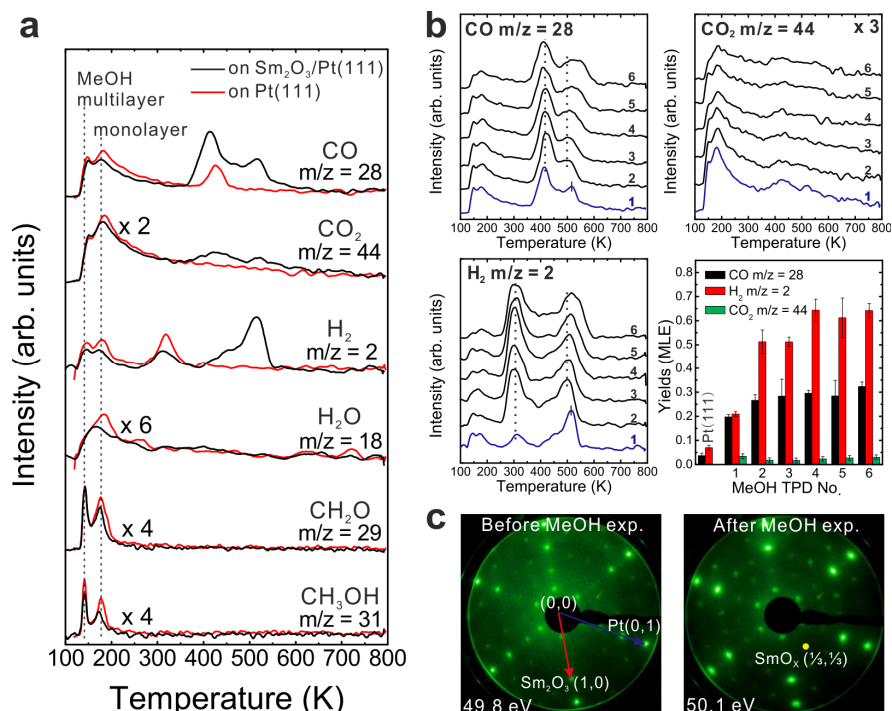


Figure 5. (a) The first TPD spectra collected from a clean Pt(111) surface and a 0.9 ML as-prepared Sm₂O₃/Pt(111) surface, (b) repeated TPD series collected on the as-prepared Sm₂O₃/Pt(111) surface and the estimated yields of products, and (c) LEED results before and after the repeated MeOH TPD experiments.

The results of repeated MeOH TPD experiments on the 0.9 ML as-prepared film are shown in Figure 5b. There is a clear difference in TPD features between the 1st and the subsequent TPD spectra. After the 1st TPD experiment, the intensity of the Pt-related H₂ peak increases dramatically and the intensity of the Pt-related CO peak increases slightly as well, whereas the intensity of the CO₂ peak decreases. Now, both the Pt-related CO and H₂ peaks exhibit much higher intensities than those observed from bare Pt(111). The result suggests that a fraction of the methoxy species adsorbed on SmO_x dehydrogenate to H and CO which spill over to the exposed Pt surface below 300 K and afterwards desorb from Pt as H₂ and CO at temperatures near 300 and 400 K, respectively. Another fraction of the methoxy species, however, remains on the SmO_x surface until, eventually, producing the SmO_x-related H₂ and CO TPD peaks at higher temperatures. This interpretation is supported by our IRRAS results in the following section. The Pt-related and SmO_x-related TPD peaks behave differently during repeated TPD experiments. The SmO_x-related H₂ and CO peaks become broader and shift to higher temperature by 30 K from the 2nd TPD to the sixth TPD experiment, as was also observed for the 2.8 ML film, whereas the Pt-related H₂ and CO peaks remain at the same temperature without significant changes of their features. These different characteristics reflect that the SmO_x film is altered during repeated methoxy dehydrogenation while the Pt surface remains unchanged.

From the yield estimation we learn that the reactivity of the 0.9 ML film slightly increases after the 1st TPD experiment. The H₂ yield increases by more than a factor of two and the CO yield also slightly increases after the first TPD experiment by a factor of 1.3, and the average ratio of [H₂]/{[CO]+[CO₂]} is estimated as 1.9. Background H₂ desorption during sample heating to 800 K during TPD might account for the small amount of missing H in the balance calculation, as we discussed before. The yield estimation shows that after repeated TPD runs, the Sm₂O₃ islands on Pt(111) also exhibit much higher reactivity for MeOH decomposition than the continuous SmO_x film or the bare Pt(111) surface. The average yield of decomposed MeOH is 0.31 ± 0.03 MLE compared to 0.21 ± 0.01 MLE from the 2.8 ML film and 0.04 ± 0.01 MLE from the the Pt(111) surface, respectively. The continuously higher overall reactivity of the 0.9 ML Sm₂O₃/Pt(111) film implies that the cooperative effect between SmO_x and Pt is robust with respect to the changes that repeated MeOH decomposition induces in the SmO_x islands.

The LEED results shown in Figure 5c provide evidence that the 0.9 ML Sm₂O₃ layer undergoes structural changes during the repeated MeOH TPD experiments. Before the TPD experiments, the LEED pattern of the sample with SmO_x islands on Pt(111) exhibits sharp and clear Sm₂O₃ main spots, Pt spots, and quasi-3 × 3 spots. After the TPD experiments, the latter are slightly rotated and additional spots are observed. One of these additional spots is labeled in Figure 5c, and is located at the (1/3, 1/3) position in registry with Sm₂O₃ main spots. Apparently, SmO_x domains slightly rotate against the Pt substrate during the repeated TPD experiments. Moreover, the appearance of the additional spots suggests that the Sm-Sm lattice constant slightly decreases, possibly due to surface defects/vacancies formation and, therefore, the quasi-3 × 3 structure transforms into a (3 × 3) structure. In summary, the film composed of Sm₂O₃ islands on Pt(111) exhibits a higher reactivity than both the continuous Sm₂O₃ thin film and the bare Pt(111) surface. From the TPD results, the contributions of both Pt and SmO_x surface areas to the MeOH reaction can be identified by monitoring the Pt-related and the SmO_x-related TPD peaks. The SmO_x surface properties are changed by the MeOH reaction for the 0.9 ML and the 2.8 ML thick films.

In contrast, the Pt substrate is not affected, as the behavior of SmO_x - and Pt-related TPD features during repeated experiments shows.

To extend the understanding of MeOH adsorption and reaction on the $\text{SmO}_x/\text{Pt}(111)$ system, we also performed IRRAS studies in a different UHV chamber from that in which the TPD studies were conducted (as mentioned in the experimental section). For the IRRAS studies, we prepared a 0.7 ± 0.2 ML Sm_2O_3 thin film on Pt(111) and observe the same LEED pattern as that obtained from the 0.90 ± 0.01 ML $\text{Sm}_2\text{O}_3/\text{Pt}(111)$ surface used in TPD experiments. Therefore, we consider the film structure of these two samples as comparable. For the IRRAS experiments, 15 Langmuir of MeOH was dosed on the 0.7 ML as-prepared $\text{Sm}_2\text{O}_3/\text{Pt}(111)$ surface at 96 K. The elaborate procedure necessary to collect reliable temperature-dependent IRRAS data in our experiments (detailed in the experimental section) made it necessary to restrict the analysis to nearly static conditions of the $\text{SmO}_x/\text{Pt}(111)$ surface. Therefore, the temperature-dependent IRRAS spectra shown in Figure 6 were collected from the second MeOH reaction on the samples, because from the repeated TPD experiments we found that $\text{SmO}_x/\text{Pt}(111)$ surfaces show an almost static reactivity after the first MeOH TPD experiment. The IRRAS spectrum collected at 250 K reveals the existence of methoxy species (CH_3O^-) which is confirmed by the detection of $\nu(\text{C-O})$, $\nu(\text{CH}_3)$, and $\rho(\text{CH}_3)$ features. The $\nu(\text{C-O})$ peak is broad in the range between 1100 and 1000 cm^{-1} , and both $\nu_s(\text{CH}_3)$ and $\nu_{\text{as}}(\text{CH}_3)$ peaks are observed at 2790 and 2926 cm^{-1} , respectively. Moreover, the $\rho(\text{CH}_3)$ peak is evident at 1140 cm^{-1} . The absence of a $\nu(\text{OH})$ signal at 3280 cm^{-1} implies that the O-H bond of methanol breaks. The $\nu(\text{CH}_3)$ frequency is relatively low (*ca.* 2800 cm^{-1}) from which a low electronegativity for the cationic site can be inferred, indicating that species resulting from the MeOH dehydrogenation are methoxy (CH_3O^-) located on top of Sm cations [39,40]. On the basis of TPD results, we speculated that a fraction of the H atoms from the MeOH dehydrogenation diffuses into the film or remains on the surface and forms surface hydroxide. The IRRAS results do not provide evidence for surface OH. It should be noted, however, that because of the small dynamic dipole moment and the adsorption geometry, surface OH on SmO_x is difficult to detect [38]. According to previous studies of MeOH adsorption and reaction on Pt(111) [20], methoxy species are not observed on a bare Pt(111) surface. Methoxy species can exist on an O-terminated Pt(111) surface on which they decompose at temperatures below 150 K. Therefore, we relate all methoxy species detected in the IRRAS spectra above 250 K to Sm_2O_3 surface sites.

After heating the sample to 250 K, two $\nu(\text{C-O})$ bands are identified as a sharp peak at 1080 cm^{-1} and a shoulder at 1042 cm^{-1} , revealing different adsorption sites for methoxy which can be identified by monitoring the $\nu(\text{C-O})$ frequencies as has been demonstrated in several studies [36,38,39]. If the coordination number of the oxygen atom in the methoxy group is increased from one (on-top site), to two (bridge site) and three (hollow site), the effective mass of this oxygen atom increases as well which leads to a decrease of the observed vibrational frequency for $\nu(\text{C-O})$. Therefore we speculate that the $\nu(\text{C-O})$ band at 1080 cm^{-1} corresponds to the type-I methoxy binding on one Sm cation (on-top), and the broad $\nu(\text{C-O})$ shoulder at lower frequency corresponds to the type-II and III methoxy species bound to two and three Sm cations (bridge and hollow sites). Since this speculation is only based on comparing our IRRAS results with previous IR studies of methoxy on ceria surfaces, theoretical and computational work for MeOH on samaria will be required for confirmation. Most likely, the binding strength between methoxy and the substrate varies for different adsorption sites on the SmO_x surface so that a multitude of

different adsorption sites is expected to lead to a broad range of desorption temperatures of SmO_x -related products in TPD spectra.

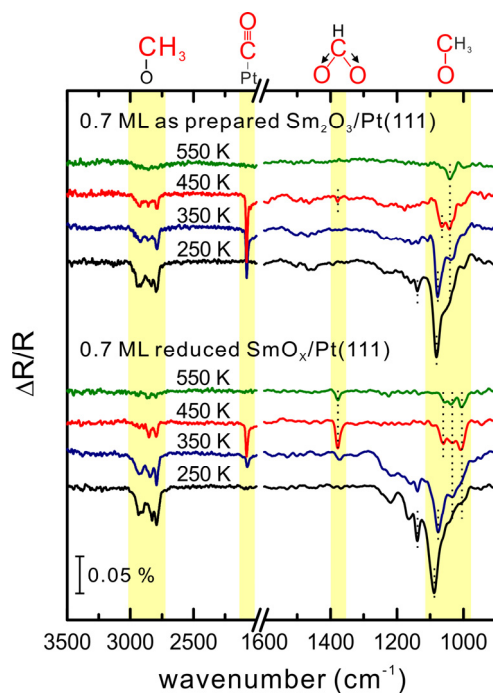


Figure 6. Temperature-dependent IRRAS spectra collected after dosing 15 Langmuir MeOH on a 0.7 ML as-prepared $\text{Sm}_2\text{O}_3/\text{Pt}(111)$ and its thermally-reduced $\text{SmO}_x/\text{Pt}(111)$ surfaces at 96 K and subsequently annealed to particular temperatures.

After heating to 350 K, both the $\nu(\text{C-O})$ and $\nu(\text{CH}_3)$ bands become smaller and the higher frequency $\nu(\text{C-O})$ feature slightly shifts from 1080 to 1077 cm^{-1} which may be due to a dilution effect whereas the lower frequency $\nu(\text{C-O})$ band remains at 1042 cm^{-1} . The $\nu(\text{C}\equiv\text{O})$ band observed at 2080 cm^{-1} originates from CO adsorbed on Pt(111). Comparing to TPD results, which showed Pt-related H_2 desorbing in the temperature range 250–350 K, the IR data reveal that the on-top methoxy species ($\nu(\text{C-O})$ at 1080 cm^{-1}) on SmO_x is the source for CO and H_2 formation on Pt(111) because the $\nu(\text{C-O})$ band at 1077–1080 cm^{-1} has almost vanished at 350 K while the $\nu(\text{C}\equiv\text{O})$ band at 2080 cm^{-1} has intensified. Obviously, the on-top methoxy species dehydrogenates near 250 K to H and CO, which spillover onto Pt in the temperature range 250–350 K. Hydrogen desorbs as H_2 from the Pt surface which we found in TPD as the Pt-related H_2 peak, whereas CO remains on the Pt surface in this temperature range.

In the spectrum obtained after sample heating to 450 K, the $\nu(\text{C-O})$ band at 1077 cm^{-1} (on-top methoxy species) has vanished completely. Instead, a $\nu(\text{C-O})$ peak at 1065 cm^{-1} is observed while the $\nu(\text{C-O})$ band at 1042 cm^{-1} remains unshifted. As mentioned before, we speculate that the $\nu(\text{C-O})$ peak at 1065 cm^{-1} and the peak at 1042 cm^{-1} correspond to type-II and III methoxy species on the bridge and hollow sites, respectively. Since the $\nu(\text{CH}_3)$ band has become smaller, less methoxy is present on the surface after heating to 450 K compared with 350 K. While the $\nu(\text{C}\equiv\text{O})$ band is still observed after heating to 450 K, a tiny $\nu_s(\text{OCO})$ band appears at 1378 cm^{-1} , the appearance of which suggests the existence of formate species on the Sm_2O_3 surface. Since the $\nu_{\text{as}}(\text{OCO})$ band expected at $\sim 1550 \text{ cm}^{-1}$ is not detected, the formate species must bind to SmO_x as bidentate (C_{2v} and $\text{C}_s(1)$). The $\nu_{\text{as}}(\text{OCO})$

of the bidentate species is not IR active due to the metal surface selection rule (MSSR) [41,42]. The appearance of formate species and CO can be connected to the transformation of methoxy species on the SmO_x surface. In summary, the decrease of intensity of the $\nu(\text{C-O})$ band, its downshift to 1077 cm^{-1} and disappearance at 450 K indicate turnover of the type-I methoxy species (on-top mode) to CO and H adsorbed on exposed Pt surface, as discussed before, and its transformation to formate on the SmO_x surface.

After the heating step to 550 K, only one small $\nu(\text{C-O})$ band at 1042 cm^{-1} is detected which, in our interpretation, reveals that only a small amount of the type-III methoxy has remained on the SmO_x surface. It should be noted, however, that no sign of the $\nu(\text{CH}_3)$ band is detected which we ascribe to limited sensitivity of IRRAS. In accordance, the TPD spectra show that above 550 K desorption of products is very limited (*cf.* Figure 5). In conclusion, the combined TPD and IRRAS results for MeOH interaction with SmO_x islands on Pt(111) show that the type-I methoxy species (on-top samarium) on the Sm_2O_3 surface dehydrogenates at temperatures above 250 K via two routes: (1) transformation to formate on the SmO_x surface. The formate species may be an intermediate and finally decompose to CO_2 upon further dehydrogenation or to CO while generating OH on the SmO_x surface. (2) Dehydrogenation to CO. The products H and CO spill over to the exposed Pt surface and lead to Pt-related H_2 and CO peaks in TPD at 300 and 400 K, respectively. Between 350 and 450 K, the type-I methoxy species fully dehydrogenates. The type-II and III methoxy species on the bridge and hollow sites on the Sm_2O_3 surface further dehydrogenate only at higher temperature above 450 K and contribute the SmO_x -related H_2 and CO peaks in TPD. The Pt-related H_2 and CO peaks are only contributed by the type-I methoxy species which exhibit less stability on the SmO_x surface compared to type-II and III methoxy species.

3.5. Reduced and Reoxidized SmO_x Islands on Pt(111)

The reduction and reoxidation treatment that was detailed before for the continuous Sm_2O_3 film on Pt(111), was also carried out with the SmO_x islands on Pt(111). IRRAS results collected from the reduced 0.7 ML SmO_x film on Pt(111) after heating the sample to 250 K (Figure 6) reveal a significant difference in the region of the $\nu(\text{C-O})$ bands compared to IRRAS from the as-prepared film. A broad absorption feature in the $\nu(\text{C-O})$ region appears for the reduced film, and the main $\nu(\text{C-O})$ band which we ascribe to the type-I methoxy species is observed at 1089 cm^{-1} instead of 1080 cm^{-1} , *i.e.*, shifted to higher frequency. As for the as-prepared film, the type-I methoxy band is smaller and down-shifted to 1077 cm^{-1} , after heating the reduced 0.7 ML SmO_x film to 350 K. Concomitantly, the $\nu(\text{C}\equiv\text{O})$ band at 2080 cm^{-1} as fingerprint for CO on Pt has appeared and suggests, as discussed for the as-prepared film, that H and CO produced from decomposition of type-I methoxy at above 250 K can spill over to the exposed Pt(111).

After heating the sample to 450 K, the $\nu(\text{C-O})$ band at $1089\text{--}1077\text{ cm}^{-1}$ has completely vanished. As for the 0.7 ML as-prepared Sm_2O_3 film, both $\nu(\text{C-O})$ fingerprints for type II and type III methoxy species are also observed in the IRRAS spectra from the reduced film, although downshifted by 5 cm^{-1} to 1061 and 1037 cm^{-1} , respectively. In addition, a new $\nu(\text{C-O})$ peak at 1005 cm^{-1} is observed which indicates a new adsorption site on the reduced surface for methoxy species (type IV). After heating the reduced film to 550 K, all three $\nu(\text{C-O})$ bands at 1061 , 1037 and 1005 cm^{-1} as well as a $\nu_s(\text{OCO})$ band are small, but still detectable, which is in contrast to the lack of bands observed for the as-prepared film.

This result suggests a stronger bonding of methoxy and formate species on the reduced film, probably because more defects/vacancies on the reduced surface are present and assist in stabilizing methoxy and formate species.

We also performed repeated MeOH TPD experiments on the reduced 0.9 ML $\text{SmO}_x/\text{Pt}(111)$ system. Reduction of the oxide was verified by XPS as indicated by shifts of the Sm 3d and O 1s peaks to higher binding energies (shown in Figure S2) that we attribute to a band bending effect as observed on the 2.8 ML reduced film. The TPD spectra recorded from the reduced $\text{SmO}_x/\text{Pt}(111)$ shown in Figure 7a significantly differ from the ones recorded for the as-prepared film. The Pt-related CO and H_2 peaks can be hardly discerned in the 1st TPD run. Our previous STM studies demonstrated that upper Sm_2O_3 layers from the samaria islands spread onto bare Pt areas during the thermal treatment of the sample for reduction. As a result, less Pt surface is exposed as indicated by the smaller amount of Pt-related CO and H_2 desorption. While small, the Pt-related H_2 and CO TPD signals have not shifted with respect to temperature after thermal reduction of the oxide film, even after repeated TPS experiments. This finding is consistent with the assumption based on the IRRAS experiments that the on-top methoxy species dehydrogenates to H and CO which spill over to the exposed Pt surface and desorb from there as H_2 and CO at 300 and 400 K, respectively.

One clear H_2 peak appears near 400 K, *i.e.*, the temperature of the Pt-related CO peak. That hydrogen is, as discussed for the 0.9 ML as-prepared film, probably contributed by sites at the boundary of SmO_x islands, *i.e.*, the SmO_x -Pt interface at the surface. For the reduced film, the intensity of the H_2 peak at 400 K is larger than that of the Pt-related H_2 peak at 300 K which indicates that while the area of exposed Pt surface decreased during thermal reduction, the total length of the SmO_x island boundaries increased. This interpretation is consistent with the wetting of a reduced SmO_x film on Pt(111) observed in our previous STM work [13]. Over repeated TPD runs, the H_2 peak that we relate to the SmO_x island boundaries remains at a temperature of 400 K which suggests that the reaction and spillover mechanisms at the SmO_x -Pt boundary on the surface do not change by the MeOH reaction and its effects on structure. The maxima of the SmO_x -related CO and H_2 desorption peaks are observed at an identical temperature of 600 K in the 1st TPD experiment with the reduced 0.9 ML $\text{Sm}_2\text{O}_3/\text{Pt}(111)$ sample which is higher than that observed on the as-prepared film. The same trend was observed when as-prepared and reduced continuous SmO_x films were compared. As discussed before, thermal reduction creates new adsorption sites for methoxy ($\nu(\text{C}-\text{O})$ band at 1005 cm^{-1} in IRRAS) on the SmO_x surface which may cause a stronger binding between the methoxy species and SmO_x and, thereby, higher desorption temperatures of the decomposition products.

Over repeated TPD runs, the SmO_x -related peaks shift to lower temperatures, *e.g.*, the CO peak shifts from 600 K in the 1st TPD trace to 560 K in the 4th TPD trace. The average $[\text{H}_2]/\{[\text{CO}]+[\text{CO}_2]\}$ ratio from 2nd to the 4th TPD is 2.38, *i.e.*, significantly larger than 2, the value expected from stoichiometry. The yield calculation suggests that 0.04 MLE C and O are missing in each TPD run, *i.e.*, 0.04 MLE oxygen remains on the reduced film and may slightly reoxidize it while 0.04 MLE carbon are also deposited on the surface. Slight reoxidation of the SmO_x surface should reduce the number of surface defects/oxygen vacancies and can therefore explain the observed shift of SmO_x -related TPD peaks to lower temperature upon repeated experiments. In the fourth TPD experiment, both SmO_x -related CO and H_2 peaks have shifted to about 550 K which is close to the temperature observed on the as-prepared

0.9 ML $\text{Sm}_2\text{O}_3/\text{Pt}(111)$ sample in the sixth TPD experiment. Apparently, both the as-prepared and the reduced 0.9 ML SmO_x films approach the same equilibrium condition during repeated MeOH TPD experiments.

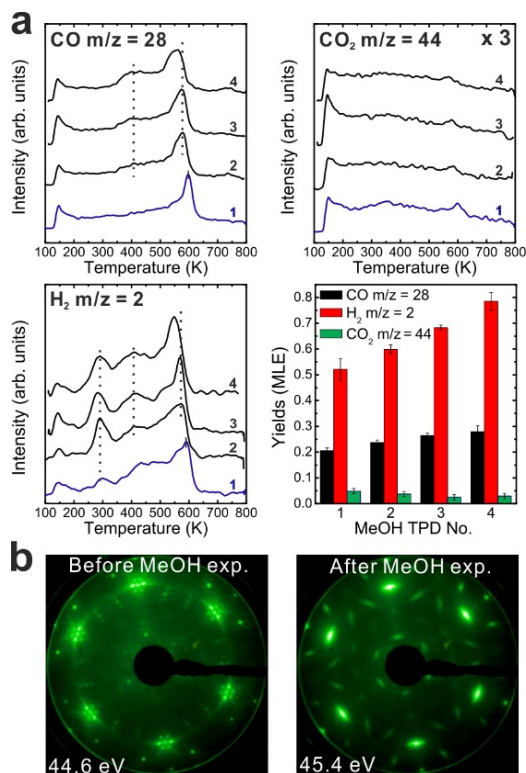


Figure 7. (a) Repeated TPD series collected on a 0.9 ML $\text{SmO}_x/\text{Pt}(111)$ surface after the treatment of thermal reduction and the estimated yields of products, and (b) LEED results before and after the repeated MeOH TPD experiments.

Structural information on the reduced 0.9 ML $\text{SmO}_x/\text{Pt}(111)$ sample was obtained using LEED, as shown in Figure 7b. Before the TPD experiments, a complicated satellite structure is observed which has been published in our previous work [13]. The satellite structure may be due to the coexistence of Sm_2O_3 (111) and SmO (100) domains and the formation of their coincidence lattice. After the TPD experiments, the LEED pattern exhibits a clear “rotated” structure which could be due to the coexistence of SmO_x domains with different rotational mismatches between SmO_x (111) trilayers and the Pt substrate. If there are multiple rotation angles, it is expected that the quasi- 3×3 spots (which are due to double diffractions) are elongated because they are involved in different scattering vectors. Ritter *et al.*, have observed a similar rotated LEED pattern due to rotational mismatches between FeO (111) layers and a $\text{Pt}(111)$ substrate [43]. Therefore, we assume that rotational mismatches between SmO_x domains and the $\text{Pt}(111)$ substrate are also responsible for the observed pattern. Moreover, the disappearance of the satellite structure indicates that SmO (100) vanishes after MeOH partially oxidizes the film.

A reoxidation treatment of the reduced 0.9 ML $\text{SmO}_x/\text{Pt}(111)$ sample was carried out by annealing in O_2 ($P = 5 \times 10^{-7}$ mbar) at 1000 K for 10 min. (XPS spectra of the reoxidized sample are shown in Figure S2). The results of repeated MeOH TPD experiments performed on the reoxidized film

are shown in Figure 8a. In contrast to our observations for the continuous SmO_x film, reoxidation of reduced SmO_x islands on Pt(111) leads to MeOH TPD spectra that are very similar to those observed for the as-prepared 0.9 ML $\text{Sm}_2\text{O}_3/\text{Pt}(111)$ sample, *i.e.*, the chemical behavior of the as-prepared film is completely restored. This also holds for repeated TPD experiments. The result indicates that the reoxidation procedure (exposure of a film surface to molecular oxygen at elevated temperatures) is more efficient for a film surface than for bulk sites in the film. Therefore the 0.9 ML thin film, wetting the Pt surface after reduction and exhibiting only surface sites, would be restored more easily than the thicker (2.8 ML) reduced film. The Pt-related H_2 and CO peaks have the same intensity as observed before the reduction-reoxidation cycle, indicating that the reoxidized Sm_2O_3 thin film dewets the Pt(111) substrate after the treatment, which is consistent with our finding in the previous STM work [13]. In that work, we demonstrated that the Sm_2O_3 (111) crystal structure is completely restored by the reoxidation treatment. However, in contrast to TPD, the LEED results obtained from the 0.9 ML reoxidized sample (Figure 8b) slightly differ from those obtained for an as-prepared film. Before the TPD experiments, there is a quasi- 3×3 LEED pattern and two additional spots adjacent to the Sm_2O_3 (111) main spots. The additional spots may be caused by differently reoxidized Sm_2O_3 domains rotated by small angles or to surface areas that are still reduced, indicating that the film is not completely restored to its initial state. After the MeOH TPD experiments, the two additional spots adjacent to the Sm_2O_3 (111) main spots still remain and dim $(2\sqrt{3} \times 2\sqrt{3})R30^\circ$ spots appear, obviously due to structural changes induced by the MeOH reaction. To resolve the origin of the $(2\sqrt{3} \times 2\sqrt{3})R30^\circ$ structure, also observed on the 2.8 ML reduced film, further investigation is required. To sum up the results obtained upon reducing and reoxidizing the 0.9 ML $\text{SmO}_x/\text{Pt}(111)$ system, we found that the reduced film can be partially oxidized by MeOH during the repeated TPD runs and that, judging by the MeOH TPD experiments, the chemical behavior of an as-prepared 0.9 ML Sm_2O_3 film on Pt(111) is restored to the initial condition by a cycle of reduction and reoxidation treatments.

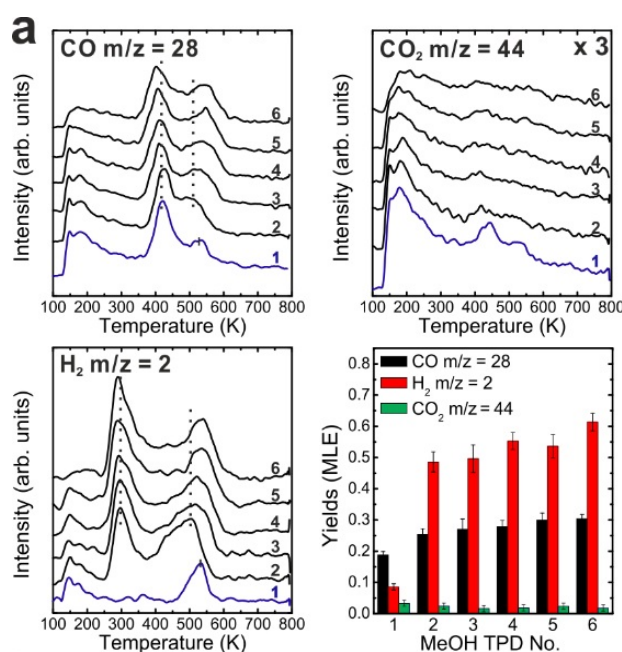


Figure 8. Cont.

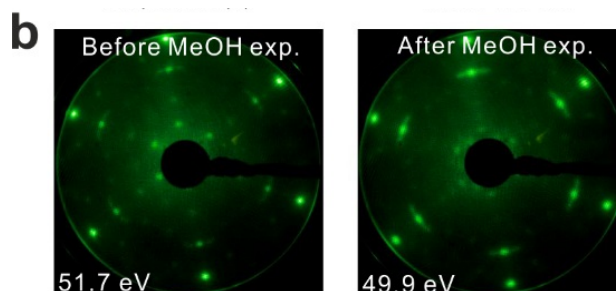


Figure 8. (a) Repeated TPD series collected on a 0.9 ML $\text{SmO}_x/\text{Pt}(111)$ surface after the treatment of reoxidation and the estimated yields of products, and (b) LEED results before and after the repeated MeOH TPD experiments.

3.6. Discussion

Our results demonstrate that SmO_x thin films exhibit a very high activity toward MeOH decomposition. We also find that MeOH decomposition on SmO_x thin films induces structural changes in the film that modify the film's chemical reactivity towards MeOH, and *vice versa*. There are several studies showing how the structural properties of ceria can affect the surface reactivity toward MeOH. For instance, the observation that a reduced $\text{CeO}_x(111)$ surface exhibits higher reactivity than a fully oxidized $\text{CeO}_2(111)$ surface [18,19] was ascribed to the different coordination environment of surface Ce cations and O anions on these two surfaces. On the fully oxidized $\text{CeO}_2(111)$ surface, each top-layer O atom is coordinated to three Ce cations. Therefore, under-coordinated sites required for dehydrogenating MeOH [18,19] are lacking on this surface resulting in minor reactivity. Reduction of the $\text{CeO}_2(111)$ surface generates defect sites (O vacancies) which are responsible to the methoxy adsorption [44,45]. In accordance, the reduced $\text{CeO}_x(111)$ surface shows a higher reactivity than does the $\text{CeO}_2(111)$ surface. In contrast to Sm_2O_3 , CeO_2 exhibits a fluorite structure with both Ce and O ions adopting a hexagonal lattice within the (111) surface. Surface vacancies can be generated by reducing $\text{CeO}_2(111)$ to $\text{CeO}_x(111)$ ($1.5 < x < 2$), and different defect structures such as, e.g., a triangular superlattice of surface and subsurface oxygen vacancies have been demonstrated by SPM [44–46]. We have learned from our previous STM work that a Sm_2O_3 thin film grows on Pt(111) in a defective fluorite structure but does not form the bixbyite structure prevalent in bulk Sm_2O_3 [13]. The Sm cations at the surface are located in a hexagonal lattice whereas O anions are randomly distributed within a hexagonal lattice, resulting in plentiful vacancies/defects on the surface. Therefore, and since we have also observed a defect structure with a triangular superlattice in previous STM work, we consider the reaction of MeOH at the fluorite-related $\text{Sm}_2\text{O}_3(111)$ thin film and a reduced $\text{CeO}_x(111)$ surface as comparable, and interpret the high activity of the SmO_x thin film surface for MeOH dehydrogenation as due to the existence of abundant vacancies/defects on the surface.

A summary of our LEED results from the SmO_x films on Pt(111) which provide evidence for even long-range structural changes within the films induced by MeOH is provided in the Figure S3 and Table S1. These structural changes are most likely connected to the MeOH capability of reducing or oxidizing SmO_x thin films, depending on their initial oxidation state. *Vice versa*, the surface structure of the SmO_x thin films does affect their chemical behavior and the reaction of MeOH on these films. Our

IRRAS data reveal that on a reduced SmO_x surface new adsorption sites can exist which are not observed on an oxidized surface. As a result, methoxy species can bind on these sites strongly and remain on the reduced surface up to higher temperatures than those on the oxidized surface.

Apart from indications for changed oxygen vacancy densities at the surface induced by MeOH, our experiments on films of SmO_x islands on Pt(111) also provide evidence for significant material transport involved in the structural changes related to the film's wetting/dewetting behavior which is demonstrated by our TPD results. (It may be interesting to note that wetting/dewetting induced by structural changes of the oxide was also observed for gold on ceria [47], which, inversely, is a metal-on-rare earth oxide system). Since the molecular desorption of MeOH is mainly contributed by the Pt(111) surface, the MeOH desorption yield during a TPD experiment is a good measure of the exposed Pt surface area, in particular for the 0.9 ML $\text{SmO}_x/\text{Pt}(111)$ samples. Akhter and White calculated the saturation monolayer coverage of MeOH and the maximum amount of reacted MeOH on a Pt(111) surface from their TPD experiments as 0.36 and 0.047 MLE, respectively [20]. Our calibration yields 0.04 ± 0.01 MLE MeOH reacting on the Pt(111) surface and 0.32 MLE intact MeOH desorbing from the Pt(111) surface which corresponds to the MeOH monolayer peak at 180 K. Following the same method, we determined that 0.08 ± 0.02 MLE of intact MeOH desorbs from the 2.8 ML Sm_2O_3 surface which is expected to exhibit no exposed Pt surface. Hence, we use a linear combination of the ratios of intact MeOH yield to total MeOH yield observed for bare Pt(111) and bare Sm_2O_3 (111) to estimate the exposed Pt area (%) on the 0.9 ML $\text{SmO}_x/\text{Pt}(111)$ samples as shown in Figure 9. About half of the Pt(111) surface is covered by the 0.9 ML as-prepared Sm_2O_3 thin film before the first TPD measurement which indicates that the film consists almost entirely of two-trilayer thick islands (one trilayer denoting an O-Sm-O layer). During repeated MeOH TPD runs, the exposed Pt area continuously decreases to ~20% of the surface by spreading of the SmO_x over the Pt(111) surface. An 80% surface coverage with 0.9 ML SmO_x can be only obtained when the film structure changes from two-trilayer high islands to almost entirely one-trilayer high islands.

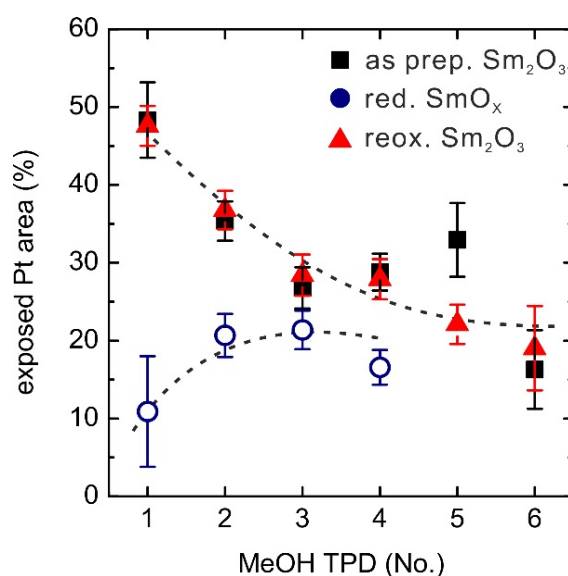


Figure 9. Changes of exposed Pt areas (%) on the 0.9 ML $\text{SmO}_x/\text{Pt}(111)$ samples over repeated TPD experiments. The dashed lines are added as a guide to the eye.

The reduced SmO_x film only exhibits ~10% exposed Pt surface before the first TPD experiment, meaning that ~90% Pt(111) surface is covered by the reduced SmO_x thin film. As discovered in our previous STM work, a fraction of the Sm_2O_3 reduces to SmO at the interface between Pt(111) and Sm_2O_3 (111) by thermal reduction. The upper Sm_2O_3 layer spreads onto the Pt areas, as a result, so that finally about 90% Pt(111) surface is covered by a single trilayer of SmO_x , consisting of Sm_2O_3 and SmO patches. During the repeated MeOH TPD runs, the exposed Pt area continuously increases from ~10% to ~20% suggesting a dewetting of the substrate by the film. Monitoring the changes of Pt-related CO and H_2 peak intensities over the repeated TPD experiments confirms an increase of the exposed Pt area. Both Pt-related H_2 and CO peaks are barely seen in the first TPD, indicating that the Pt surface is almost entirely covered by SmO_x , but continuously increase during the repeated TPD runs. This result supports the interpretation that MeOH is capable of slightly reoxidizing the reduced 0.9 ML SmO_x film. Furthermore, the reoxidation by molecular oxygen at elevated temperatures leads to further dewetting and finally exposes 50% of the Pt(111) surface. For repeated MeOH TPD runs after reoxidation, the change of the exposed Pt surface area shows the same trend as for the as-prepared $\text{Sm}_2\text{O}_3/\text{Pt}(111)$ film, indicating that the sample condition is restored by the reoxidation process. It should be noted that the as-prepared and the reoxidized Sm_2O_3 films as well as the reduced films reach a similar condition with ~20% exposed Pt surface after repeated MeOH TPD experiments. The implication is that there is a single equilibrium condition of the SmO_x film structure upon continuous exposure to MeOH, independent of the initial film condition.

A comparison of the overall activity observed for the MeOH reaction on clean Pt(111), the continuous 2.8 ML SmO_x thin films, and the discontinuous 0.9 ML SmO_x film is provided in Table 1. From the calibration of CO, CO_2 , and H_2 yields, we estimated how many MLE of MeOH reacted on these surfaces. The overall activity follows the trend $\text{SmO}_x/\text{Pt}(111) > \text{SmO}_x \gg \text{Pt}(111)$ and suggests that a cooperative-effect between SmO_x and Pt on the 0.9 ML $\text{SmO}_x/\text{Pt}(111)$ samples must play an essential role for promoting the decomposition of MeOH. A likely explanation of this observation is a spillover of CO and H from SmO_x islands to exposed Pt surface occurring at low temperature (~250 K). As a result, adsorption sites (on-top sites) on SmO_x can be vacated. As the tail of the MeOH monolayer-desorption feature in TPD up to 250 K indicates, there is still molecular MeOH available on the surface which can fill the vacant methoxy adsorption sites on the SmO_x surface. Therefore, in total, more methoxy can react on the 0.9 ML $\text{SmO}_x/\text{Pt}(111)$ samples than on the continuous 2.8 ML SmO_x thin films. For a continuously driven reactor these SmO_x adsorption sites (on-top sites) in close proximity to Pt(111) areas should be relevant as they sustain cycles of methoxy decomposition—spillover of the products—readsorption of methoxy at relatively low temperature.

Table 1. Summary of the overall reactivity for the MeOH reaction on Pt(111), the 0.9 ML $\text{SmO}_x/\text{Pt}(111)$, and the 2.8 ML SmO_x samples. Yields of methanol reaction and ratios of $[\text{H}_2]/\{[\text{CO}] + [\text{CO}_2]\}$ estimated from TPD spectra on each samples. Yields of methanol reaction are defined by $[\text{CH}_3\text{OH}] = [\text{CO}] + [\text{CO}_2]$ except on the 0.9 ML reduced film (marked *), 0.35 MLE is estimated by $[\text{CH}_3\text{OH}] = 2 [\text{H}_2]$ because a fraction of carbon and oxygen remains on/in the reduced film.

TPD Spectra	Pt(111)	0.9 ML Samaria Thin Films			2.8 ML Samaria Thin Films		
	–	as prep. Sm_2O_3	red. SmO_x	reox. Sm_2O_3	as prep. Sm_2O_3	red. SmO_x	reox. Sm_2O_3
Yield of MeOH reaction (MLE)							
1st TPD	0.04	0.24	0.26	0.22	0.27	0.12	0.14
Ave. w/o 1st TPD	–	0.31	0.35 *	0.30	0.21	0.17	0.14
Ratio of $[\text{H}_2]/\{[\text{CO}]+[\text{CO}_2]\}$							
1st TPD	1.80	0.89	2.00	0.40	–	0.57	0.22
Ave. w/o 1st TPD	–	1.87	2.38	1.80	1.61	1.59	1.35

4. Conclusions

We investigated the adsorption and reaction of MeOH on both continuous and discontinuous SmO_x thin films on Pt(111) by TPD and IRRAS. Combining the available results, we conclude that MeOH is dehydrogenated forming mainly CO and H_2 as desorbing products. On as-prepared continuous and discontinuous $\text{Sm}_2\text{O}_3/\text{Pt}(111)$ samples, CO_2 is also produced in small quantities via CO oxidation by oxygen from the Sm_2O_3 surface. According to the yield estimation of products, we observe the highest reactivity for the discontinuous SmO_x film. The product yields obtained from the discontinuous film are, on average, a factor of 1.6 higher than those obtained from the continuous film. This observation can be explained by a spillover of products from SmO_x islands to exposed Pt areas, a mechanism which is not available on continuous films. All identified MeOH reaction mechanisms are summarized in Figure 10, while all detected IRRAS vibrational frequencies and their assignments are summarized in Table 2.

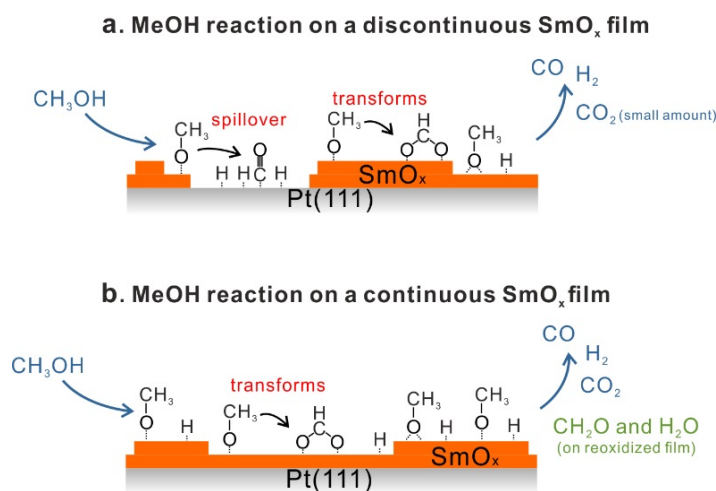


Figure 10. Summary of the MeOH reaction on (a) a discontinuous SmO_x thin film, and (b) a continuous SmO_x thin film.

Table 2. Vibrational frequencies and assignments of methanol, methoxy and formate species collected from the 0.7 ML and 2.3 ML SmO_x/Pt(111) samples. The corresponding IRRAS spectra of the 2.3 (± 0.2) ML thick continuous SmO_x film are shown in Figure S4.

Assignments	Vibrational Frequencies						
	Methanol	Methoxy and Formate Species					
	(cm ⁻¹)	0.7 ML Sm ₂ O ₃ (cm ⁻¹)	0.7 ML red. SmO _x (cm ⁻¹)	0.7 ML reox. Sm ₂ O ₃ (cm ⁻¹)	2.3 ML Sm ₂ O ₃ (cm ⁻¹)	2.3 ML red. SmO _x (cm ⁻¹)	2.3 ML reox. Sm ₂ O ₃ (cm ⁻¹)
ν(C-O)	1046	1080–1077	1089–1077	1084–1078	1083–1074	1065–1057	1080–1072
		1065	1061	1055–1052	1062	1015	1066
		1042	1037		1049		1050
ρ(CH ₃)	1130	1140	1140				
ν _s (OCO), δ(CH)		1378	1378	1377	1377		1378
ν(C≡O) ^a		~2080	~2080	~2088	~2089		
ν _s (CH ₃)	2831	2790	2790	2780	2780	2800	2780
2δ(CH ₃), ν(CH)	*	2856	2851	2850	2840	2854	2837
ν _{as} (CH ₃)	2957	2926	2926	2941	2925	2938	2920
ν(OH)	3280						

Notes: ^a The band corresponds to carbon monoxide on the exposed Pt(111) surface. * The overtone band in case of methanol sits underneath the CH₃ symmetric and asymmetric stretch bands.

Effects of the SmO_x structure on the MeOH reaction, and *vice versa*, were revealed by studying as-prepared, reduced, and re-oxidized films. The highest reactivity was observed for a discontinuous SmO_x film after thermal reduction, containing an unknown amount of SmO domains. Moreover, the MeOH decomposition leaves some amount of oxygen on the reduced film, indicating surface reoxidation by MeOH. The SmO domains most likely promote reduction reactions while being oxidized. However, one may conceive that the phase boundaries should also play a dominant role for the overall reactivity of the film. Therefore, while we find evidence, e.g., for new adsorption sites for methoxy on the reduced film, it cannot unambiguously assigned to the SmO(100) phase. CO₂ is detected from both continuous and discontinuous films, but the highest CO₂ yield was observed for the as-prepared continuous film suggesting that there is an oxygen species available for oxidation reactions on SmO_x films, which is not necessarily expected from a rare earth sesquioxide. Apart from the effect of the film's surface structures on the MeOH reactivity, the decomposition of MeOH itself also modifies the SmO_x structure as revealed by repeated TPD experiments. They probably involve oxygen vacancy formation at the surface.

Our results indicate that whether as-prepared or reoxidized or reduced discontinuous films are used as a starting point, MeOH decomposition on these films drives the SmO_x toward a structural equilibrium condition. The SmO_x-related desorption signals of products obtained for both oxidized and reduced films over repeated TPD runs reach a similar temperature of maximum desorption (~550 K) while the fraction of exposed Pt area adjusts to ~20% of the entire surface area. Finally, the repeated TPD experiments reveal that hydrogen is stored either in the film or as OH groups on the SmO_x surface. Further investigations are in progress to elucidate the origin of the capability of SmO_x films for hydrogen storage.

Supplementary Materials

Supplementary materials can be accessed at: <http://www.mdpi.com/1996-1944/8/9/6228/s1>.

Acknowledgments

Funding by the Deutsche Forschungsgemeinschaft under contract No. Ba 1710/19-1 and by the National Science Foundation, Division of Chemistry, through grant number 1026712 is gratefully acknowledged.

Author Contributions

Jin-Hao Jhang performed all experiments and data analysis and prepared all Figures and Tables. Andreas Schaefer contributed to experiment design and data evaluation and interpretation. Volkmar Zielasek and Jason F. Weaver contributed to data interpretation. Jin-Hao Jhang, Volkmar Zielasek and Andreas Schaefer wrote the manuscript. Andreas Schaefer and Marcus Bäumer supervised the work. All authors reviewed the manuscript.

Conflicts of Interest

The authors declare no conflict of interest.

References

1. Goonan, T.G. *Rare Earth Elements—End Use and Recyclability*; U.S. Geological Survey: Reston, VA, USA, 2011.
2. Trovarelli, A.; Fornasiero, P. *Catalytic Science Series*; Imperial College Press: London, UK, 2013.
3. Schroeder, T.; Giussani, A.; Muessig, H.J.; Weidner, G.; Costina, I.; Wenger, C.; Lukosius, M.; Storck, P.; Zaumseil, P. Ge integration on Si via rare earth oxide buffers: From MBE to CVD (invited paper). *Microelectron. Eng.* **2009**, *86*, 1615–1620. [[CrossRef](#)]
4. Rosynek, M.P. Catalytic properties of rare earth oxides. *Catal. Rev.* **1977**, *16*, 111–154. [[CrossRef](#)]
5. Campbell, K.D.; Zhang, H.; Lunsford, J.H. Methane activation by the lanthanide oxides. *J. Phys. Chem.* **1988**, *92*, 750–753. [[CrossRef](#)]
6. Dedov, A.G.; Loktev, A.S.; Moiseev, II; Aboukais, A.; Lamonier, J.F.; Filimonov, I.N. Oxidative coupling of methane catalyzed unexpected synergistic effect of the by rare earth oxides oxide mixtures. *Appl. Catal. A-Gen.* **2003**, *245*, 209–220. [[CrossRef](#)]
7. Elkins, T.W.; Neumann, B.; Bäumer, M.; Hagelin-Weaver, H.E. Effects of Li doping on MgO-supported Sm₂O₃ and TbO_x catalysts in the oxidative coupling of methane. *ACS Catal.* **2014**, *4*, 1972–1990. [[CrossRef](#)]
8. Rodriguez, J.A.; Ma, S.; Liu, P.; Hrbek, J.; Evans, J.; Pérez, M. Activity of CeO_x and TiO_x nanoparticles grown on Au(111) in the water-gas shift reaction. *Science* **2007**, *318*, 1757–1760. [[CrossRef](#)] [[PubMed](#)]
9. Senanayake, S.D.; Stacchiola, D.; Rodriguez, J.A. Unique properties of ceria nanoparticles supported on metals: Novel inverse ceria/copper catalysts for CO oxidation and the water-gas shift reaction. *Acc. Chem. Res.* **2013**, *46*, 1702–1711. [[CrossRef](#)] [[PubMed](#)]
10. Adachi, G.; Imanaka, N. The binary rare earth oxides. *Chem. Rev.* **1998**, *98*, 1479–1514. [[CrossRef](#)]

11. Rodriguez, J.A.; Graciani, J.; Evans, J.; Park, J.B.; Yang, F.; Stacchiola, D.; Senanayake, S.D.; Ma, S.; Pérez, M.; Liu, P.; *et al.* Water-gas shift reaction on a highly active inverse CeO_x/Cu(111) catalyst: Unique role of ceria nanoparticles. *Angew. Chem. Int. Ed.* **2009**, *48*, 8047–8050. [[CrossRef](#)] [[PubMed](#)]
12. Hornés, A.; Hungría, A.B.; Bera, P.; Cámara, A.L.; Fernández-García, M.; Martínez-Arias, A.; Barrio, L.; Estrella, M.; Zhou, G.; Fonseca, J.J.; *et al.* Inverse CeO₂/CuO catalyst as an alternative to classical direct configurations for preferential oxidation of CO in hydrogen-rich stream. *J. Am. Chem. Soc.* **2010**, *132*, 34–35. [[CrossRef](#)] [[PubMed](#)]
13. Jhang, J.-H.; Schaefer, A.; Cartas, W.; Epuri, S.; Bäumer, M.; Weaver, J.F. Growth and partial reduction of Sm₂O₃(111) thin films on Pt(111): Evidence for the formation of SmO(100). *J. Phys. Chem. C* **2013**, *117*, 21396–21406. [[CrossRef](#)]
14. Cartas, W.; Rai, R.; Sathe, A.; Schaefer, A.; Weaver, J.F. Oxidation of a Tb₂O₃(111) thin film on Pt(111) by gas-phase oxygen atoms. *J. Phys. Chem. C* **2014**, *118*, 20916–20926. [[CrossRef](#)]
15. Höcker, J.; Cartas, W.; Schaefer, A.; Bäumer, M.; Weaver, J.F.; Falta, J.; Flege, J.I. Growth, structure, and stability of the high-index TbO_x(112) surface on Cu(111). *J. Phys. Chem. C* **2015**, *119*, 14175–14184. [[CrossRef](#)]
16. Netzer, F.P.; Allegretti, F.; Surnev, S. Low-dimensional oxide nanostructures on metals: Hybrid systems with novel properties. *J. Vac. Sci. Technol. B* **2010**, *28*, 1–16. [[CrossRef](#)]
17. Matolin, V.; Libra, J.; Skoda, M.; Tsud, N.; Prince, K.C.; Skala, T. Methanol adsorption on a CeO₂(111)/Cu(111) thin film model catalyst. *Surf. Sci.* **2009**, *603*, 1087–1092. [[CrossRef](#)]
18. Albrecht, P.M.; Mullins, D.R. Adsorption and reaction of methanol over CeO_x(100) thin films. *Langmuir* **2013**, *29*, 4559–4567. [[CrossRef](#)] [[PubMed](#)]
19. Mullins, D.R.; Robbins, M.D.; Zhou, J. Adsorption and reaction of methanol on thin-film cerium oxide. *Surf. Sci.* **2006**, *600*, 1547–1558. [[CrossRef](#)]
20. Akhter, S.; White, J.M. A static SIMS/TPD study of the kinetics of methoxy formation and decomposition on O/Pt(111). *Surf. Sci.* **1986**, *167*, 101–126. [[CrossRef](#)]
21. Gibson, K.D.; Dubois, L.H. Step effects in the thermal decomposition of methanol on Pt(111). *Surf. Sci.* **1990**, *233*, 59–64. [[CrossRef](#)]
22. Sexton, B.A. Methanol decomposition on platinum (111). *Surf. Sci.* **1981**, *102*, 271–281. [[CrossRef](#)]
23. Diekhöner, L.; Butler, D.A.; Baurichter, A.; Luntz, A.C. Parallel pathways in methanol decomposition on Pt(111). *Surf. Sci.* **1998**, *409*, 384–391. [[CrossRef](#)]
24. Greeley, J.; Mavrikakis, M. A first-principles study of methanol decomposition on Pt(111). *J. Am. Chem. Soc.* **2002**, *124*, 7193–7201. [[CrossRef](#)] [[PubMed](#)]
25. Greeley, J.; Mavrikakis, M. Competitive paths for methanol decomposition on Pt(111). *J. Am. Chem. Soc.* **2004**, *126*, 3910–3919. [[CrossRef](#)] [[PubMed](#)]
26. Feilberg, K.L.; Sellevag, S.R.; Nielsen, C.J.; Griffith, D.W.T.; Johnson, M.S. CO + OH → CO₂ + H: The relative reaction rate of five CO isotopologues. *Phys. Chem. Chem. Phys.* **2002**, *4*, 4687–4693. [[CrossRef](#)]

27. Shido, T.; Yamaguchi, A.; Asakura, K.; Iwasawa, Y. Surface catalytic reactions assisted by gas phase molecules: Activation of reaction intermediates. *J. Mol. Catal. A Chem.* **2000**, *163*, 67–77. [[CrossRef](#)]
28. Putna, E.S.; Shereck, B.; Gorte, R.J. Adsorption and reactivity of lanthana with CO. *Appl. Catal. B* **1998**, *17*, 101–106. [[CrossRef](#)]
29. Putna, E.S.; Vohs, J.M.; Gorte, R.J. Evidence for weakly bound oxygen on ceria films. *J. Phys. Chem.* **1996**, *100*, 17862–17865. [[CrossRef](#)]
30. Badlani, M.; Wachs, I. Methanol: A “smart” chemical probe molecule. *Catal. Lett.* **2001**, *75*, 137–149. [[CrossRef](#)]
31. Tatibouët, J.M. Methanol oxidation as a catalytic surface probe. *Appl. Catal. A* **1997**, *148*, 213–252. [[CrossRef](#)]
32. Luches, P.; Pagliuca, F.; Valeri, S. Morphology, stoichiometry, and interface structure of CeO₂ ultrathin films on Pt(111). *J. Phys. Chem. C* **2011**, *115*, 10718–10726. [[CrossRef](#)]
33. Eck, S.; Castellarin-Cudia, C.; Surnev, S.; Ramsey, M.G.; Netzer, F.P. Growth and thermal properties of ultrathin cerium oxide layers on Rh(111). *Surf. Sci.* **2002**, *520*, 173–185. [[CrossRef](#)]
34. Mullins, D.R.; Overbury, S.H.; Huntley, D.R. Electron spectroscopy of single crystal and polycrystalline cerium oxide surfaces. *Surf. Sci.* **1998**, *409*, 307–319. [[CrossRef](#)]
35. Fu, Q.; Wagner, T. Interaction of nanostructured metal overlayers with oxide surfaces. *Surf. Sci. Rep.* **2007**, *62*, 431–498. [[CrossRef](#)]
36. Zhang, X.; Klabunde, K.J. Superoxide (O₂⁻) on the surface of heat-treated ceria. Intermediates in the reversible oxygen to oxide transformation. *Inorg. Chem.* **1992**, *31*, 1706–1709. [[CrossRef](#)]
37. Binet, C.; Daturi, M.; Lavalley, J.-C. IR study of polycrystalline ceria properties in oxidised and reduced states. *Catal. Today* **1999**, *50*, 207–225. [[CrossRef](#)]
38. Guzman, J.; Carrettin, S.; Corma, A. Spectroscopic evidence for the supply of reactive oxygen during CO oxidation catalyzed by gold supported on nanocrystalline CeO₂. *J. Am. Chem. Soc.* **2005**, *127*, 3286–3287. [[CrossRef](#)] [[PubMed](#)]
39. Siokou, A.; Nix, R.M. Interaction of methanol with well-defined ceria surfaces: Reflection/absorption infrared spectroscopy, X-ray photoelectron spectroscopy, and temperature-programmed desorption study. *J. Phys. Chem. B* **1999**, *103*, 6984–6997. [[CrossRef](#)]
40. Badri, A.; Binet, C.; Lavalley, J.-C. Use of methanol as an IR molecular probe to study the surface of polycrystalline ceria. *J. Chem. Soc. Faraday Trans.* **1997**, *93*, 1159–1168. [[CrossRef](#)]
41. Barros, R.B.; Garcia, A.R.; Ilharco, L.M. The chemistry of formic acid on oxygen modified Ru(0001) surfaces. *Surf. Sci.* **2005**, *591*, 142–152. [[CrossRef](#)]
42. Mudiyansele, K.; Baber, A.E.; Liu, Z.; Senanayake, S.D.; Stacchiola, D.J. Isolation and characterization of formates on CeO_x-Cu_yO/Cu(111). *Catal. Today* **2015**, *240*, 190–200. [[CrossRef](#)]
43. Ritter, M.; Ranke, W.; Weiss, W. Growth and structure of ultrathin FeO films on Pt(111) studied by STM and LEED. *Phys. Rev. B* **1998**, *57*, 7240–7251. [[CrossRef](#)]
44. Namai, Y.; Fukui, K.-I.; Iwasawa, Y. Atom-resolved noncontact atomic force microscopic and scanning tunneling microscopic observations of the structure and dynamic behavior of CeO₂(111) surfaces. *Catal. Today* **2003**, *85*, 79–91. [[CrossRef](#)]

45. Namai, Y.; Fukui, K.-I.; Iwasawa, Y. The dynamic behaviour of CH₃OH and NO₂ adsorbed on CeO₂(111) studied by noncontact atomic force microscopy. *Nanotechnology* **2004**, *15*, S49–S54. [[CrossRef](#)]
46. Esch, F.; Fabris, S.; Zhou, L.; Montini, T.; Africh, C.; Fornasiero, P.; Comelli, G.; Rosei, R. Electron localization determines defect formation on ceria substrates. *Science* **2005**, *309*, 752–755. [[CrossRef](#)] [[PubMed](#)]
47. Lin, Y.; Wu, Z.; Wen, J.; Ding, K.; Yang, X.; Poepelmeier, K.R.; Marks, L.D. Adhesion and atomic structures of gold on ceria nanostructures: The role of surface structure and oxidation state of ceria supports. *Nano Lett.* **2015**, *15*, 5375–5381. [[CrossRef](#)] [[PubMed](#)]

© 2015 by the authors; licensee MDPI, Basel, Switzerland. This article is an open access article distributed under the terms and conditions of the Creative Commons Attribution license (<http://creativecommons.org/licenses/by/4.0/>).

Supplementary Information

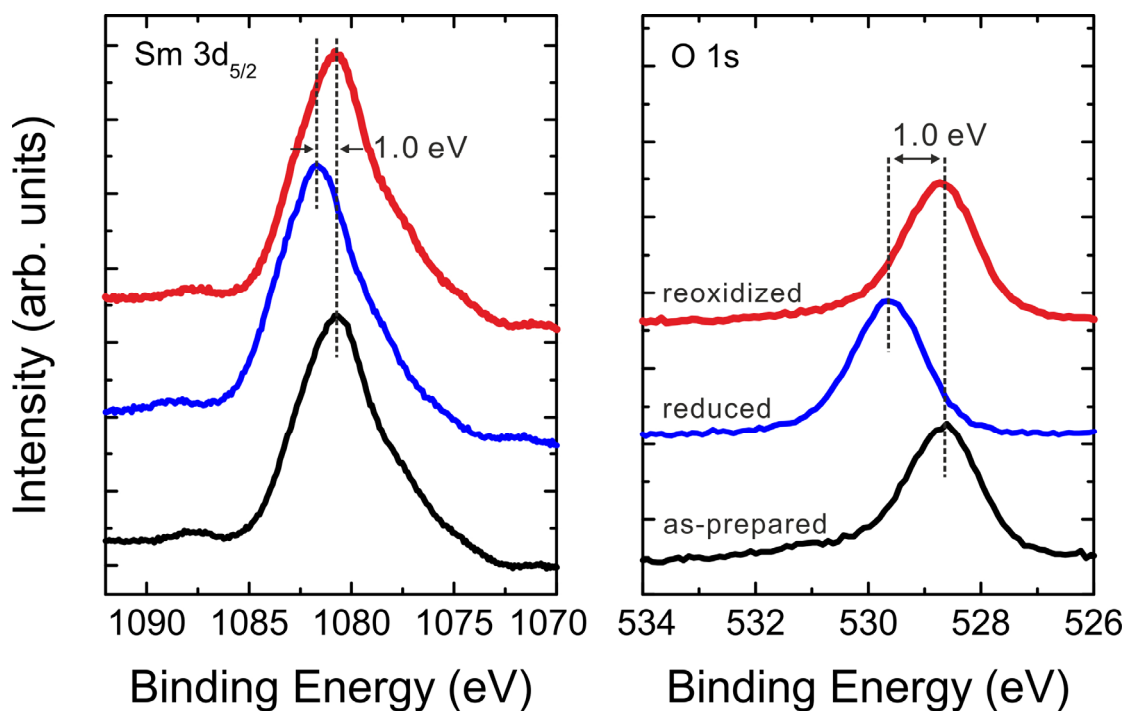


Figure S1. XPS spectra of Sm 3d_{5/2} and O 1s regions collected from the 2.8 ML as-prepared, reduced, and reoxidized SmO_x thin films.

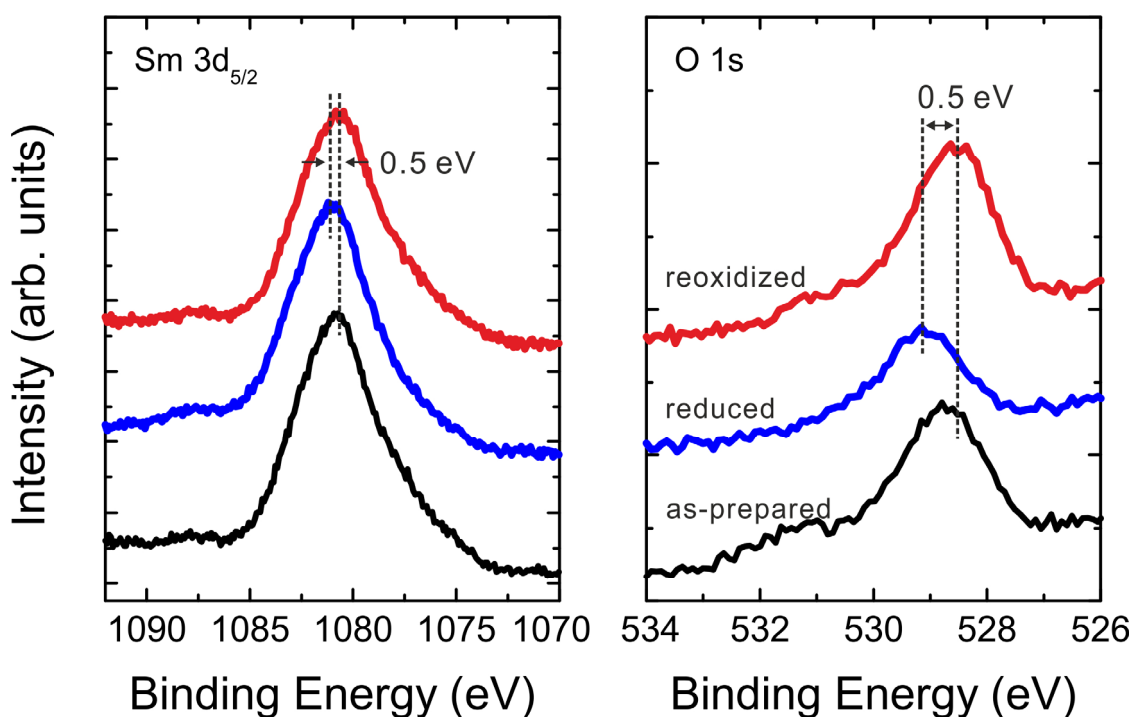


Figure S2. XPS spectra of Sm 3d_{5/2} and O 1s regions collected from the 0.9 ML as-prepared, reduced, and reoxidized SmO_x thin films.

Schematic representation of LEED patterns

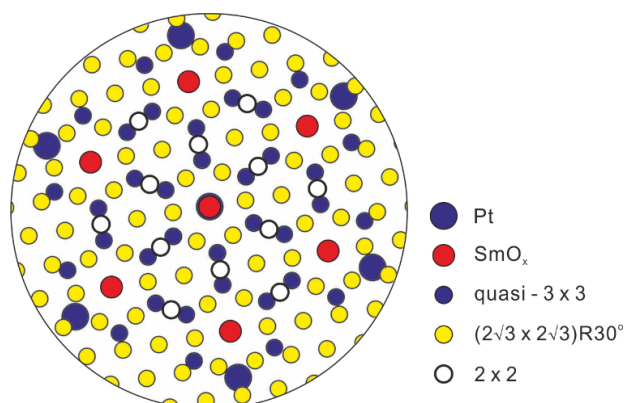
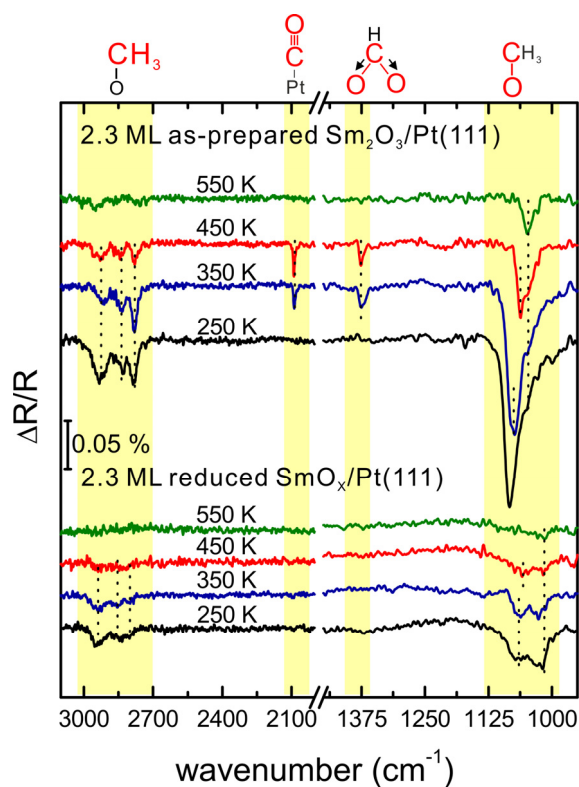


Figure S3. Summary of LEED patterns observed.

Table S1. Summary of LEED patterns observed for the differently prepared SmO_x deposits.

MeOH TPD Treatment	LEED Patterns of 0.9 ML SmO_x on Pt(111)		
	as-prepared Sm_2O_3	reduced SmO_x	reoxidized Sm_2O_3
w/o	quasi- 3×3	satellites	quasi- $3 \times 3 + 2$ add. spots
with	slightly rotated	rotated	quasi- $3 \times 3 + 2$ add. spots + $(2\sqrt{3} \times 2\sqrt{3})R30^\circ$
MeOH TPD Treatment	LEED Patterns of 2.8 ML SmO_x on Pt(111)		
	as-prepared Sm_2O_3	reduced SmO_x	reoxidized Sm_2O_3
w/o	quasi- 3×3	quasi- $3 \times 3 + (2\sqrt{3} \times 2\sqrt{3})R30^\circ$	quasi- $3 \times 3 + 2 \times 2$
with	$\text{SmO}_x(1 \times 1)$	quasi- $3 \times 3 + (2\sqrt{3} \times 2\sqrt{3})R30^\circ$	quasi- $3 \times 3 + (2\sqrt{3} \times 2\sqrt{3})R30^\circ$

Figure S4. Temperature-dependent IRRAS spectra collected from the 2.3 ML as-prepared and reduced SmO_x thin films.